CZECH TECHNICAL UNIVERSITY IN PRAGUE
Faculty of Mechanical Engineering
Department of Fluid Dynamics and Thermodynamics

Synthetic and continuous jets impinging on a circular cylinder:

Flow field and heat transfer experimental study

Doctoral thesis

Ing. Zuzana BROUČKOVÁ

Study field: Thermomechanics and fluid mechanics

Supervisor: Prof. Ing. Pavel Šafařík, CSc.
Supervisor-specialist: Doc. Ing. Zdeněk Trávníček, CSc.

2018 Prague

Declaration of authorship

I hereby confirm that the submitted work is entirely my own and was written only with help of referenced literature.

Abstract

Synthetic and continuous jets impinging onto an heated circular cylinder were investigated.

The study was performed experimentally. For this reason, a piezoelectrically driven actuator with water as the working fluid was designed. The basic parameters of the experiments were: the slot nozzle width was 0.36 mm, the aspect ratio of the slot was 111, the cylinder diameter was 1.2 mm, and the cylinder-to-nozzle spacing related to the slot width was 5–21.

The experimental investigation of the flow field and heat transfer was performed by means of various independent methods. To investigate the flow field, three optical methods were used: qualitative laser-induced fluorescence (LIF) visualization, laser Doppler vibrometry (LDV) measurements, and particle image velocimetry (PIV) measurements. To investigate the heat transfer, the overall convective heat transfer from the circular cylinder was evaluated, simultaneously with the optical experiments.

The heat transfer experiments were validated in a natural convection regime and reasonable agreement with representative references was concluded. An enhancement of the average Nusselt numbers by 4.2–6.2 times by means of the synthetic jets was quantified by comparison with the natural convection regime. A correlation for the average Nusselt number was proposed for both the continuous and synthetic jets.

Abstrakt

Syntetizovaný a kontinuální proud, které dopadaly na zahřívaný kruhový válec, byly zkoumány.

Práce byla experimentální. Pro tento účel byl navržen piezoelektrický generátor. Pracovním médiem byla voda. Základní parametry experimentu byly následující: šířka trysky byla 0,36 mm, poměr délky a šířky trysky byl 111, průměr válce byl 1,2 mm a vzdálenost mezi tryskou a válcem byla 5-21.

Experimentální vyšetřování proudového pole a přestupu tepla bylo provedeno za použití rozličných nezávislých metod. Při vyšetřování proudového pole byly použity tři optické metody: kvalitativní vizualizace pomocí metody laserem indukované fluorescence (laser induced fluorescence, LIF), laserová dopplerovská vibrometrie (laser Doppler vibrometry, LDV) a integrální laserová anemometrie (particle image velocimetry, PIV). Souběžně s optickými experimenty byl vyhodnocován celkový přestup tepla z kruhového válce.

Experimenty s přestupem tepla byly validovány režimem přirozené konvekce, kdy byla dosažena dobrá shoda s relevantními daty z dostupné literatury. Bylo zjištěno zvýšení Nusseltova čísla 4,2 až 6,2-krát při použití syntetizovaného proudu oproti režimu přirozené konvekce. Byla navržena kriteriální rovnice pro průměrné Nusseltovo číslo platná pro syntetizovaný i kontinuální proud.

Acknowledgements

My thanks go firstly to my supervisor Prof. Ing. Pavel Šafařík, CSc. for his advice during all my studies and during writing my thesis.
I wish to give great thanks to my consultant, Zdeněk Trávníček, for his input, positive attitude and enormous help during my entire PhD study.

The experiments were performed in the laboratory of the Institute of Thermomechanics of the Czech Academy of Sciences.
Some of the PIV measurements were also performed in the laboratory of the Institute of Applied Mechanics of the National Taiwan University. I would like to thank Prof. An-Bang Wang and Dr. Shu-Shen Hsu for the help with the PIV system.

Financial support for the research was provided by GA CR (16-16596S, *Optimization of pulsatile jet actuation in fluid mechanics*), GA CR (14-08888S, *Control of flow fields by means of fluid oscillation*) and AS CR-MOST Taiwan (reg. n. 1, 2014-2015, *Nonisothermal synthetic jets and hybrid synthetic jets*).

Contents

Declaration of authorship ..... **iii**

Abstract (EN) ..... **iv**

Abstrakt (CZ) ..... **v**

Acknowledgements ..... **vi**

Contents ..... **vii**

List of Figures ..... **ix**

List of Tables ..... **xii**

List of symbols and abbreviations ..... **xiii**

1. Introduction **1**

1.1 Motivation 1

1.2 State of the art 3

1.2.1 Continuous jets 3

1.2.1.1 Turbulent plane jet 4

1.2.1.2 Rectangular turbulent jets 6

1.2.1.3 Microjets and very low Reynolds number jets 9

1.2.2 Synthetic jets 11

1.2.3 Convective heat transfer 14

1.2.3.1 Natural convection - correlations for the Nusselt number 17

1.2.3.2 Forced convection 19

1.2.3.3 CJ impingement heat transfer 21

1.2.3.4 SJ impingement heat transfer 26

1.3 Aims of the dissertation 27

2. Experimental setup **29**

3. Experimental methods and uncertainties **33**

3.1 Laser induced fluorescence (LIF) 33

3.2 Particle image velocimetry (PIV) 36

3.2.1 Uncertainties of the PIV method 39

3.3 Laser Doppler vibrometry (LDV) 44

3.4 Gravimetric method 46

3.5 Temperature measurement 47
3.5.1 Uncertainties of the Nusselt number evaluation 47
4. Relevant parameters 49
4.1 Continuous jet 49
4.2 Synthetic jet 49
4.3 Heat transfer 51
5. Results and analysis 52
5.1 Continuous jet 52
5.1.1 Evaluation of the time-mean exit velocity 52
5.1.2 Continuous jet - flow visualization 52
5.1.3 Continuous jet - PIV results 55
5.2 Synthetic jet 67
5.2.1 Resonance 67
5.2.2 Synthetic jet - LDV results 68
5.2.3 Synthetic jet - flow visualization 73
5.2.4 Synthetic jet - PIV results 77
5.3 The jet impinging onto the cylinder 100
5.4 Convective heat transfer 106
5.4.1 Natural convection 106
5.4.2 Forced convection 107
6. Conclusions 112
6.1 Results and contribution of the thesis 112
6.2 Future work 114
List of references 115
Publications of author 123
Appendix I - Velocity and vorticity maps of the CJ 127
Appendix II - Velocity and vorticity maps of the SJ 128

List of figures

Fig. 1.1 Scheme of the plane turbulent jet 4
Fig. 1.2 The variation of the exponent n of the velocity decay $U_c \sim x^{-n}$ in the characteristic region with the inverse value of the aspect ratio, $e = 1/AR$ 7
Fig. 1.3 The mean vorticity contours of the rectangular synthetic jet with $f = 300$ Hz 13
Fig. 1.4 The representative correlations for natural convection regime from collections by Morgan [70], the correlation by Morgan [70] and the correlation by Churchill and Chu [81] 18
Fig. 1.5 Forced convection from circular cylinder in air cross-flow at moderate temperature loading of $T_w/T_\infty = 1.50$ 20
Fig. 1.6 Heat transfer coefficient h of a cylinder of 19.5 mm diameter and the centerline velocity decay, $Re \sim 35{,}000\text{-}50{,}000$ 22
Fig. 1.7 Nusselt number correlations and experimental points by Jeng et al. [106] for the cylinder under the CJ impingement and the correlation by Morgan [70] for the cylinder in the cross-flow 25

Fig. 2.1 Schematic view of the experimental device 29
Fig. 2.2 Detail photograph of the nozzle and the comparison of with human hair 30
Fig. 2.3 The overall scheme of the experiment 31

Fig. 3.1 Absorption and emission spectra of Rhodamine B for 20, 30, 40, 50, 60 and 70ºC .. 34
Fig. 3.2 Schematic view on the exit slot (from the top) with planes where the LIF visualization and PIV measurement were performed 35
Fig. 3.3 Scheme of the PIV measurement technique 36
Fig. 3.4 Experimental uncertainty estimated for the present PIV measurement 42
Fig. 3.5 Arrangement of 9 points for LDV velocity measurements of the oscillating diaphragm 45

Fig. 5.1 Visualization of the CJ 53
Fig. 5.2 Visualization of the CJ in y-z planes 54
Fig. 5.3 Velocity vector field of the CJ along the slot (x-z plane) 56

Fig. 5.4 Velocity vector field of the CJ across the slot (*x*-*y* plane) at *z*/*B* = -41.7 and 0 58
Fig. 5.5 Contours of the streamwise velocity component of the CJ 59
Fig. 5.6 3D contours of the streamwise velocity component of the CJ 60
Fig. 5.7 Streamwise velocity profiles of the CJ (at *z*/*B* = 0) 61
Fig. 5.8 Normalized streamwise velocity profiles of the CJ (at *z*/*B* = 0) 62
Fig. 5.9 Streamwise velocity profiles of the CJ (at *z*/*B* = 0) normalized using the half-width 63
Fig. 5.10 Evolution of (a) half-width and (b) volume flux of the CJ 66
Fig. 5.11 Evolution of the streamwise component of the CJ centerline velocity 67
Fig. 5.12 Velocity of the oscillating diaphragm center 69
Fig. 5.13 Velocity of the oscillating diaphragm 69
Fig. 5.14 Profiles of the diaphragm displacement 71
Fig. 5.15 Frequency characteristics of the SJ actuator obtained by LDV measurement 72
Fig. 5.16 Visualization of the SJ across the slot (*x*-*y* plane) 74
Fig. 5.17 Visualization of the SJ along the slot (*x*-*z* plane) 75
Fig. 5.18 Visualization of the SJ in *y*-*z* planes at arbitrary phase 76
Fig. 5.19 Velocity vector field of the SJ along the slot (*x*-*z* plane) colored by the velocity magnitude 79
Fig. 5.20 Velocity vector field of the SJ along the slot (*x*-*z* plane) colored by vorticity 80
Fig. 5.21 Velocity vector field of the SJ along the slot (*x*-*z* plane) colored by velocity magnitude (detail view) 81
Fig. 5.22 Velocity vector field of the SJ across the slot (*x*-*y* plane) at *z*/*B* = -41.7 82
Fig. 5.23 Velocity vector field of the SJ across the slot (*x*-*y* plane) at *z*/*B* = 0 83
Fig. 5.24 Velocity vector field of the SJ across the slot (*x*-*y* plane) at *z*/*B* = -41.7 and φ = 90° and 270° 86
Fig. 5.25 Velocity vector field of the SJ across the slot (*x*-*y* plane) at *z*/*B* = 0 and φ = 90° and 270° 87
Fig. 5.26 Contours of the streamwise velocity component of the SJ 89
Fig. 5.27 3D contours of the streamwise velocity component of the SJ 90
Fig. 5.28 3D contours of the time-mean streamwise velocity component 91
Fig. 5.29 Velocity profiles of the SJ 93
Fig. 5.30 Dimensionless stream-wise velocity component of the SJ 94
Fig. 5.31 Dimensionless stream-wise velocity component of the SJ 95
Fig. 5.32 Evolution of the half-width of the SJ 97

Fig. 5.33 Evolution of the half-width - the comparison of the SJ and CJ 98
Fig. 5.34 Evolution of the volume flow rate of the SJ 99
Fig. 5.35 Evolution of the volume flow rate - the comparison of the SJ and CJ 99
Fig. 5.36 Evolution of the time-mean streamwise centerline velocity of the SJ and the comparison with CJ 100
Fig. 5.37 LIF visualization of the CJs, unheated cases at $T_w = T_\infty$ and $H/B = 20.8$ 102
Fig. 5.38 LIF visualization of the SJs, $Re_{SJ} = 67$, $H/B = 20.8$ 102
Fig. 5.39 Velocity vector field colored by velocity magnitude and the corresponding streamlines of the CJ impinging onto the cylinder 104
Fig. 5.40 Instantaneous velocity vector field colored by the vorticity and the corresponding streamlines of the CJ impinging onto a cylinder at $Re_{CJ} = 161$ ($Re_{CJ,D} = 542$) 105
Fig. 5.41 Validation experiment - the natural convection 107
Fig. 5.42 Frequency characteristic of the SJ 107
Fig. 5.43 Comparison of the natural and forced convection (SJ, $H/B = 10$) 108
Fig. 5.44 Effect of the nozzle-to-cylinder spacing on *Nu* 109
Fig. 5.45 Overall heat transfer (a) Nu-Re_D and (b) Nu-Re_{DC} 111

List of tables

Table 1 Nusselt number correlations according to Morgan [70] 18
Table 2 Nusselt number uncertainty analysis for the natural convection experiments 48
Table 3 Nusselt number uncertainty analysis - typical forced convection experiment (SJ) ... 48
Table 4 Parameters of the CJ experiments 52
Table 5 Parameters of the experiments - CJ and SJ impinging onto the cylinder 101

List of symbols and abbreviations

Roman symbols

A	m^2	area
B	m	width of the nozzle slot (see Fig. 3.1)
c		shape constant of the diaphragm
C		ratio of the exit velocity in the z location to the mean exit velocity U_m (see Eq. 44)
D	m	diameter of the cylinder
f	Hz	frequency
g	m^2/s	acceleration of gravity
h	W/m^2K	heat transfer coefficient
H	m	nozzle-to-cylinder distance
I_c	A	electrical current through the cylinder
I_{SJ}	A	electrical current of the synthetic jet actuator input
k	W/mK	thermal conductivity
K		coverage factor
L	m	length of the nozzle exit channel
L_b	m	breakdown length of the jet (see Eq. 3 and 4)
L_H	m	length of the test section of the cylinder
L_s	m	length of the nozzle slot (see Fig. 3.1)
L_0	m	stroke length of the synthetic jet (see Eq. 33)
P_{SJ}	W	power input of the synthetic jet actuator
Q	m3/s	volume flux
Q_z	m2/s	volume flux related to the z coordinate
t	s	time
T	s	duration of the period
T_f	ºC	film temperature
T_w	ºC	surface (wall) temperature
T_∞	ºC	bulk temperature
u_0	m/s	synthetic jet instantaneous exit velocity (see Eq. 27)

U	m/s	time-mean streamwise velocity component
U_c	m/s	jet centerline axial velocity
U_e	m/s	jet exit axial velocity
U_m	m/s	continuous jet exit mean velocity
U_{max}	m/s	jet maximum velocity
U_0	m/s	synthetic jet time-mean exit velocity (see Eq. 34)
v	m/s	velocity of the vibrating diaphragm
V	m/s	time-mean cross-stream velocity component
V_c	V	electrical voltage between the cylinder contact points
V_{SJ}	V	voltage of the synthetic jet actuator input
W	m/s	time-mean spanwise velocity component
$U_{x\text{-}y}$	m/s	velocity magnitude in x-y plane (see Eq. 20)
$U_{x\text{-}z}$	m/s	velocity magnitude in x-z plane (see Eq. 21)
x	m	axial (stream-wise) coordinate
y	m	horizontal (cross-stream) coordinate
$y_{0.5}$	m	half-width of the jet
y^*	m	shifted horizontal coordinate
z	m	longitudinal (span-wise) coordinate

Greek symbols

α	m^2/s	thermal diffusivity
γ	º	half-angle of the jet
β	1/K	volumetric thermal expansion coefficient
λ	m	wavelength
φ	º	phase angle of the synthetic jet
θ	º	phase shift between I_{SJ} and V_{SJ}
ν	m^2/s	kinematic viscosity
σ		uncertainty (see Eq. 22 and 30)

Dimensionless numbers

Gr	Grashof number (see Eq. 5)
Nu	Nusselt number (see Eq. 8)
Pr	Prandtl number (see Eq. 7)

Re	Reynolds number
Re_{CJ}	continuous jet Reynolds number (see Eq. 31)
$Re_{CJ,\,D}$	continuous jet Reynolds number based on the cylinder diameter (see Eq. 32)
Re_D	Reynolds number based on the cylinder diameter
Re_{DC}	corrected Reynolds number (see Eq. 45)
Re_{SJ}	synthetic jet Reynolds number (see Eq. 35)
$Re_{SJ,\,D}$	synthetic jet Reynolds number based on the cylinder diamter (see Eq. 36)
St	Strouhal number (see Eq. 37)
Ri	Richardson number
S	Stokes number (see Eq. 38)

Abbreviations

AR	aspect ratio
dgt	digit
FS	full scale
rdg	reading
SJ	synthetic jet
CJ	continuous jet

1. Introduction

The fluid jet flow phenomenon has been attracting scientific researchers from ancient times. The aeolipile is considered the first fluid jet flow application, i.e., a steam-powered device, and Hero(n) of Alexandria is generally credited for creating it in the first AD century. In the 18th century, the same reactive jet flow principle was applied by Johann Andreas Segner to design one of the first usable water turbines. Relevant examples of this type of technology can be found in the Far East and old China, including blowpipes for metallurgical processes and rockets, which were used for entertainment and military purposes (fireworks, pyrotechnics and missiles). Leonardo da Vinci is often considered the first scientist and polymath of the modern period to conduct scientific research in general. Among his many interests, he studied the profile of liquid jets, the impact of a water jet on the surface of water or a wake flow behind a cylinder [1]. Ludwig Prandtl, who laid foundations for the boundary layer theory at the beginning of the 20th century, is often regarded as the father of modern fluid dynamics [1]. The comprehensive book [2] by Prandtl's student Hermann Schlichting remains relevant in the study of the fluid jet flows today (the first edition was published in German in 1951, since then several revised editions have been published in multiple languages).

The fluid jet is frequently considered a source of momentum [3]. A special significance was given to jets in the design of machines and apparatuses. From the first attempts as was the Heron's engine aeolipile, over the first jet planes (Henri Coanda's prototype plane in 1910, Me-262 operational fighter in 1940s) to the modern usage in the various areas of human activities; Some examples include transportation (aviation, aeronautics and underwater vehicles), energy (heating, cooling, drying and coating technologies, combustion and burners, water jet cutters, cutting torches) and daily life (jet printers, washing machines, cooling of electronics). While some of the applications are still seemingly futuristic, such as 3D printers, they are nevertheless modern applications.

1.1 Motivation

The goal of this thesis is to describe the fluid mechanics and heat transfer of a fluid jet impinging on a circular cylinder, i.e., the flow of a submerged water jet originating from small-sized rectangular nozzles (less than 1 mm, i.e., micro-jet) and with a relatively high

aspect ratio (higher than 100). Both synthetic (SJ) and conventional continuous (CJ) jets are investigated. The task is studied from a fluid mechanical and heat transfer point-of-view.

Generally speaking, CJ can be easily controlled. To facilitate investigations, some parts of complicated SJ experiments can be substituted by simpler CJ experiments. The hypothesis, which is a background for this approach, can be formulated according to the following three points:

- The behavior of CJ and SJ (e.g., regimes of flow separation on a cylindrical surface, including a jet splitting into two parts) are approximately (qualitatively) equivalent for identical Reynolds numbers.
- The average Nusselt number for CJ and SJ are determined by the Reynolds numbers and can be described by the same equations.
- The Reynolds number of SJ can be defined from the extrusion stroke of the SJ cycle.

This hypothesis is proposed considering current knowledge. There is no confirmation available in the literature yet. Moreover, results from macro-scale measurements cannot be used to corroborate micro-scale measurements. A typical example known from impinging CJs is the reduction in the stagnation Nusselt number resulting from a nozzle size decrease, at the same Reynolds numbers.

There are two main reasons for the present work:

1) The fundamental research point-of-view

Many particular topics have been studied extensively: impinging jets, impinging heat transfer, heat transfer from cylinders in a cross-flow, heat transfer from cylinders to impinging continuous jets, as well as the topic of the synthetic jets. Despite this fact, an understanding of all the mechanisms is still far from complete. The mentioned topics belong to a set of fundamental fluid mechanics problems. Surprisingly, to the author's best knowledge, there are no available literature (or data) concerning heat transfer from a cylinder under the impingement of a synthetic jet. Considering previous research, which proves that synthetic jets are useful tools to effectively cool flat surfaces, the use of synthetic jets to cool cylindrical surfaces can also be useful. Thus, obtaining data concerning this specific component of fluid mechanics can yield interesting results.

2) The potential applications

Nowadays, the operation of synthetic jet coolers is not only the privilege of the leading scientific laboratories but commercial products are available for industrial or home usage ([4,5,6], etc.).

On the other hand, there are plenty of applications, where the object that needs to be cooled (or heated), has a cylindrical shape (e.g., heat exchangers, various electronic and optoelectronic elements such as resistors, condensers, optic fibers, various transducers, induction coils, and materials and products in food industry, etc).

It is just a matter of time when the need of thermal management of cylindrical surfaces can be satisfied by using synthetic jets (in industrial or everyday home applications). Therefore, this work might contribute to the knowledge of this application field.

1.2 State of the art

In this section, an overview and summary of relevant academic literature and research studies is provided. The overview is focused on continuous 2D submerged jets, synthetic jets (especially 2D), jets with low Reynolds numbers, micro-jets, convective heat transfer, heat transfer using synthetic jets and heat transfer from circular cylinders.

1.2.1 Continuous jets

Free jet flows are jets which are not directly influenced by any walls. This category includes a free jet (a source of momentum), a plume (a source of buoyancy), a mixing layer or a wake flow [2,3]. The category free jet includes free-surface jets and submerged jets.

- The submerged jet is a jet which is issuing into surroundings with approximately the same properties as the jet itself (typically water-to-water jet, air-to-air jet, etc.).
- The free-surface jet is a fluid jet flow which is emitted into its surroundings created by the fluid with different properties (typically liquid-to-gas jet).

Note here some uncertainty and discrepancy in terminology: An expression "free jet" is sometimes used as a shortened expression for the "free-surface jet," whereas sometimes the phrase "free jet" emphasizes the absence of solid surfaces in the test section. In the latter case, the "free jet" is (for both free-surface and submerged jets) used to distinguish the jet occurring

far from surfaces from all other jets interacting with surfaces such as wall jets, impinging jets and jets deflected by the Coanda effect.

From a geometrical point-of-view, the two largest sub-categories of submerged jets are round or axisymmetric jets (i.e., those originating from round or axisymmetric orifices or nozzles) and plane jets (those originate from long slot orifices or nozzles).

Both round and plane jets have been widely studied as one of the basic topics of fluid dynamics. The theoretical solution of this type of jet can be found in the available literature (e.g. [2,3]).

Considering this terminology, the present study deals with submerged jets issuing from a slot nozzle in general, and with this jet impinging onto a circular cylinder.

1.2.1.1 Turbulent plane jet

Fig. 1.1 shows a scheme for a plane turbulent jet model (the scheme was adapted from [3]).

After the discharge of the jet from the slot, the three regions of the jet can be distinguished:

I) The initial region

This region is characterized by the presence of the potential core, i.e., the part of the jet where the exit velocity of the jet, U_e, is kept. In the potential core, the influence of viscosity is not

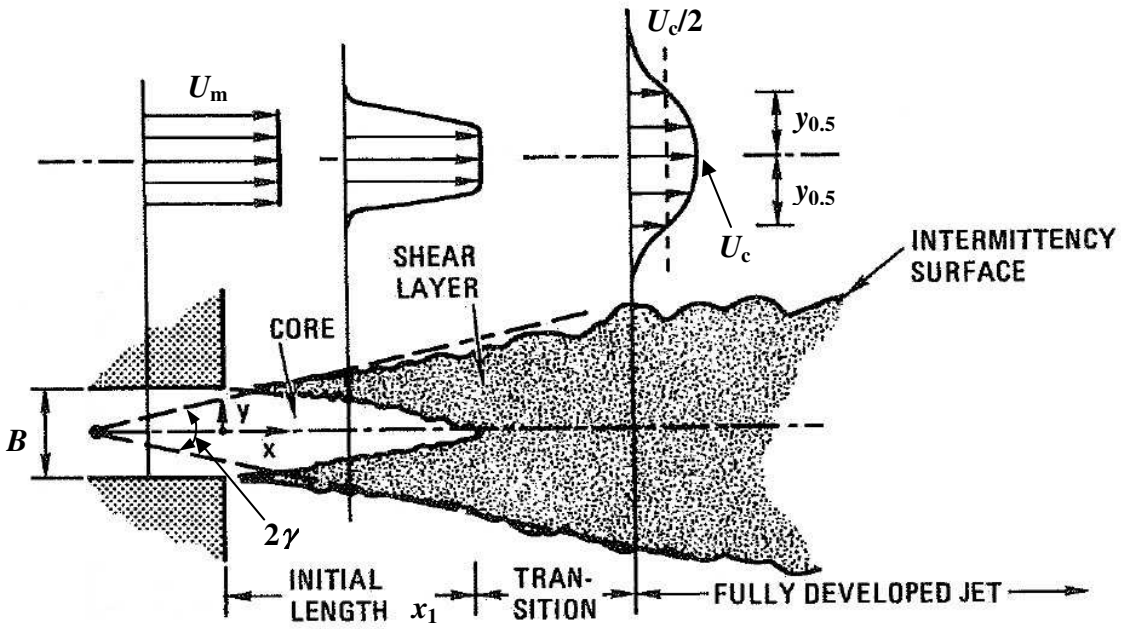

Fig. 1.1 Scheme of the plane turbulent jet (adapted from Blevins [3] and modified).

employed, the fluid keeps its initial direction. The width of the potential core gradually decreases as the fluid is mixed with the quiescent surroundings in the shear (mixing) layer out of the jet core. The accompanying effect of the mixing process is the increase of the velocity fluctuations in the mixing layer. The initial region ends with the boundary of the potential core, at an approximate distance $x_1 = 6B$ (where B is the width of the nozzle slot) for turbulent jets [3].

II) The transition region

III) The region of the fully developed jet

The velocity profiles become self-similar (another term is self-preserving) in this region (approximately from $x = 20B$ [7]). To characterize the widening of the jet along the downstream direction, the half-width of the jet $y_{0.5}$ is defined as the transverse distance for axial velocity U to fall to one-half the of the centerline value U_c , where $U_c = U_{max}$ in this case (see e.g., Blevins [3]). The self-similar velocity profiles collapse into dimensionless form onto one curve. Several authors propose theoretical solution of the dimensionless velocity profile. For example, a solution according to Blevins [3] is characterized

$$\frac{U}{U_{max}} = \exp\left[-57\left(0.11\frac{y}{y_{0.5}} \right)^2 \right], \tag{1}$$

where the half-angle of the jet is approximately $\gamma = 6.3°$.

Just note here that also for plane laminar jets, the solution of the velocity profiles can be found in the literature, e.g., Bickley [8]:

$$\frac{U}{U_{max}} = \mathrm{sech}^2\left(0.88136\frac{y}{y_{0.5}} \right). \tag{2}$$

The profiles of the turbulent velocity fluctuations become self-similar further downstream, approximately at $x/B = 40$ (see Gutmark and Wygnanski [9]).

The centerline velocity, U_c, decays with the axial distance as $U_c \sim x^{-0.5}$, which is frequently named as the "half-power law" (see e.g., [10]). For comparison purposes, it should be mentioned that in the axisymmetric case decays faster, $U_c \sim x^{-1}$.

1.2.1.2 Rectangular turbulent jets

To achieve a truly 2D plane jet is practically impossible in real-world devices. The ideal plane jet streams fluid from a slot of infinite length. Therefore, in the theoretical or numerical studies the pure 2D jet flow, without the third component, can be assumed. Although the computational process can be considerably simplified and shortened using a 2D approach, the results are only an approximation and simplification of reality.

In the experimental praxis, the plane jets are usually realized by means of rectangular slots with high aspect ratios (AR), i.e., the ratio between the lengths of a long and a short side of the slot. Because the AR can never reach infinity, finite slot length generate so-called end-effects, which include the mixing and entrainments along the short sides of the slot (contrary to the pure 2D case). Other specific features result from the edge effects. The mixing-layers along the edges of the slot meet, interact and merge, which brings about new jet phenomena. Finally, a 3D jet character is developed as will be discussed in the following text.

A reasonable approximation of the theoretical plane jet can be achieved using the sidewalls along the short sides of the exit slot. By applying the sidewalls, the quasi-plane jet can be obtained. It is fair to add a penalty of this approach here: boundary layers are developed on the sidewalls. This effect can be negligible in the near-field; however, it contaminates the far field.

The majority of existing research is concerned with rectangular jets. The terms "plane jet" and "rectangular jet" are often confused in the relevant literature. Thus, it should be specified here that the following text concentrates solely on incompressible rectangular jets, i.e., the jets issuing from finite-sized orifices or nozzles, with rather low Reynolds numbers. A Reynolds number is commonly defined as $Re = U_m B/\nu$, where U_m is the mean exit velocity, B is the characteristic dimension (which is usually the width of the slot) and ν is the kinematic viscosity. More details and parameter definitions used in this study will be presented in Chapter 4.

Sforza et al. [11] presented a study on three-dimensional, free submerged jets and a year later Trentacoste and Sforza [12] extended their work and performed a more detailed study on the same topic. According to their general findings, the turbulent incompressible 3D jet can be divided into three regions 1, 2, 3 [11,12]. Note that region 1 (potential core) exactly agrees with the "initial region" of the well-known classification characteristics; on the other hand, regions 2 and 3 specify the 3D character of these jets [11,12]:

1) The potential core region – mixing is initiated at the jet boundaries, however, the mixing does not affect the entire flow and thus the velocity on the jet axis and its surroundings remain constant.
2) Characteristic decay region – the velocity on the jet axis begins to decay. The slope of the decay depends on the exit geometry, i.e., for the initial 2D jet, the centerline velocity obeys the half-power law, $U_c \sim x^{-0.5}$. The velocity profiles on the minor axis are self-similar, while the velocity profiles on the major axis are not self-similar.
3) Axisymmetric decay regions – the slope of the centerline velocity decay is not dependent on the exit geometry anymore; instead the velocity decreases with the slope as is typical in an axisymmetric case, $U_c \sim x^{-1}$. The velocity profiles in both axes are similar here. Further downstream, the fully developed region appears.

The variation of the exponent *n,* in the velocity decay $U_c \sim x^{-n}$, in the characteristic region with the inverse value of the aspect ratio, $e = 1/AR$ is shown in Fig. 1.2. Fig. 1.2 shows that the transition between the 2D case and the axisymmetric case is characterized by a non-monotonic relationship between *n* and *e*. A value of $n = 0.5$ is relevant to the 2D jets (in reality AR = 100). An increase in *e* causes a gradual decrease of *n*, thus the lowest value of $n = 0.33$ was found for AR = 10. Then, an increasing *e* causes a gradual increase of *n*, thus the

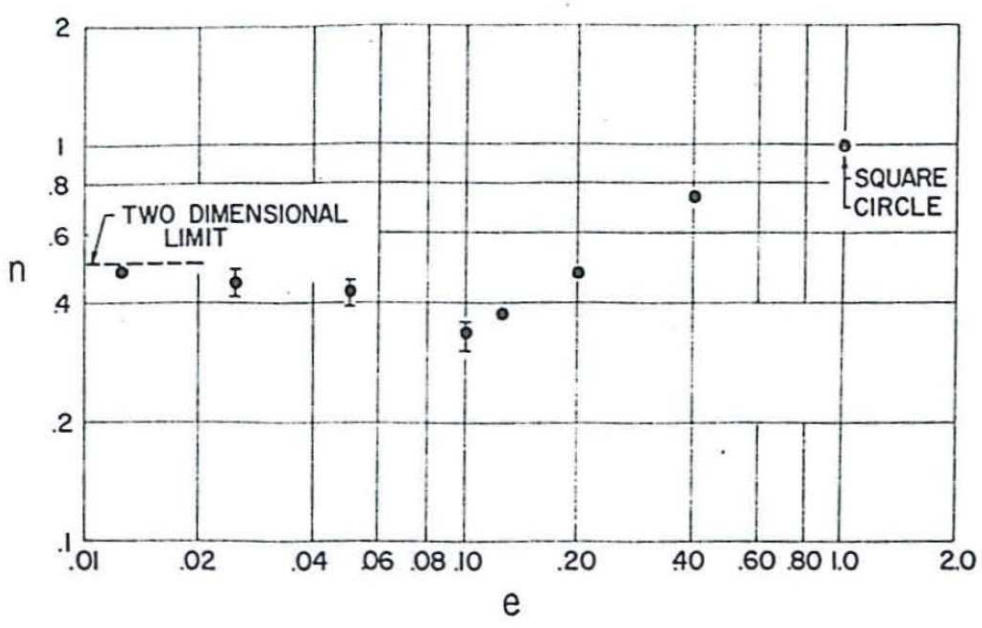

Fig. 1.2 The variation of the exponent *n* of the velocity decay $U_c \sim x^{-n}$ in the characteristic region with the inverse value of the aspect ratio, $e = 1/AR$ (adapted from Trentacoste and Sforza [12]).

maximum value of $n = 1$ was found at $AR = 1$ (i.e., cases of square and round jets). The authors in [11] compared their data associated with lengths of the potential core region and the lengths of the characteristic decay region with some data available in the literature. The results indicated that the location of the individual regions for turbulent incompressible jets is not dependent on an exit velocity (i.e., on the Reynolds number) but purely on the exit geometry of the jet. Similar regions in the rectangular jets were identified by Mi et al. [10].

The general properties of the rectangular turbulent jets were investigated by many other authors, see e.g., Lemieux and Oosthuizen [13], Namer and Ötügen [14], Deo et al. [15], Deo et al. [16], just to name a few.

As discussed earlier, to promote the 2D-nature of the rectangular jet the sidewalls along the short sides of the slot, another paper by Deo et al. [17]. A substantial influence of the sidewalls on the overall character of the jet was proven. While the jet with sidewalls is considered a plane jet, the jet without sidewalls, even with the AR = 60, is rather 3D in character.

Rectangular jets without sidewalls are often connected to an axis-switch, i.e., a three-dimensional deformation of the jet cross section due to jet spreading in the major- and minor-axis planes (Zaman [18]) and a saddle-back velocity profile phenomena.

Trentacoste and Sforza [12] observed the axis-switching phenomenon, and although there was no explanation of this phenomenon, the saddle-back (saddle-shape) velocity profiles were identified in the jet with AR = 10. The shape disappeared at the beginning of the axisymmetric decay region and agreed with the position of the axis-switching point.

Tsuchiya et al. [19] studied characteristics of rectangular air jets, including velocity and temperature profiles, and identified the saddle-back velocity profiles for an orifice-type jet, both in terms of the velocity and temperature. Ratios of the off-axis peaks, over the centerline (saddle) values, are higher for the temperature profiles. These ratios were approximately 1.5 (at $x/B = 5$) and 1.2 (at $x/B = 7$) for the temperature and velocity profiles, respectively. Both peaks (on the temperature and velocity profiles) move toward the jet axis and consequently disappear around $x/B = 11$, without reaching the axis. The positions of the velocity peaks correspond to the local minima of turbulent fluctuations of the velocity. The authors attribute the peaks to the regions of retarded mixing. The phenomenon of axis-switching is also documented, both for the orifice and nozzle type geometries and both the velocity and temperature profiles (although the term “axis-switching” is not used here).

More recently, Vouros et al. [20] investigated the near field of a rectangular jet issuing from sharp-edged orifice. The authors presented velocity and vorticity distributions in planes parallel to the exit plane for several distances from the exit orifice (x/B = 0–30). The evolution from the uniform initial velocity distribution, over the deformation into a "dumbbell-like" shape, to an almost axisymmetric velocity distribution was shown. Around x/B = 30, the beginning of the axis-switching was apparent. The expected saddle-back profiles were observed from the axial distances x/B = 5 to 10. The local minima of the velocity fluctuations correspond to the position of the off-axis velocity peaks, indicating that the shear layer fluctuations had not yet penetrated these areas, thus these areas could be called the "potential core" regions. The velocity in the peaks remained close to the exit velocity; its relative value was about 20% higher than the centerline velocity.

1.2.1.3 Microjets and very low Reynolds number jets

The term "microjet" is used to express small cross-section jet sizes – usually when at least one dimension is lower than 1 mm, see Cabaleiro and Aider [21].

One of the earlier studies, which considered the problem of microjets (in the contemporary terminology) and low Reynolds-number jets was performed by Sato and Sakao [22]. They performed very careful experiments in air focused on the stability of very thin rectangular jets (i.e., microjets in the contemporary terminology) at very low Reynolds numbers from 8 to 800. It should be note here that the authors in [22] used a Reynolds number based on the maximal on-axis velocity of the jet. To make this text consistent, the values used here were recalculated to assume an ideal laminar parabolic profile with a ratio of the maximum and orifice-mean velocities equal to 1.5. Two nozzles were used with widths of 0.2 and 1.1 mm. The aspect ratios were 150 (for Re = 8–133) and 91 (for Re = 213–800), respectively.

Using hot-wire anemometry, the authors found that when the Reynolds number is less than approximately 6.7, the whole jet is laminar. By increasing the Reynolds number, periodic velocity fluctuations appeared in the jet, however they decay further downstream without developing into the irregular fluctuations. When the Reynolds number was higher than approximately 33, the periodic fluctuations developed (gradually) into irregular, turbulent fluctuations.

The observations by Sato and Sakao [22] were in accordance with the value stated by Blevins [3]: the maximal Reynolds number for a laminar jet is around 30. A similar critical value is

also reported for an axisymmetric jets by Bejan [23] (Re < 10–30, where Re is based on the exit diameter).

Despite the earlier study by Sato and Sakao [22], the wider interest in micro-jets is relatively new. Probably the first experimental study focusing exclusively on fundamental features of this phenomenon was introduced by Gau et al. [24]. Using hot-wire anemometry, they investigated air jets with three different slot nozzles with the widths of 50, 100 and 200 μm, and with corresponding aspect ratios 10, 20 and 40. The Reynolds number was determined to be in the range from 16 to 320. The experiments reveal several unexpected results, therefore the authors named the paper [24] "*Peculiar phenomenon of micro-jet-flow*". Using flow visualization, the vortex formation process, and subsequent merging of two neighboring vortices, usually seen in macro-scale jets is missing in micro-scale jets. The spectra of the velocity fluctuations did not reveal any fundamental frequencies or subharmonics. The centerline velocity decays more slowly and the corresponding turbulence intensity has a slower rise in the near field compared with large-scale jets. The authors attribute this behavior to the small amplification rate of the instability waves, the absence of a vortex formation, and the low interactions between a micro-jet and its surroundings.

The breakdown point of micro-jets was studied in [24] and the position of the breakdown (L_b) is dependent only on the jet's exit velocity, and surprisingly not on the Reynolds number, i.e., the jets with the same Reynolds number but different slot widths have different breakdown lengths. In other words, conclusions by [24] deconstruct abilities of a similarity considerations in this task. The correlation between the Reynolds number and the dimensionless breakdown length was found in [24] as

$$\frac{L_b}{B} = \frac{14\ 136}{Re}, \tag{3}$$

which can be rewritten (for $Re = U_m B/\nu$) as

$$L_b = \frac{14\ 136\nu}{U_m}. \tag{4}$$

According to [24], the transition process between a laminar and turbulent jet resembles the transition of a laminar boundary-layer flow; this is because the energy for the instability

waves is accumulated gradually until reaching its critical value. As the jet reaches its critical level of the energy, the distinct changes in both the centerline velocity and turbulence intensity occur. This relates to its sudden jet expansion, i.e., its breakdown. The critical Reynolds number is based on the jet's exit-velocity and breakdown-length; in this test, the recorded value was Re_c = 16,013.

The topic of the breakdown of the low Reynolds number rectangular jet and laminar-turbulent transition was studied also by Muramatsu and Tsuchiya [25]. The similar topic was investigated by Lemanov et al. [26] for an axisymmetric micro-jets.

Cabaleiro and Aider [21] performed the experiments and the direct numerical simulation (DNS) concentrated on the axis-switching of a pulsed micro-jet. The exit nozzle had the width B = 380 μm and the aspect ratio 6.5. The phenomenon of the axis-switching is usually attributed to the presence of the vortical structures in the jet. Although, according to Gau et al. [24] the micro-jet is vortex-free, Cabaleiro and Aider [21] proved the existence of the axis-switching in the examined micro-jets of the Reynolds numbers 263.5 and 137. The detailed DNS revealed the existence of the vortex ring in the close vicinity of the exit orifice and it is believed this vortex ring is responsible for the axis-switching in the examined cases.

Gau et al. [24] concluded a complete absence of the vortices in the microjet while Cabaleiro and Aider [21] claim the existence of the vortices and their necessity because of the axis-switching phenomenon. However, these seemingly contrasting conclusions [21] and [24] are valid only for specific parameters (for pulsed [21] and continuous micro-jets [24]) that cannot be generalized. Nevertheless, the topic of the (pulsed and continuous) micro-jets remains still quite unexplored.

1.2.2 Synthetic jets

A synthetic jet (SJ) is a reversible pulsating jet that is generated from fluid oscillations during a periodic fluid exchange between an actuator cavity and its surroundings. A typical SJ actuator has a cavity with an oscillating wall (diaphragm or piston). The cavity is opened to its surroundings via some orifice or nozzle. Mechanical energy is transferred from a transducer, via an oscillating wall, to the fluid. The transducer is either separate from the actuator or it can be integrated into the cavity. This method was proposed by Dauphinee [27] who designed and used a laboratory air-jet generator – likely the first SJ actuator using today's terminology. Note that the "synthetic jet" expression originated from James et al. [28] and Smith and Glezer [29]. A time-mean mass flux through the SJ actuator orifice is zero,

therefore SJ is frequently named as the zero-net-mass flux jet; this phrase is credited to Cater and Soria [30]. A meaningful advantage of a SJ is its relatively simple arrangement: neither blower nor fluid supply piping is required. SJs have been investigated via experimental, theoretical and numerical methods – Mallinson et al. [31], Glezer and Amitay [32]. The flow field regime of SJs and the necessary conditions for SJ existence (formation criteria) were investigated, e.g., by Holman et al. [33], Zhou et al. [34], Xia and Zhong [35], Trávníček et al. [36], Trávníček et al. [37] and McGuinn et al. [38].

SJs are promising alternatives for various applications of active flow control, such as jet vectoring and exciting (Pack and Seifert [39], Smith and Glezer [40], Tamburello and Amitay [41], Ben Chiekh et al. [42]), flow control/triggering of mean flow development (Hong [43], Watson and Sigurdson [44]), flow control in external aerodynamics (Chen and Beeler [45], Mittal and Rampunggoon [46], Tensi et al. [47]) and flow control in internal aerodynamics (Ben Chiekh et al. [48]).

An interesting application field is convective heat-transfer augmentation. Yassour et al. [49] experimentally investigated the annular-impinging SJ. Since that time, SJs for cooling applications have been investigated by many other authors [50-58], including previous work e.g. [59]. A majority of these studies have focused on air SJ impinging on a wall. An interesting up-to-date problem is the cooling of highly loaded electronic components in micro-channels, e.g., see Lee et al. [60] and Trávníček et al. [61].

The following text introduces experimental studies that focus on plane and rectangular SJs, where the SJ flow formation and development were investigated using the manner, methods and parameters that are relevant to the present study. Smith and Glezer [29] studied experimental air-SJs emissions from a rectangular nozzle with AR = 150, a Reynolds number (Re_{SJ}, based on the time-mean exit velocity) varied between 104 and 489. Very detailed measurements of the near-field formation and subsequent jet evolution was performed. While in the near-field, the time-periodic behavior is dominant (due to the passing of individual vortex pairs), further downstream, the vortex structures undergo the transition to turbulence, coherence loss and the jet resembles a conventional turbulent continuous jet. Some differences can be found; for example the velocity decay is faster, the velocity decreases with a power of -0.58 (instead of -0.5), the half-width of the jet increases a power of 0.88 (instead of 1) and the flow rate increases like $Q \sim x^{0.33}$ while a conventional jet $Q \sim x^{0.5}$.

Amitay and Cannelle [62] used PIV and hot-wire anemometry to study the influence of the Reynolds number and the aspect ratio on SJ flow fields. The parameters fall between the

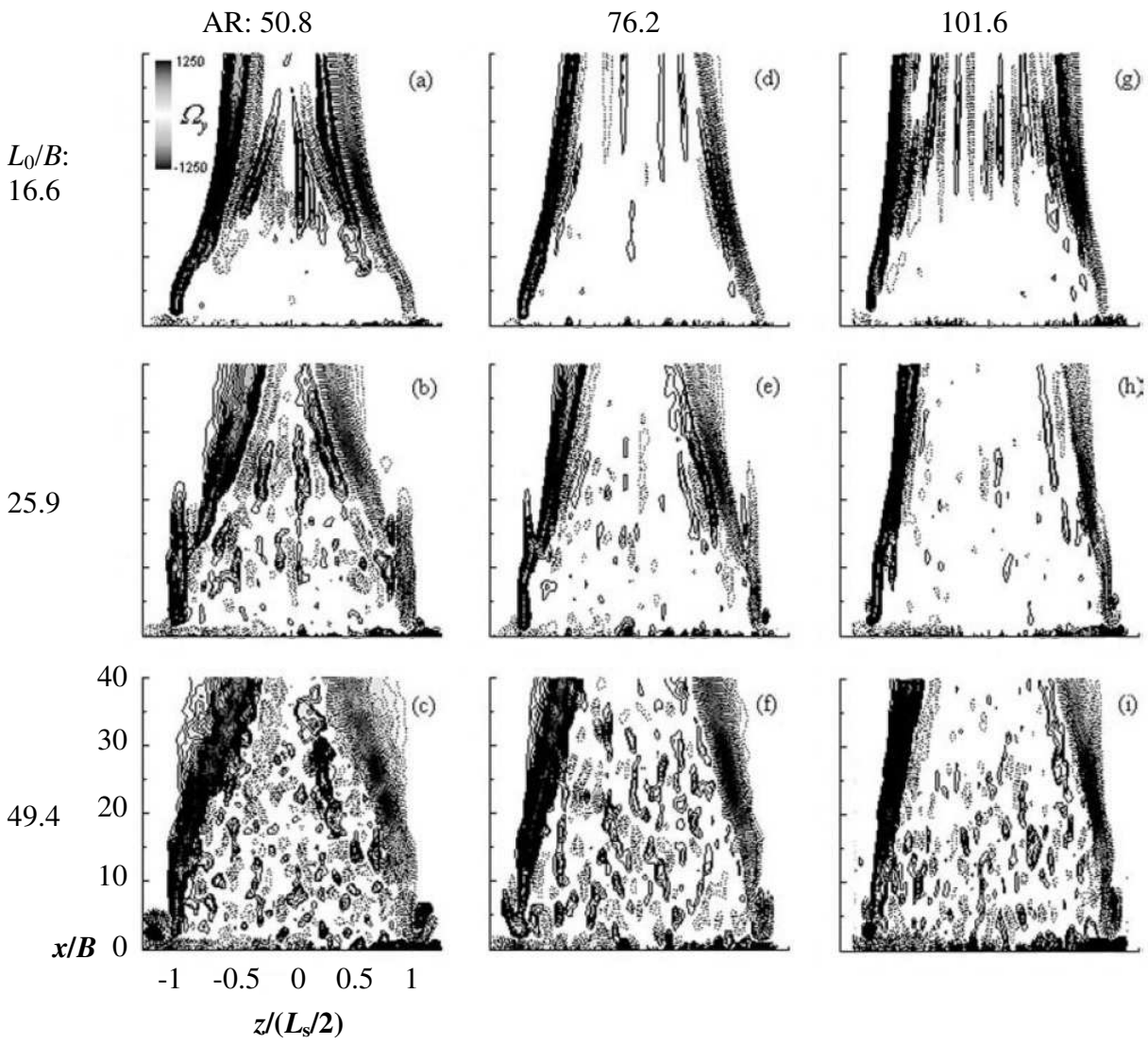

Fig. 1.3 The mean vorticity contours of the rectangular synthetic jet with $f = 300$ Hz (adapted from Amitay and Cannelle [62] and modified).

following ranges: $85 < Re_{SJ} < 364$, $16.6 < L_0/B < 49.4$, AR = 50.8, 76.2, 101.6 (where L_0 is the stroke length of the jet). Regardless of the stroke length, with the increasing aspect ratio the jet width is reduced and so are the entrainment and velocity decay rates in the far field due to the smaller edge effects of the induced velocity. The lower decay rate for the lower aspect ratio is attributed to the large influence of the 3D jet effects. The span-wise velocity profiles of the mean stream-wise velocity component revealed that the initially uniform velocity profile changes into a noticeably non-uniform velocity distribution further downstream. However, this feature is less marked with an increasing Reynolds number while keeping a constant aspect ratio. The mean vorticity contours (see Fig. 1.3) revealed an interesting phenomenon - the existence of a streaky-like vorticity pattern. At the lowest stroke length ($L_0/B = 16.6$) in the near field, the flow is uniform, with no vorticity concentrations along the

span, except those at the edges, which relate to entrainment effects. Further downstream ($8 < x/B < 35$), the streaky-like vorticity pattern appears (see Fig. 1.3). Its existence corresponds to the instability waves, at $x/B = 25$ the wavelength is approximately $0.115L_s$ (where L_s is the slot length). As the aspect ratio increases, the span-wise distance between streaks decreases. As the stroke length increases, the streaks gradually disappear as well and the vorticity field becomes more disorganized and change into randomly distributed vorticity structures.

Gillespie et al. [53] examined convective heat transfer from a heated plate. The impinging SJ emanated from a rectangular orifice with an AR = 25 at the maximum $Re_{SJ} = 450$. PIV experiments showed axis-switching occurred in the jet at around $x/B = 15$. The position of the axis-switching corresponds to the local minimum of the centerline velocity. Organized structures and a vorticity concentration in the inner parts of the jet (named previously as streaky-like structures by Amitay and Cannelle [62]) were also reported. Stream-wise velocity profiles exhibited a non-uniform velocity distribution. At the distance $x/B = 10$, three distinct peaks were visible (one at the centerline, two at the edges). The peaks are associated with the counter-sense vorticity distribution (i.e., the streaky-like structures). After the jet axis is switched, the central peak disappears. Another paper that deals with the topic of rectangular SJ include, e.g., Béra et al. [63], Yao et al. [64] and Abdou and Ziada [65].

1.2.3 Convective heat transfer

The topic of jets is closely bounded to the topic of convection or *convective heat transfer*, particularly when the jets interact with solid body surfaces. The *convective heat transfer* is caused predominantly by the macroscopic motion of fluid particles (see [66,67]).

Two main subcategories of convection can be distinguished:

1) Free (or natural) convection - a fluid motion is driven by density gradients that produce a buoyancy force. The density gradients are mainly caused by the presence of temperature gradients. When a solid body is immersed in a fluid and heated, it works as an energy source (e.g., a line source in the case of a cylinder) and fluid motion is created above the body. This is usually called a buoyancy jet or plume (see Schlichting [2]).

2) Forced convection - a fluid motion is produced by an external source (pump, compressor, etc.).

In some cases, the combination of both types of convection may occur. This type is usually called mixed convection. The crucial factor that determines the type of convection is the ratio Gr/Re^2, usually called the Richardson number, Ri (see e.g., Dumouchel et al. [68], Seutiens et al. [69]). In general, free convection can be neglected if $Ri << 1$; while, forced convection can be neglected if $Ri >> 1$. A mixed convection is considered in the case $Ri \approx 1$ (see Incropera and De Witt [66]). A more precise determination of the critical Richardson number depends on the chosen geometry. For a heated cylinder, the critical value is approximately 0.5 (see Morgan [70], Fand and Keswani [71]). Mixed convection needs to be considered when the Richardson number is approximately the critical value.

The governing parameter for a natural convection is the Grashof number, which is the ratio of the buoyancy and the viscous forces. The Grashof number is characterized by

$$Gr = \frac{g\beta(T_w - T_\infty)D^3}{\nu^2}, \tag{5}$$

where g is the acceleration of gravity, β is the volumetric thermal expansion coefficient, D is the characteristic dimension (i.e., the diameter of the cylinder in this case), T_w is the wall temperature and T_∞ is the bulk temperature.

The forced convection is characterized by the Reynolds number Re (the ratio of the inertial and the viscous forces).

The evaluation of the convective heat transfer differs considerably with geometry. The following section is focused on the convective heat transfer from horizontal cylinders.

In general, (if the compressibility or high velocities are not considered) the overall convective heat transfer is expressed by the following equation ([70]):

$$Nu = f(Gr, Pr, Re, T_w / T_\infty), \tag{6}$$

where Nu is the average Nusselt number over the entire cylindrical circumference, T_w is the (surface) wall temperature, and T_∞ is the bulk (ambient) temperature. The Prandtl number, Pr, is characterized by

$$Pr = \frac{\nu}{\alpha}, \tag{7}$$

where α is the thermal diffusivity.

The average Nusselt number is defined as

$$Nu = \frac{hD}{k}, \tag{8}$$

where h is the average heat transfer coefficient, D is the characteristic dimension (here the cylinder diameter) and k is the thermal conductivity of the fluid. In this work, k is always evaluated using the film temperature $T_f = (T_w+T_\infty)/2$ via the formula for water provided by Pátek et al. [72]. Note that T_∞ is coincident with the jet temperature at the slot exit.

When the local Nusselt number is requested, the local heat transfer coefficient should be known and the overall Nusselt number is obtained via the integration of the local contributions. In this work, the term Nusselt number is used for the average Nusselt number over a cylindrical surface, unless stated otherwise.

The present study deals with the overall heat transfer, but the local heat transfer (thus the local Nusselt number distribution) is briefly mentioned to explain the importance of the governing parameters. The local Nusselt number distribution depends on the boundary layer development along the cylinder's circumference. In the case of natural convection, the boundary layer begins at the lowest point (or line) of the cylinder; its width gradually increases as the top is reached. The boundary layer is then separated and a plume is created above the top of the cylinder. In case of a laminar boundary layer, the local Nusselt number has a maximum at the bottom of the cylinder that decays monotonically upwards (see [66]).

The thermal boundary conditions must be specified when the heat transfer from the cylinder needs to be evaluated. Two basic boundary conditions can be assumed: a constant surface temperature and a constant heat flux from the surface. In real situations, the boundary condition is usually not unambiguous and the real boundary condition is a combination of both mentioned approaches. However, in most tasks, one of the conditions dominates and the other one can be neglected. The difference between the Nusselt number based on the constant heat flux (Nu_q) and the constant temperature (Nu_T) is usually in order of percentage units (see e.g., [73]).

In both the natural and forced convection regimes, a very important phenomenon is the laminar-turbulent transition in the boundary layer. The transitions are associated with the (governing parameters) Rayleigh ($Ra = GrPr$) and Reynolds numbers for natural and forced convection regimes, respectively. In natural convection cases, the critical value of Ra for the transition varies between $Ra_C = 10^7$ (Morgan [70]) and 10^9 (McAdams [74]). In forced convection cases, the critical Re value for the transition depends on the flow regime on the cylinder. In fact, the laminar-turbulent transition, in the boundary layer, is one of many transitions occurring in the flow field near the cylinder (see e.g., Zdravkovich [75]).

Both natural and forced convective heat transfer can be controlled by means of passive or active methods. Examples of passive controls in natural convection are vertical or horizontal confinements, which were studied by Atmane et al. [76] and Karim et al. [77], respectively. Each approach led to a significant enhancement of the natural convective heat transfer process.

An example of active control of natural convection was proposed by Penot et al. [78]. They tried to enhance natural convective heat transfer in air via a differentially-heated cavity. Periodical heating was used to induce flow-field actuation effects, resulting in a heat transfer enhancement. While the results confirmed the intended modifications of the flow field via vortex structures, the overall and local Nusselt numbers decreased. This result was attributed to the flow instabilities, which remained in the external boundary layers; thus, they could not have contributed to any heat transfer enhancement on the walls.

Recently, a similar active control approach was tested by Broučková and Trávníček using PIV and LIF techniques ([79], [80]). It was concluded that flow and thermal fields can be effectively controlled by periodical heating; thus, unsteadiness was generated, which resulted in higher velocities and local temperature gradients. However, no heat transfer enhancement effect has been achieved, in accord with the literature (Penot et al. [78]).

1.2.3.1 Natural convection - correlations for the Nusselt number

In natural convection, the available correlations are mostly proposed for an average Nusselt number over the entire isothermal cylindrical surface. Morgan [70] surveyed and collected experimental data and data correlations from many studies and proposed his own correlation based on the accumulated experimental results. His Nusselt number formulation is characterized by

$$Nu = N(GrPr)^m = N(Ra)^m \ . \tag{9}$$

The parameters N and m vary with the range of Ra.

Table 1 Nusselt number correlations according to Morgan [70]

Ra		N	m
from	to		
10^{-10}	10^{-2}	0.675	0.058
10^{-2}	10^{2}	1.02	0.148
10^{2}	10^{4}	0.850	0.188
10^{4}	10^{7}	0.480	0.250
10^{7}	10^{12}	0.125	0.333

The Rayleigh number and the Nusselt number are based on the cylinder diameter and the thermo-physical properties associated with the film temperature T_f.

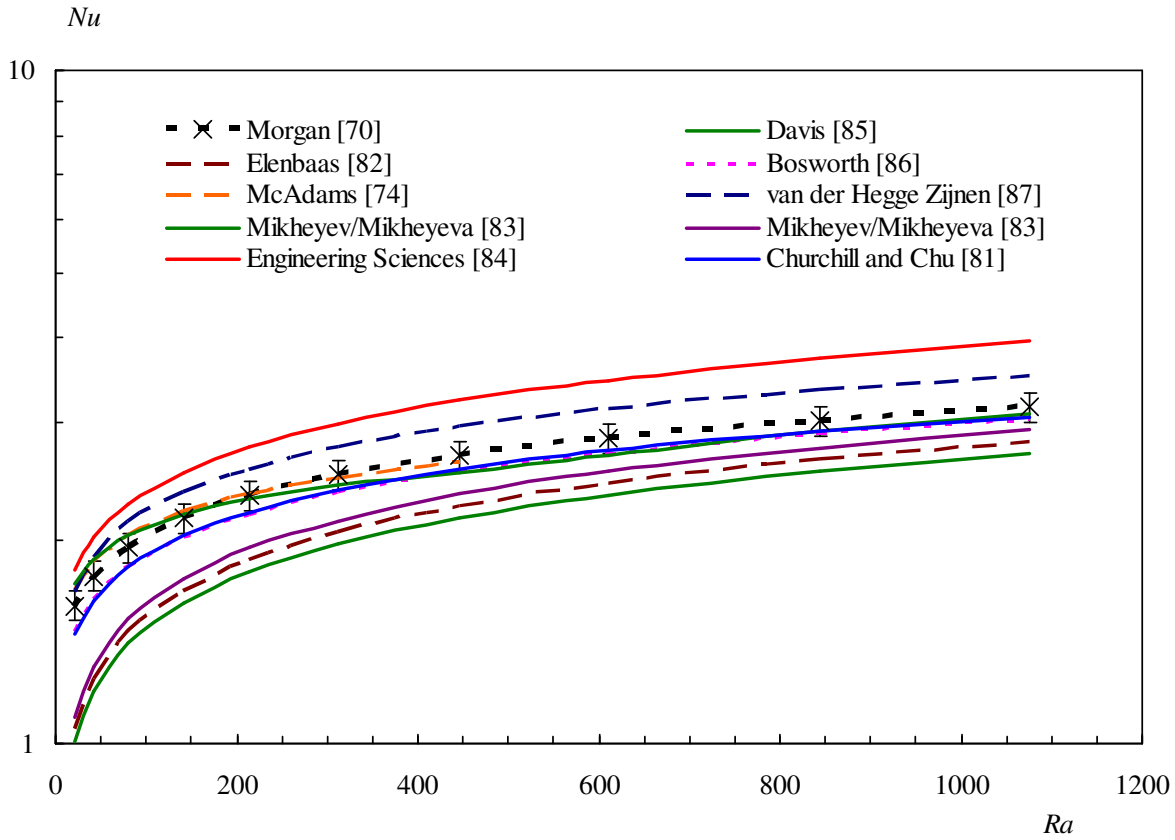

Fig. 1.4 The representative correlations for natural convection regime from collections by Morgan [70], the correlation by Morgan [70] and the correlation by Churchill and Chu [81].

Another correlation was proposed by Churchill and Chu [81] for a complete range of *Ra* that is characterized by

$$Nu = \left\{ 0.60 + \frac{0.387 Ra^{1/6}}{\left[1 + \left(0.559/\mathrm{Pr}\right)^{9/16}\right]^{8/27}} \right\}^2 . \tag{10}$$

The correlations differ from author to author, but in general, they are similar in form to Eq. (10) by Morgan [70]. The representative correlations based on the collection by Morgan [70] (only correlation based on the measurement in water or liquids in general were chosen), the correlation by Morgan [70] (including declared uncertainty) and the correlation by Churchill and Chu [81] are summarized and plotted in Fig. 1.4 (the range was chosen by considering the range relevant in this work, specifically, the present experimental methods were validated via the overall heat transfer from the cylinder under a natural convection regime).

1.2.3.2 Forced convection

Forced convection can be carried out via a cylinder in the uniform cross-flow or using jet impinging onto a cylindrical surface (i.e., impinging jet).

The forced convection from a cylinder to the uniform cross-flow is a widely investigated topic (Morgan [70], Incropera and De Witt [66]) since various regimes depending on the Reynolds number of the oncoming flow can be distinguished (see e.g., Zdravkovich [75]).

One of the most commonly used relations for forced convection of a heated circular cylinder in cross-flow is the theoretically proposed King's law from 1914. It states that there is a square root dependence of the average Nusselt number on the Reynolds number, see Bruun [88]:

$$Nu = A_{Nu} + B_{Nu} Re^{0.5}, \tag{11}$$

where A_{Nu} and B_{Nu} are empirical calibration constants for each fluid.

A generalized form was later proposed by Kramer in 1946 (see Bruun [88]). The form was based on experiments in air, water and oil. The Nusselt number is expressed by

$$Nu = 0.42\, Pr^{0.2} + 0.57\, Pr^{0.33} Re^{0.5}, \tag{12}$$

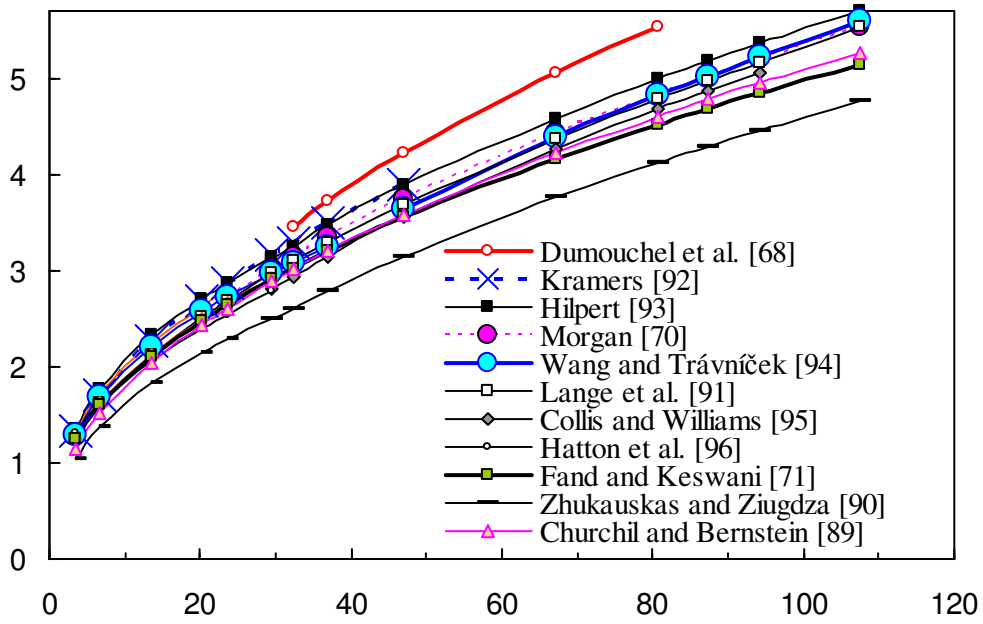

Fig. 1.5 Forced convection from circular cylinder in air cross flow at moderate temperature loading of $T_w/T_\infty = 1.50$.

where the *Nu*, *Pr* and *Re* are evaluated for the thermo-physical properties at the film temperature T_f. Many investigators tried to modify the constants in this equation. A representative collection of references was described by Morgan [70]. Since his time, other correlations were proposed by Churchill and Bernstein [89], Zhukauskas and Ziugzda [90] and Lange et al. [91]. A representative collection of references is presented in Fig. 1.5.

Another task is the (slot) jet impinging onto the cylinder. Depending on the geometry arrangement, several combinations can be distinguished. Two extreme situations are considered here:

1) If the cylinder diameter is very large in comparison with the slot width, then the jet impingement resembles an impingement onto a convex surface.

2) If the cylinder width is much smaller than the jet width, the task resembles the cylinder in cross-flow.

Because of the scope of this work, the following text is focused on the impinging jet (IJ) case.

Note here that (submerged) IJs are in general widely studied due to evident advantages and the potential application possibilities to cooling (e.g., electronic components), heating (e.g., aircraft thermal de-icing systems) and drying (paper or textile industry). IJs are also often used as test cases in CFD computations (for more details about IJ applications see [97]).

According to a general classification, heat and/or mass transfer to or from a fluid jet impinging normally on a flat surface is one of the basic cases of forced convection in external flows (see [66]). IJs are capable of achieving the highest forced convection heat/mass transfer rate between a single-phase fluid flow and a solid wall. Therefore, the IJs attracted attention in many heat/mass transfer studies (see e.g., the comprehensive monograph by Martin [98]).

1.2.3.3 CJ impingement heat transfer

In addition to the case of a jet impinging on a flat surface, several experimental studies dealing with a (slot, continual) jet impinging on a circular cylinder can be found in available literature.

Schuh and Persson [99] performed a heat transfer study on an air jet impinging onto a circular cylinder. The Reynolds number based on the cylinder diameter, Re_D, was around 6,000 to 50,000, the cylinder diameter was $D = 19.5$ mm, the width of the nozzle was adjustable between $B = 1.2$ to 50.0 mm. In this work, the overall heat transfer coefficient h on the cylinder was investigated. The relationship between the heat transfer coefficient h and the dimensionless nozzle-to-cylinder distance *(H/B)* is shown in Fig. 1.6. The evaluated heat transfer coefficient h is related to the overall heat transfer coefficient for a cylinder in cross-flow h_∞. For comparison purposes, the centerline velocity decay is also plotted in Fig. 1.6. If the cylinder is placed immediately after the nozzle exit, the jets with smaller B reach a higher heat transfer coefficient than the larger ones. The reason is the low turbulence level in the case of the jets from larger nozzle, i.e. the cylinder is fully submerged in the jet potential core. In the case of the narrower jets, the cylinder is influenced by the higher turbulence level connected with the outside shear layer. As the nozzle-to-cylinder distance increases, the coefficient h increases for moderate nozzle widths ($B = 5$ to 20 mm) and achieves its maxima around $x/B = 8$, but then quickly drops again. The distance where the maximum occurs corresponds to the position immediately behind the end of the jet potential core, i.e., the position where the jet velocity is still comparable to the exit velocity, but the jet has a higher turbulence level than the potential core. The curves for jets with small B/D ratio do not have any maxima and monotonically decay from the start. Conversely, the coefficient h of the jet

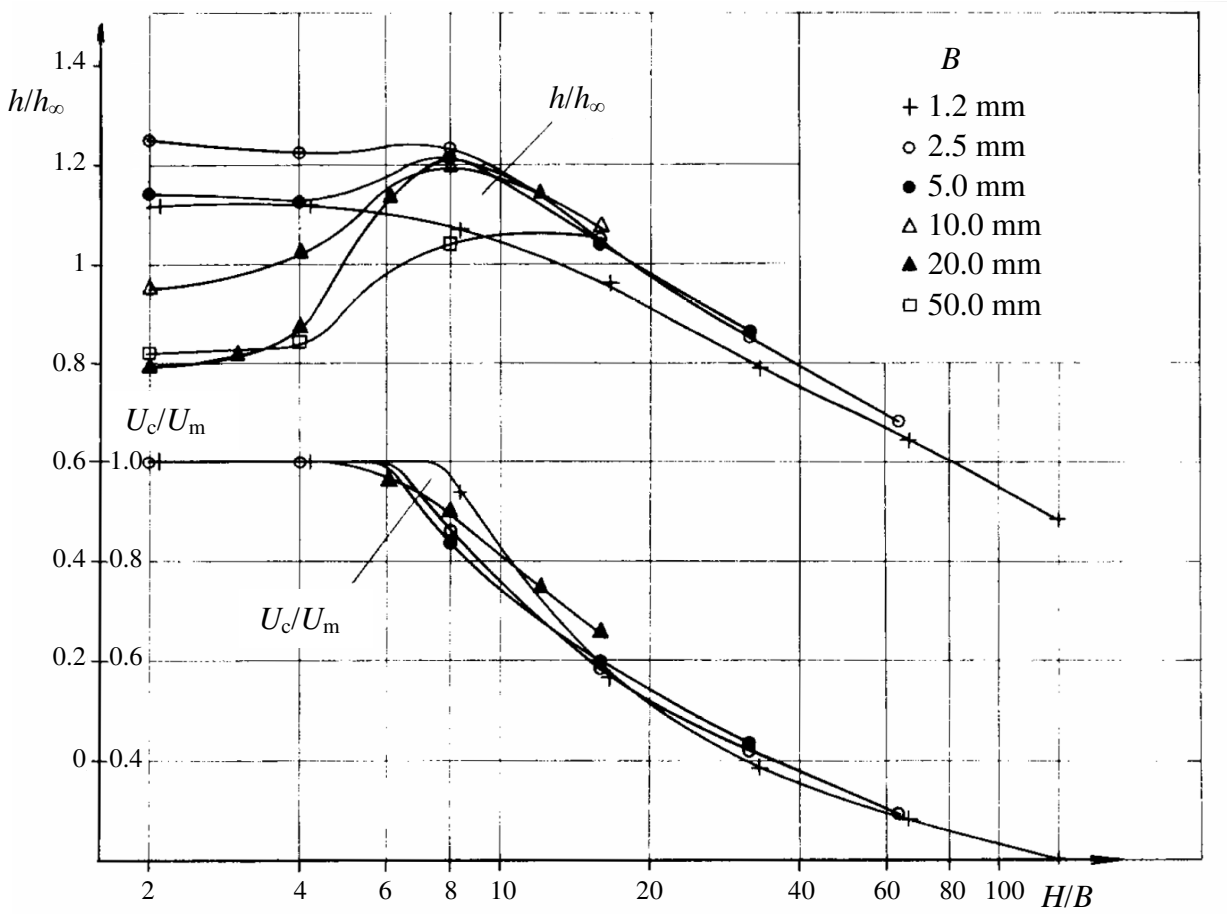

Fig. 1.6 Heat transfer coefficient h of a cylinder of 19.5 mm diameter (h_∞ is the heat transfer coefficient of the cylinder in the cross-flow) and the centerline velocity decay (modified from Schuh and Persson [99]), Re ~ 35,000-50,000.

from the biggest nozzle increases gradually. At larger distances, the heat transfer coefficient values for all jets tend to lie on a single curve (all the jets are much wider than the cylinder).

McDaniel and Webb [100] studied heat transfer from a cylinder using an impinging slot jet issued either from a sharp-edged or rounded nozzle. The working fluid was air. The Reynolds number, Re_D, ranged between 600 to 8,000, D/B = 0.66-2 and the dimensionless nozzle-to-cylinder distance was H/B = 1-11. The slot jet achieves a higher heat transfer rate (the increase was approximately 1.2 to 2 times) when compared to an infinite flow with the same average velocity. This is attributed to the increased turbulence in the slot jet configuration. Furthermore, nozzles with a sharp-edged orifice lead to higher heat transfer rates over the contoured nozzle. Moreover, the heat transfer using a contoured nozzle was almost independent of the Reynolds number, while the heat transfer using a sharp-edged nozzle increased significantly as the Re increased. The difference in heat transfer between both types of nozzles are attributed to the different velocity profiles; the contoured nozzle

yields a uniform velocity profile, while the sharp-edged nozzle, due to the vena contracta effect, yields a highly non-uniform velocity profile; it also achieves the highest velocity on the jet axis and the high velocity gradients in the shear layer. The optimal non-dimensionless distance was found to be H/B = 5-6 and 2-4 for contoured and sharp-edged nozzles, respectively. The optimal distance corresponds to placing the cylinder on the tip of the potential core of the jet. McDaniel and Webb [100] also singled out three flow field types depending on the position of the cylinder in the jet:

(A) The cylinder is fully submerged in the jet's potential core. A separation may occur and the back side of the cylinder is poorly covered and heat transfer is relatively low.

(B) The cylinder is placed near the tip of the potential core. The velocity is mostly unaffected by the still ambient fluid and the fluid remains attached to the cylinder surface, which yields higher heat transfer.

(C) The cylinder is placed downstream the potential core, the decreased velocity yields decreased heat transfer.

The proposed correlation equation is characterized by

$$Nu = 0.28 Re_D^{0.59}. \tag{13}$$

(Re = 600-8,000, D/B = 2, H/B = 9-11)

Gori and Bossi [101] investigated the optimal slot width to cool a circular cylinder via IJ in air. The cylinder diameter was D = 10 mm, the Reynolds number, Re_D, ranged from 4,000 to 22,000, B/D = 0.25-1, the slot nozzle length was L_s = 135 mm, nozzle-to-cylinder distance varied between 2B and 20B. The optimal nozzle-to-cylinder distance was found to be x = 8B. These results agree with the findings by Schuh and Persson [99]. The maximum Nu (based on the cylinder diameter) was obtained for the slot with ratio B/D = 0.25. The maximum Nu (based on slot width) was obtained for a slot with ratio B/D = 0.5, which is considered the optimal slot ratio. The correlation equation is characterized by

$$Nu = 0.10\left(\frac{H}{B}\right)^{-0.35} Re_D^{0.83}. \tag{14}$$

(Re = 4,000-22,000, D/B = 4, H/B = 8-20)

Bartoli et al. [102] performed experiments in water that focused on the cooling of a circular cylinder. The cylinder diameter D and a slot width B had the same order of magnitude ($D = 2.5$ and 3 mm, $B = 2$ and 3 mm). The length of the slot is $L_s = 100$ mm. The nozzle-to-cylinder distance H/B varied from 1.5 to 10. The Reynolds number, Re_D, was in the range from 1500 to 20,000. The maximum Nu is determined by the distance ranging from H/B = 4 to 7. Singularities were found in the Nu-Re relationship. The phenomenon is attributed to changes of the flow pattern around the cylinder, namely to the variations of the separation angle. Thus, the results suggest that the correlation equation is characterized by

$$Nu = 0.52 Re_D^{0.51} Pr^{0.4} \tag{15}$$

(jet reaches the cylinder from below with Re < 5,000, B = 3 mm, D = 2.5 mm)

Nada [103] investigated cooling of the circular cylinder using air IJ. Two configurations of the slot nozzle were investigated: (1) a simple single slot nozzle aligned with the cylinder axis, (2) multiple (three-) slot nozzles orthogonal to the cylinder axis. The Reynolds number is between 1,000 and 10,000. The dimensionless slot width was B/D = 0.125-0.5, the dimensionless nozzle-to-cylinder distance was H/B = 1-12. In general, the three-slot configuration yielded higher Nu than the simple one. The nozzle-to-cylinder spacing was also investigated. The maximum Nu was found for H/B between 4 and 6 for all Reynolds numbers tested, i.e., when the cylinder is placed at the tip of the potential core. Thus, the resulting correlation equation is characterized by

$$Nu = 1.781\left(\frac{B}{D}\right)^{0.147} Re_D^{0.4}\left[1 + 0.147\left(\frac{H}{B}\right) - 0.0256\left(\frac{H}{B}\right)^2 + 0.0012\left(\frac{H}{B}\right)^3\right] \tag{16}$$

(Re = 1,000-10,000, B/D = 0.125-0.5, H/B = 1-12)

Sparrow and Alhomoud [104] focused on the influence of an offset of the slot air jet on a heat transfer from the circular cylinder. The following parameters were tested: D = 304.8 mm, Re_D = 5,000-60,000, H/D = 3.25-7.25, B/D = 0.25 and 0.5, E/B = 0, 0.5 and 1 (E is the offset, i.e., the distance between the jet axis and the cylinder axis). The Nusselt number (the Sherwood number) increases with the slot width and the Re but the Nusselt number decreases with the

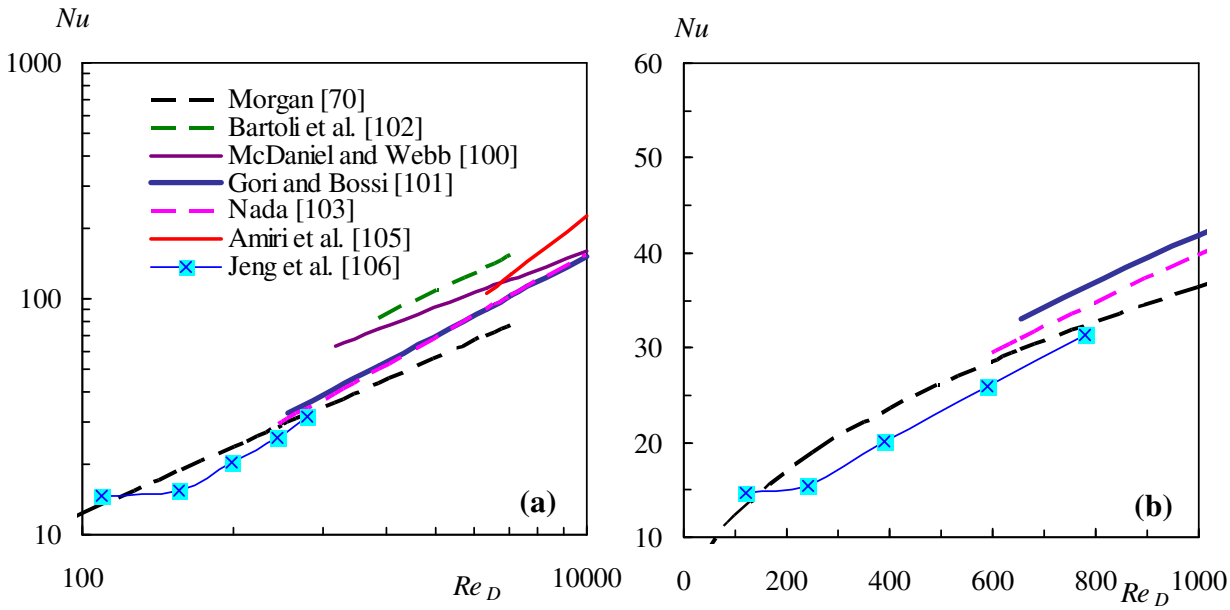

Fig. 1.7 Nusselt number correlations and experimental points by Jeng et al. [106] for the cylinder under the CJ impingement and the correlation by Morgan [70] for the cylinder in the cross-flow;
(a) Complete plot,
(b) Detail view on the region of low Re_D.

nozzle-to-cylinder distance and offset. For the largest offset the heat transfer coefficient was reduced by up to 50%.

Amiri at al. [105] investigated a mixed and forced convection for IJs on circular cylinders in the air at $D = 22$ mm, $B/D = 0.23$, $H/B = 2–8$, and $Re_D = 120–1{,}210$. The local and average Nusselt numbers were evaluated experimentally and numerically. It was confirmed that the average Nusselt number increases with an increase in the Reynolds number and slightly decreases with an increase in the nozzle-to-cylinder spacing. Moreover, the average Nusselt numbers for a forced convective heat transfer regime are commensurate with the case of cylinders in an infinite uniform cross-flow (cf. Morgan [70]).

Jeng et al. [106] investigated the heat transfer characteristics of stationary and rotating cylinders in slot IJs in air at $D = 40$ mm, $B/D = 0.0625–0.50$, $H/B = 1–16$, and $Re_D = 655$-$60{,}237$. Under stationary cylinders, the average Nusselt numbers were slightly greater than the ones for the cylinders in an infinite uniform cross-flow. The influence of the B/D ratio on the position H/B where the maximum of the Nu occurs was shown. As the B/D decreases, the maximum shifts from app. $H/B = 2$ (for $B/D = 0.5$) to more than 8 (for $B/D = 0.0625$). This phenomenon is more dominant for the higher Re_D. No maximum was apparent in lower Re_D. The authors propose a correlation equation characterized by

$$Nu = 0.995\,\mathrm{Re}_D^{0.560}\left(\frac{H}{B}\right)^{-0.341}\left(\frac{B}{D}\right)^{0.768(H/B)^{-0.616}} \tag{17}$$

(Re = 655-60,237, B/D = 0.0625–0.50, H/B = 1–16).

The correlations of the Nu-Re_D relationship are shown in graphical form in Fig. 1.7. The figure also shows the correlation by Morgan [70] for a cylinder in the cross-flow.

1.2.3.4 SJ impingement heat transfer

The impinging SJs and heat transfer from a flat surface (plate) to the SJ were investigated in many studies. Surprisingly, there is (to the best of author's knowledge) no study dealing with heat transfer from a cylinder using SJ, even though the advantage of the SJ as a tool for an impingement heat transfer was already shown. Following this fact, the topic was briefly tested. Based on promising preliminary results, the method and device were patented as an invention ([107]). In the following text, a systematic experimental approach towards this topic is described.

Trávníček and Tesař [50] investigated an annular SJ impinging onto a wall. They used a mass transfer naphthalene sublimation technique. Several regimes of the flow field were found.

Kercher et al. [51] focused on using micro SJ as a tool for thermal management of microelectronic devices. The SJ cooling performance turned out to be comparable with the "classical" cooling fans.

Mahalingam et al. [52] investigated an SJ-based ejector and its utility for electronic cooling in a rectangular channel. The Nusselt number for an SJ ejector flow turned out to be six to eight times higher than a comparable conventional turbulent flow.

Gillespie et al. [53] investigated a plane SJ impinging onto a flat surface. The optimal dimensionless nozzle-to-plate spacing H/B was between 14 and 18, where the maximal average Nu can be achieved.

Arik [54] performed a heat transfer experiment using meso-scale SJ meant for thermal management of electronics. The experiment with SJ impingement onto the flat plate had a heat transfer coefficient enhancement from 4.5 to 10 over the natural convection regime (dependent on heated plate size).

Valiorge et al. [55] found that heat transfer from a flat surface in the stagnation point, using impinging SJ, is strongly influenced by the SJ stroke length (the distance which is traveled by

the extruded vortex ring pair during one period) related to the nozzle-to-plate distance, L_0/H. For the fixed nozzle-to-plate spacing, two flow and related heat transfer regimes were found. First, the increasing L_0/H the ratio Nu/Re^n ($n = 0.32$) increases until $L_0/H = 2.5$. Then, the saturation is reached and the heat transfer becomes constant.

Chaudhari et al. [56] performed an experimental study and the dimensional analysis of heat transfer from a heated plate using SJ. The SJ cooling performance was comparable with the continuous jet given similar conditions.

Persoons et al. [57] proposed general correlation for the stagnation point of heat transfer that were based on the experimental results using SJ for a wide parameter range (e.g., Reynolds number, nozzle-to-surface spacing and stroke length) and identified 4 regimes related to the stroke length of the SJ.

Trávníček and Vít [108] performed a heat transfer study that compared synthetic jets, hybrid synthetic jets, mixed pulsed jets and continuous jets. The enhancement of heat transfer using pulsating jets was shown. The advanced variant of the SJ, the hybrid SJ, led to an 18% enhancement over the classical SJ.

1.3 Aims of the dissertation

Based on the literature review the following aims of the dissertation were specified. The existing device, which was previously only preliminarily tested from the heat transfer point-of-view, will be modified and used for an experimental research. The aims of this dissertation is to experimentally solve the following three problems:

(1) Describe the behavior of synthetic jet (SJ) from the fluid mechanics point-of-view. Namely, to describe the behavior of a submerged SJ originating from a rectangular slot with small slot width (and associated Reynolds numbers), i.e., a (micro) SJ with a slot width below 1 mm.

(2) Describe the behavior of an SJ impinging onto a horizontal cylinder from the fluid mechanics and heat transfer point-of-view. Comparison of SJs and continuous jets (CJs) based on a hypothesis of their similarity.

(3) Quantify the overall convective heat transfer rates in terms of the average Nusselt and Reynolds numbers, i.e., propose a correlation equation.

More specifically, the three aims will be solved through the following particular tasks:

(1) The SJ will be investigated using water as the working fluid. The submerged SJ will be generated by a piezo-electrically driven actuator. The following experimental methods will be used: flow visualization (LIF, Laser Induced Fluorescence), flow velocity measurement (PIV, Particle Image Velocimetry), surface velocity measurement (LDV, Laser Doppler Vibrometry), temperature point measurements (thermocouples and Pt100 probes).

The experiments will consist of an adequate preparation (including a state-of-the-art study of problems and methods), data acquisition, data processing, and result analysis including a comparison with available literature.

(2) A choice of operating parameters of the piezo-electrically driven SJs depends on the actuator's resonant behavior. Therefore, adjustments of the frequency and amplitude of the fluid oscillations are coupled with and related to a particular transducer

(3) Heat transfer experiments will include an overall convective heat transfer measurement based on the Joule effect (the heat generated by the electric current flowing through a conductor). A validation should be based on representative references, therefore the natural convection from cylinders will be used. New correlation equations for the average Nusselt number will be proposed.

2. Experimental setup

The experimental device used in the experiment is shown in Fig. 2.1 (including the coordinate system). The used device was previously patented [107] and preliminarily studied from the heat transfer point-of-view. The actuator body is made up of PMMA (polymethyl methacrylate). It is equipped with a piezoelectric diaphragm (1) (KPS-l00 piezoceramic transducer). The diaphragm consists of a central piezoceramic part (25 mm in diameter and total thickness of 0.22 mm) bonded to a brass part (0.11 mm thick). The diameter of the flexible metal diaphragm, rounded with a plastic rim, is $D_D = 39.5$ mm. The electrical

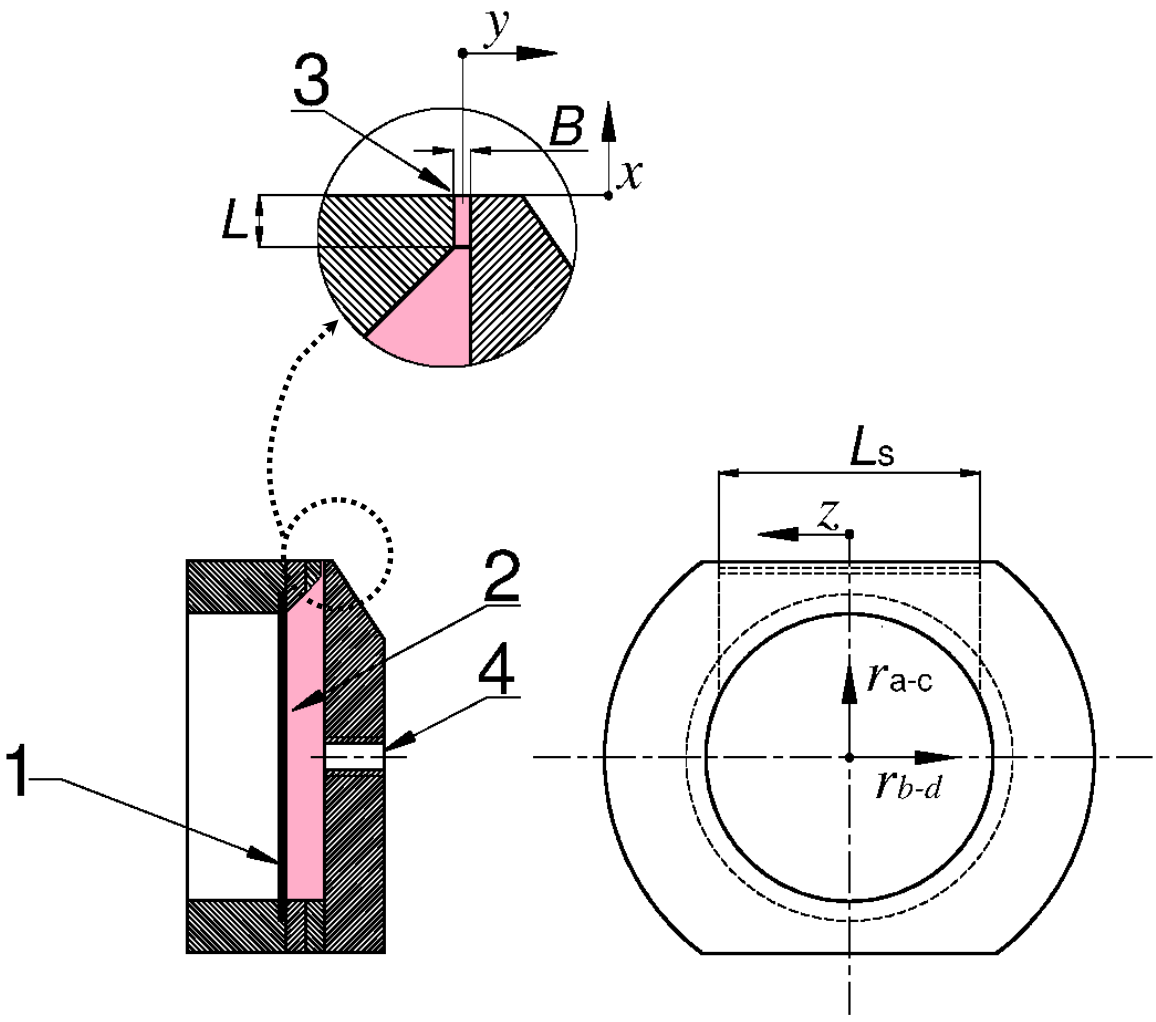

Fig. 2.1 Schematic view of the experimental device;
1: piezoelectric diaphragm, 2: cavity, 3: nozzle, 4: water pump inlet.

insulation of the whole transducer against water surroundings was made via an insulating varnish, which is common in electronics. The actuator body and the diaphragm create a cavity (2) with a diameter and depth of 44 mm and 6 mm, respectively. The jet flow is ejected from a slot (3) on the top of the cavity. The slot width and length are B = 0.36 mm and L_s = 40 mm, respectively. Thus, the aspect ratio of the slot is AR = L_s/B = 111. The length of the nozzle exit channel is L = 1.0 mm.

The actuator can operate in two regimes: it can produce either a continuous jet (CJ) or a synthetic jet (SJ). When the device is operated in the CJ regime, the fluid is fed into the cavity of the actuator using a centrifugal pump (Atman AT-301). The pump is connected to the actuator via a flexible pipe and the fluid enters the cavity opposite to the center of the piezoelectric diaphragm (4). The pump is placed either in the same tank as the actuator or in a separate tank. The former arrangement is used for PIV experiments, the latter for LIF visualization and for evaluation of the time-mean volume flux by means of the gravimetric method (via precise scales). Under the CJ regime, the piezoceramics transducer is not fed.

When the device operates as an SJ actuator, the inlet from the pump is sealed and the piezoceramics diaphragm is driven by the sinusoidal current from a sweep/function generator (Agilent 33210A), which is amplified by an amplifier (RH Sound ST2250BC). The true root-mean-square (RMS) of the alternating current, voltage, and power are measured with an accuracy of ±0.5 %, ±0 5 %, and ±1 %, respectively, using a digital multimeter constructed in-house and operating with 13 kHz sampling frequency.

The setup used for the work with the SJ actuator during the PIV measurement of the flow-field without the cylinder is slightly different: the sinusoidal signal is generated by the function generator (Wavetek model 395) which is amplified by the amplifier (Krohn-Hite model 7602M). The true root-mean-square (RMS) of the alternating current is measured with an accuracy of ±0.1 % rdg ±0.04 % FS by the multimeter HP 34401A and voltage is measured

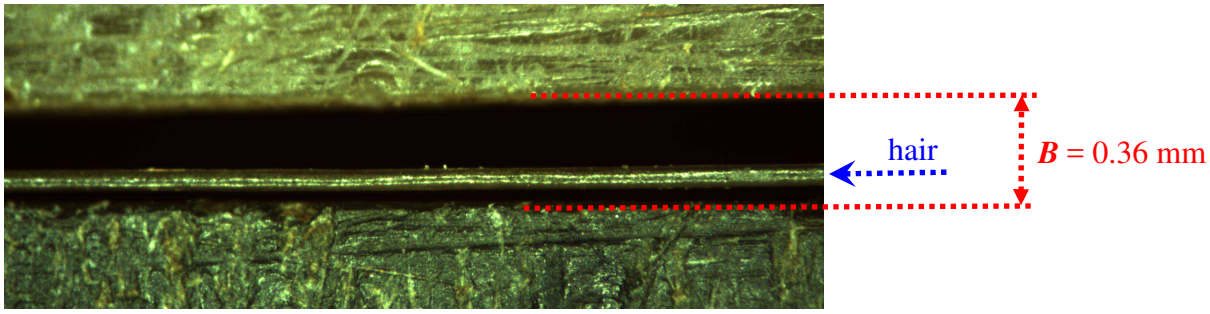

Fig. 2.2 Detail photograph of the nozzle and the comparison of with human hair (diameter of about 0.05 mm).

using the True RMS bench multimeter (Sigmotek CD-3, 4 3/4 digit, with accuracy about 1 % rdg).

To demonstrate the micro-size of the present nozzle, a detailed photograph of the nozzle and a human hair (diameter of about 0.05 mm) was made and shown in Fig. 2.2.

Figure 2.3 shows an overall scheme of the experimental setup, including the cylinder downstream from the nozzle, which was designed for heat transfer measurements. The cylinder (1) is made up of a smooth stainless steel tube; its outside and inside diameters are D = 1.21 mm and 0.91 mm, respectively. The cylinder is mounted parallel to the actuator slot. It

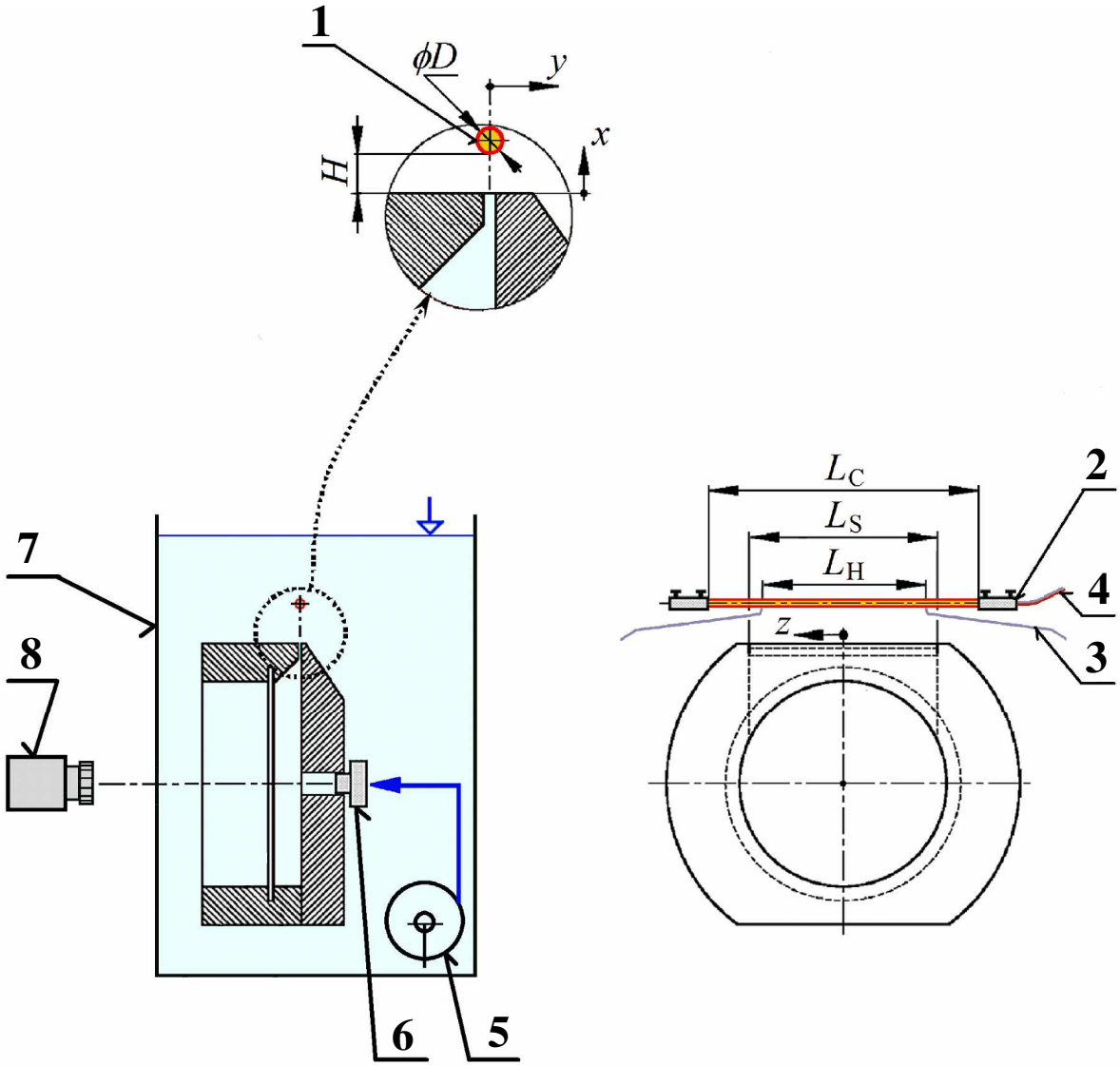

Fig. 2.3 The overall scheme of the experiment;
1: cylinder, 2: cylinder brackets, 3: stainless steel wires (measurement of voltage difference), 4: thermocouple, 5: centrifugal pump, 6: plug, 7: glass tank, 8: vibrometer (LDV).

is fastened into place by two metal brackets (2). The total cylinder length is the distance between the brackets, L_C = 57.5 mm.

For heat transfer experiments, the cylinder is heated via the Joule effect of direct current I_c from the brackets. The test section is in the middle part of the cylinder, which is defined by contact points with a span of L_H = 35.3 mm. In these contact points the stainless steel wires with diameter 0.20 mm (3) are welded and the voltage difference V_c is measured between them. The cylinder end-parts, from the test section, operate as end-guard sections. This arrangement minimizes axial conduction-based heat losses from the test section.

The laboratory power supply, Diametral V140R50D, is used. The current is measured using the Metex M-3800 multimeter with an accuracy of ± (1% rdg + 3 dgt) and a voltage difference in the test section is measured using the multimeter Metex M-4660M with an accuracy of ± (0.8% rdg + 10 dgt).

Most of the SJ experiments were made with a drive frequency of f = 46 Hz. This careful frequency choice was derived from an effort to operate in near-resonance conditions, as will be described in Chapter 5.2. A typical RMS voltage was V_{SJ} = 18.0 V. For this supply, the electrical power was approximately P_{SJ} = 17 mW. Note that the capacitive nature of the piezoceramic transducer did not allow the electrical power to be evaluated as the product of RMS values of the alternating current and voltage because the phase angle θ between them was not negligible in this case, hence it was evaluated from 23° to 28°. Thus, $P_{SJ} = I_{SJ}\ V_{SJ} \cos(\theta)$, where I_{SJ} is the electrical current.

3. Experimental methods and uncertainties

3.1 Laser induced fluorescence (LIF)

The LIF method in liquids is usually used for determination of temperature or concentration fields in water. The method is also considered as a useful tool in the qualitative visualization of flow and temperature fields. As the term implies, the LIF method is based on the fluorescence effect. Fluorescence is a type of photoluminescence, i.e., the transformation of part of the radiant energy, that was absorbed by a material during exposure with electromagnetic radiation, into new radiation with a different wavelength. If the duration of the transformation is long-lasting (from 10^{-2} s to several hours, days or even months), then the effect is called phosphorescence. If the duration of the transformation is short-lived (e.g., an order of magnitude 10^{-8} s), then the excited radiation fades down in almost an instant; this effect is called fluorescence [109,110].

The intensity of fluorescence can be characterized by (see [69,111])

$$I = I_e c \phi \varepsilon \frac{\lambda_e}{\lambda_f}, \tag{18}$$

where I_e is the intensity of light, used for the absorbed (excited) radiation, c is the concentration of the fluorescence dye, ε is the molar absorptivity, ϕ is the quantum yield (the ratio of photons absorbed to photons emitted via fluorescence) and the ratio λ_e/λ_f is the ratio of wavelengths of the absorbed (excited) and emitted (fluorescence) light. Only a part of the energy of absorbed light is reemitted, while the rest is transformed into another type of energy, e.g., heat. According to Stokes' law of fluorescence (also called as Stokes shift), the wavelength of the emitted light is always greater than that of the absorbed one – see e.g., [109,110], i.e., the ratio is $\lambda_e/\lambda_f < 1$.

When the concentration fields are studied, the dependence of the intensity of emitted light on the concentration c is employed at a given temperature (see Eq. (18)). The suitable dye is e.g., Rhodamine 6G.

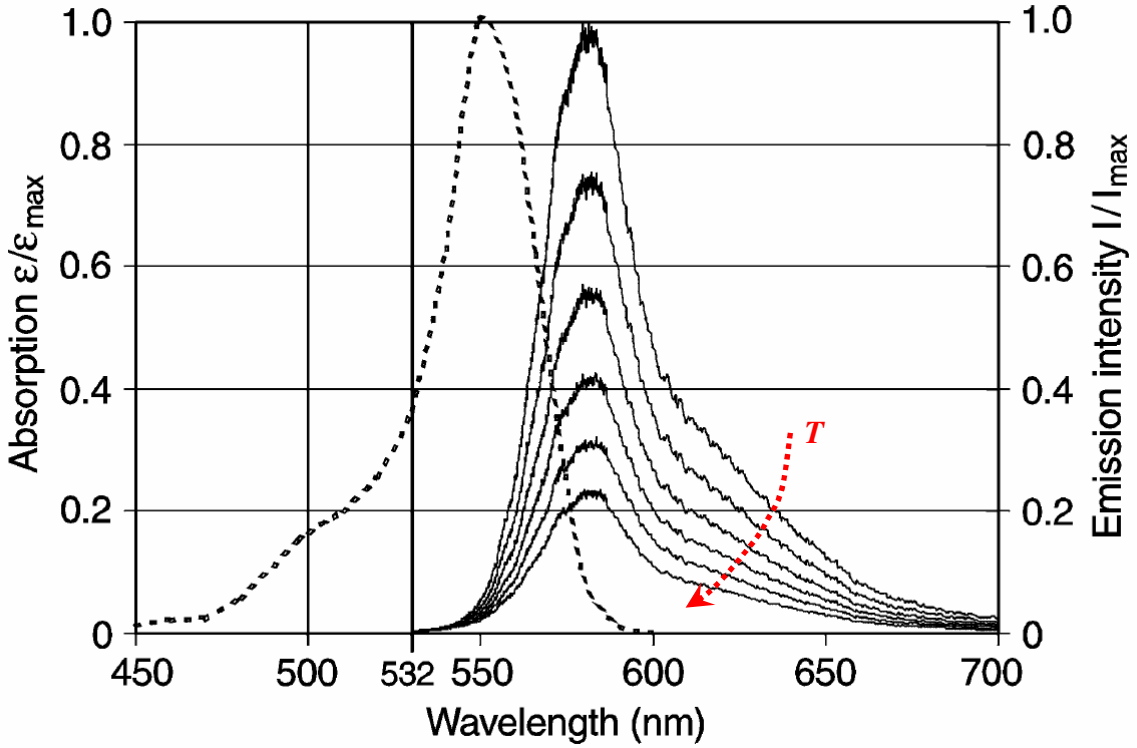

Fig. 3.1 Absorption and emission spectra of Rhodamine B for 20, 30, 40, 50, 60 and 70ºC (adapted from Coolen et al. [114] and modified).

In addition to the dependence on the concentration, the intensity of emitted light of some fluorescent dyes is also influenced by temperature. The higher the temperature is, the lower the quantum yield is. This phenomenon is used when the temperature field of liquids is studied. Suitable dyes are e.g., Rhodamine B (also Rhodamine 610). ([112,113]).

In the present study, the LIF technique was used for visualization of the flow field. Rhodamine B was chosen as the fluorescent dye (chemical formula $C_{28}H_{31}N_2O_3Cl$).

Note that the present system was also used for measurement of temperature fields, but under parameters that were beyond the scope of this study, namely for the investigation of natural convection from horizontal heated cylinders [79,80].

Fig. 3.1 demonstrates the normalized absorption and emission spectra of the dye (the picture is adopted from [114]). The longest absorption wavelength is around 550 nm. The emission spectra of the dye are temperature-sensitive. The higher the temperature, the lower the intensity of the emitted light. The decrease in intensity is reported to be in the range 0.8 – 5% per 1°C ([112,113]). All the emission spectra have a maximum at the same wavelength, which is approximately 580 nm in this case.

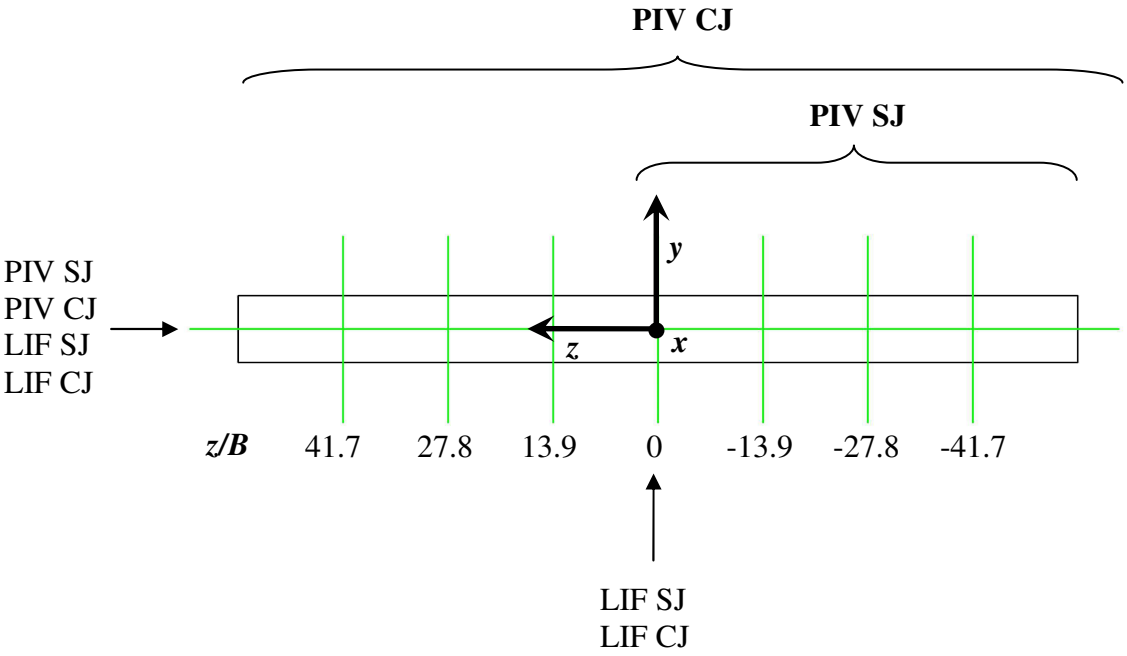

Fig. 3.2 Schematic view on the exit slot (from the top) with planes where the LIF visualization and PIV measurement were performed.

The experiments were made in a glass water tank that had dimensions: height × length × depth = 150 × 245 × 140 mm and that was filled with pure water (either demineralized water, prepared in four-stage reverse osmosis water purification system or distilled).

When the SJA is operated in the CJ regime, the pump is placed in a separate tank. The separate tank is then filled with dye solution (highly concentrated Rhodamine B solution). Subsequently, the pump is turned on. When the SJA is operated in the SJ regime, the cavity of switched-off actuator is filled with the dye solution (a highly-concentrated solution of Rhodamine B, approximately 100 ppm). Consequently, the actuator is placed into the tank filled with water and it is switched on. In both cases (CJ and SJ), the dye-stained flow is lit by a laser sheet (Nd:YAG pulsed laser, Litron, NANO S 65-15), with a wavelength of 532 nm and an output of 65 mJ that is equipped with cylindrical optics. The laser sheet is perpendicular to the slot, i.e., in the *x*–*y* or *x*-*z* plane (along the slot), see Fig. 3.2). The thickness of the laser sheet was approximately 1 mm in the test section.

The pictures of the visible flow field pattern (streaklines) are taken using a high resolution digital camera (HiSense Neo, 2560 × 2160 pixels, 16 bit). The camera is equipped with a Tokina 100 mm F2.8 Macro D lens. To remove the laser light from the pictures, a color filter (cut-off wavelength 570 nm) is used. The camera is used to trigger the laser pulse. The measurement system is controlled via DynamicStudio v3.40 Software (Dantec Dynamics).

3.2 Particle image velocimetry (PIV)

Particle image velocimetry (PIV) is a non-intrusive measurement technique that (in its basic form) allows the evaluation of the whole 2D velocity vector field. The ability of the whole field measurement makes from PIV the unique technique with a wide range of possible uses in contrast to another often used non-intrusive optical method such as Laser Doppler Anemometry (LDA) which facilitates a single-point measurement.

A scheme of a typical PIV experiment is shown in Fig. 3.3. The tracer particles are fed into the flow and the plane is illuminated using a laser sheet. The light is emitted in two consecutive short pulses. The duration of the pulse can be in order of 10^{-9} s and the time between pulses Δt can be in order of 10^{-3} s. The flow with illuminated particles is captured in two consequent pictures of the flow field at time t and $t´$ (schematically depicted in Fig. 3.3). From the subsequent pictures, the spatial shift $s(m,n)$ of the particle can be identified and if the time shift Δt is known, then the velocity vector can be easily evaluated. Obviously, this approach is not possible to apply on huge number of individual particles present in the flow field, digital image processing methods were developed. The sequential images are subsampled into smaller regions, which are usually called interrogation areas (IA) or interrogation windows. In every IA, the average spatial shift is evaluated using a cross-

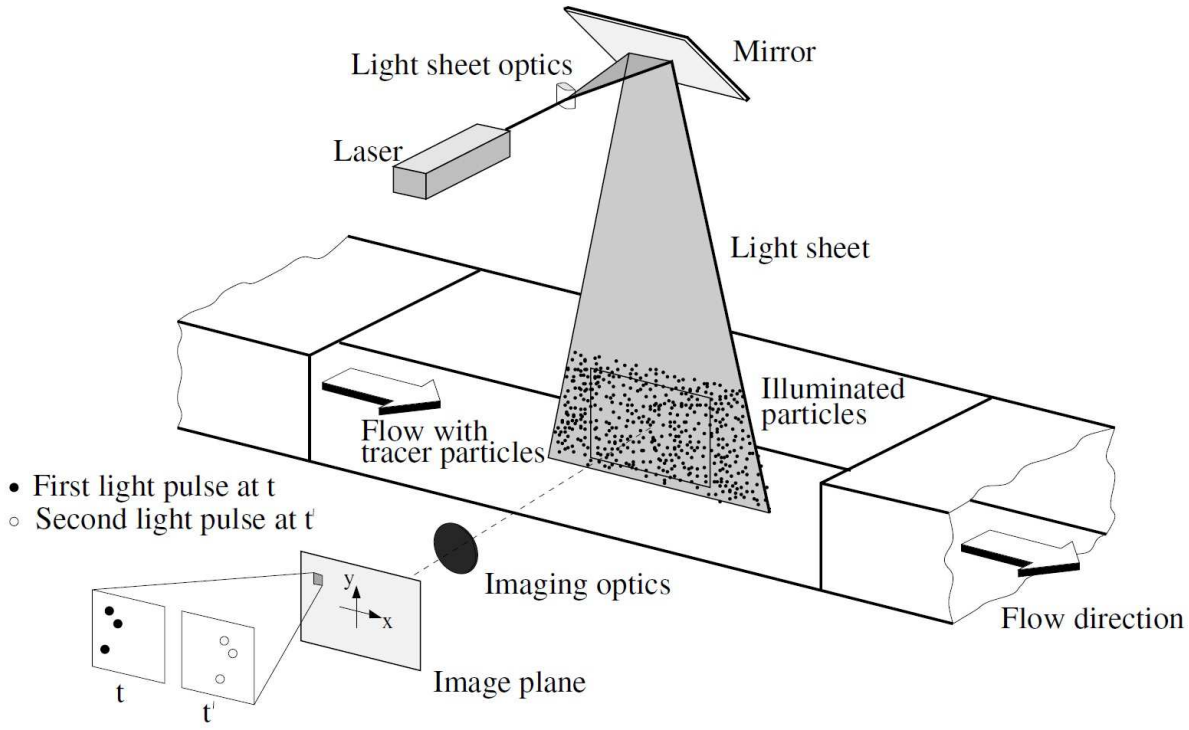

Fig. 3.3 Scheme of the PIV measurement technique (adapted from Raffel et al. [115]).

correlation technique. The computation itself is usually performed via an FFT technique (Fast Fourier Transform). The discrete cross-correlation function of the sampled regions $f(k,l)$ (i.e., IA in time t) and $g(k,l)$ (i.e., IA in time $t^{\prime}$) is expressed by (see [116])

$$\phi_{fg}(m,n) = \frac{\sum_{k=-\infty}^{\infty}\sum_{l=-\infty}^{\infty} f(k,l)g(k+m,l+n)}{\sum_{k=-\infty}^{\infty}\sum_{l=-\infty}^{\infty} f(k,l)\sum_{k=-\infty}^{\infty}\sum_{l=-\infty}^{\infty} g(k,l)}\ , \tag{19}$$

where $f(k, l)$ and $g(k, l)$ are the light intensities at the pixel at position (k, l) of the images at time t and t', respectively.

After the FFT, and the calculation of the cross-correlation function, the inverse FFT is performed to determine the cross-correlation function. In the resulting cross-correlation function, the dominant peak (maximum of the function) can be identified. The line connecting the dominant peak with the midpoint of the correlation plane is the desired vector of mean shift for the IA particles. The precise position of the peak is evaluated with sub-pixel accuracy using a centroiding technique. The peak is commonly interpolated using a Gaussian function (see Willert and Gharib [116], Raffel et al. [115], Kopecký [117]). After detection of the peak, the data are converted into velocity data. This procedure is performed for every IA and a resulting velocity-vector map is obtained. This procedure is a general approach to process the PIV image data. Obviously, various improvements and modifications of the basic procedure exist, including auto-correlation, adaptive correlation, and the application of filter functions, etc. A more detailed description and review of the available techniques is far beyond the scope of the present study, for more information see, e.g., the monograph by Raffel et al. [115]. A more detailed description of the PIV measurements, and subsequent post-processing, used in this study will be provide next.

PIV experiments of the flow-field, without a cylinder, were done in the National Taiwan University, Institute of Applied Mechanics laboratory. The preliminary results were described and provided previously by Broučková et al. [118,119]

The experiments were performed in a cubic glass water tank setting with the side length of 390 mm. The PIV system (using Dantec Dynamics, FlowMap1500) was used with polyamide seeding particles (PSP-5, Dantec Dynamics, 5μm in diameter). The light source was a

Nd:YAG dual laser head system (NewWave, 120 mJ at 532 nm) with a cylindrical lens. The thickness of the laser sheet was approximately 1 mm (in the test section). The image pairs were acquired using a CCD camera (Kodak, MegaPlus ES1.0) with a spatial resolution of 1008 × 1016 pixels. The camera was equipped with a Micro-Nikkor 55 lens. The typical time delay between pulses was in the range 700 to 3000 μs.

The pictures were taken using Flow Manager software (Dantec Dynamics). The subsequent post-processing was done using DynamicStudio v3.40 Software (Dantec Dynamics).

The velocity vectors were calculated using an advanced cross-correlation technique, namely the DynamicStudio built-in Adaptive PIV technique. This method iteratively adjusts the size and shape of the individual IA to adapt local seeding densities and gradients (for more details, see [113]). The minimum size of the IA was 32 × 32 pixels and the maximum size was 64 × 64 pixels, with a grid step size of 16 × 16 pixels with 50% overlap and a moving average area filtered via a 3 × 3-pixel window. Velocity and vorticity maps were averaged from a sequence of approximately 100 images.

The experiments were performed as the phase-locked measurement, after the periodic nature of the SJ. To synchronize the PIV system with the driven signal, the trigger signal was taken from the function generator that was feeding the SJA. The frequency of this trigger signal was divided, by the 74HC112N chip, to be half the driven frequency (i.e., $f/2 = 23$ Hz). The reason is the frequency limit of the PIV system, which is only 30 Hz. To catch the phase-locked data, the digital delay generator (Stanford Research System DG535) was used. The trigger signal can be delayed to an arbitrary phase. The delayed phase-locked signal was then used to trigger the PIV system. When the CJ was investigated, a synchronization was not performed and the experiments were controlled solely via the Flow Manager software without an external trigger.

Investigations of the flow-field, within the cylinder were performed using the PIV system in Prague, at IT CAS. The experiments were performed with the same setup described in the LIF visualization. In this case, a Litron NANO 145-15 PIV laser was used. The fluorescence particles PS-FluoRed-FRAK-Fi204 were 1-20μm in diameter. The images were post-processed via DynamicStudio v5.1 software (Dantec Dynamics). The procedure and the software setup was same as the previous test.

The visualization using LIF and PIV measurements were performed on several planes. The schematic illustration of the individual laser sheet positions is shown in Fig. 3.2.

Note that the PIV method provides a 2D velocity map, i.e., the resulting velocity magnitude is always a combination of only two velocity components. To distinguish the components of the particular velocity magnitude, the following nomenclature is introduced:

The velocity magnitude in *x*-y plane is characterized by

$$U_{x-y} = \sqrt{U^2 + V^2} \ . \tag{20}$$

The velocity magnitude in *x*-*z* plane is characterized by

$$U_{x-z} = \sqrt{U^2 + W^2} \ . \tag{21}$$

3.2.1 Uncertainties of the PIV method

The evaluation of the PIV measurement uncertainty is a complex problem where many properties of the measurement chain need to be determined.

The list of possible sources of the systematic errors found in PIV measurements are described e.g., by Kopecký [117]:

- loss pairs - during the time interval between two consequent flow field images in time *t* and *t´*, i.e., when the particle left the IA or when a new particle enters the IA.
- maximal particle shift between time *t* and *t´* is recommended to be 1/4 the length of IA (the recommendation is based on the Nyquist criterion)
- the sufficient particle density in the IA, the recommendation is at least 5 particles for the cross-correlation
- the dynamic range, i.e., the maximal and the minimal measurable velocity (given by the size of the particle, size of the IA etc.)

Many of the possible systematic errors can be removed by following the basic rules (e.g., the maximal particle shift) or by using the advanced correlation methods (e.g., adaptive correlation).

Timmins et al. [120] proposed a method of estimation for the instantaneous uncertainty of the PIV measurement. The source of errors for the following parameters were considered: particle

diameter, particle density, particle displacement and velocity gradient. Lost pair effects are not involved in this evaluation process.

Gordon et al. [121] combine three sources of random errors to obtain the total random error for PIV measurements: the error of the particle displacement (uncertainty in the location of the cross-correlation peak); the error due to magnification uncertainty (spatial resolution of the images); and the uncertainty of separation time between laser pulses.

The topic of the PIV measurement uncertainty was deeply analyzed at the 25th ITTC conference, see the Guideline [122]. Six main groups of error sources are described:

- the calibration (including magnificent factor, image distortion due to aberration of lenses etc.)
- the displacement of particle image (including laser power fluctuation, lens aberration, view angle, mismatching error, sub-pixel analysis etc.)
- the time interval of the experiment (including ability of the particle to follow the flow and out-of-plane velocity)
- the measurement position (including determination of the center position of the correlation area, non-uniformity of tracer particle distribution across the correlation area etc.)
- the measurement time, i.e., the fluctuation of the pulse.

All groups contribute to the total combined uncertainty of the entire measurement chain. The largest source of uncertainty for the case investigated in [122] was found to be the mis-matching uncertainty. The next two largest sources were the sub-pixel analysis and the uncertainty caused by lens aberration.

As is obvious from the above described approaches, the evaluation of PIV measurement uncertainty is a complicated and time-consuming task; moreover, as in [123], the methods are only able to provide an estimation of an expected error for an average measurement under specific image quality and flow conditions. In 2013, two novel approaches to determine the PIV measurement uncertainty were introduced:

1) A method based on image matching (particle disparity approach) - Sciacchitano et al. [123].

2) A method based on cross-correlation peak ratio - Charonko and Vlachos [124].

Instead of input measurement parameters, both methods use the resulting images, as a basis for the evaluation of the uncertainty.

The method by Sciacchitano et al. [123] is based on the statistical evaluation of matched particle image disparity. After the cross-correlation, the resulting mean particle image displacement is obtained. If the window from the second exposure is shifted back to the first exposure, most of particles will partially superimpose each other. Some particles will not superimpose each other for several reasons (e.g., out-of-plane motion, presence of noise in recording, velocity gradient etc.). The residual distance between a pair of particle images after the matching is called a matched particle image disparity. The accuracy of the method depends on the particle's image density. A minimum of six particle images per IA is required for an accurate error estimation.

The Charonko and Vlachos [124] method is based on the ratio of the first and second highest correlation peak, and its empirical relationship to the radial error. Although the highest detectable correlation peak is assumed to be the best estimate of the true displacement, the second highest correlation peak is related to the combined effects of all error sources stemming from the image quality and flow field. Thus, the ratio between the first and second highest correlation peak can provide the displacement estimate uncertainty.

The uncertainty of the PIV measurements in this work are estimated via Sciacchitano et al. [123] and Charonko and Vlachos [124] methods. Both methods are implemented in DynamicStudio v5.1 software (Dantec Dynamics).

The radial uncertainty σ_R is calculated. Radial uncertainty is defined as ([113]):

$$\sigma_R = \sqrt{\sigma_U^2 + \sigma_V^2}\,, \tag{22}$$

where σ_U and σ_V are the standard deviations of the velocity errors in the vertical and horizontal direction, respectively. The radial error follows the Rayleigh distribution, i.e., the result only has a 39% likelihood of occurring. To obtain an expanded uncertainty, i.e., a probability of 95%, the uncertainties should be multiplied by a factor of 2.45.

A typical example of PIV measurement results is shown in Fig. 3.4(a) and (b) (which shows the CJ impinging on the cylinder, the result itself will be described in Chapter 5.3). In Fig. 3.4(a), the instantaneous velocity vector field is colored by the estimated uncertainty according to Sciacchitano [123]. In Fig. 3.4(b), the same vector field is colored by the estimated uncertainty per Charonko and Vlachos [124]. The large white areas show the place where parts of the experimental devices were masked in the raw picture. The individual white

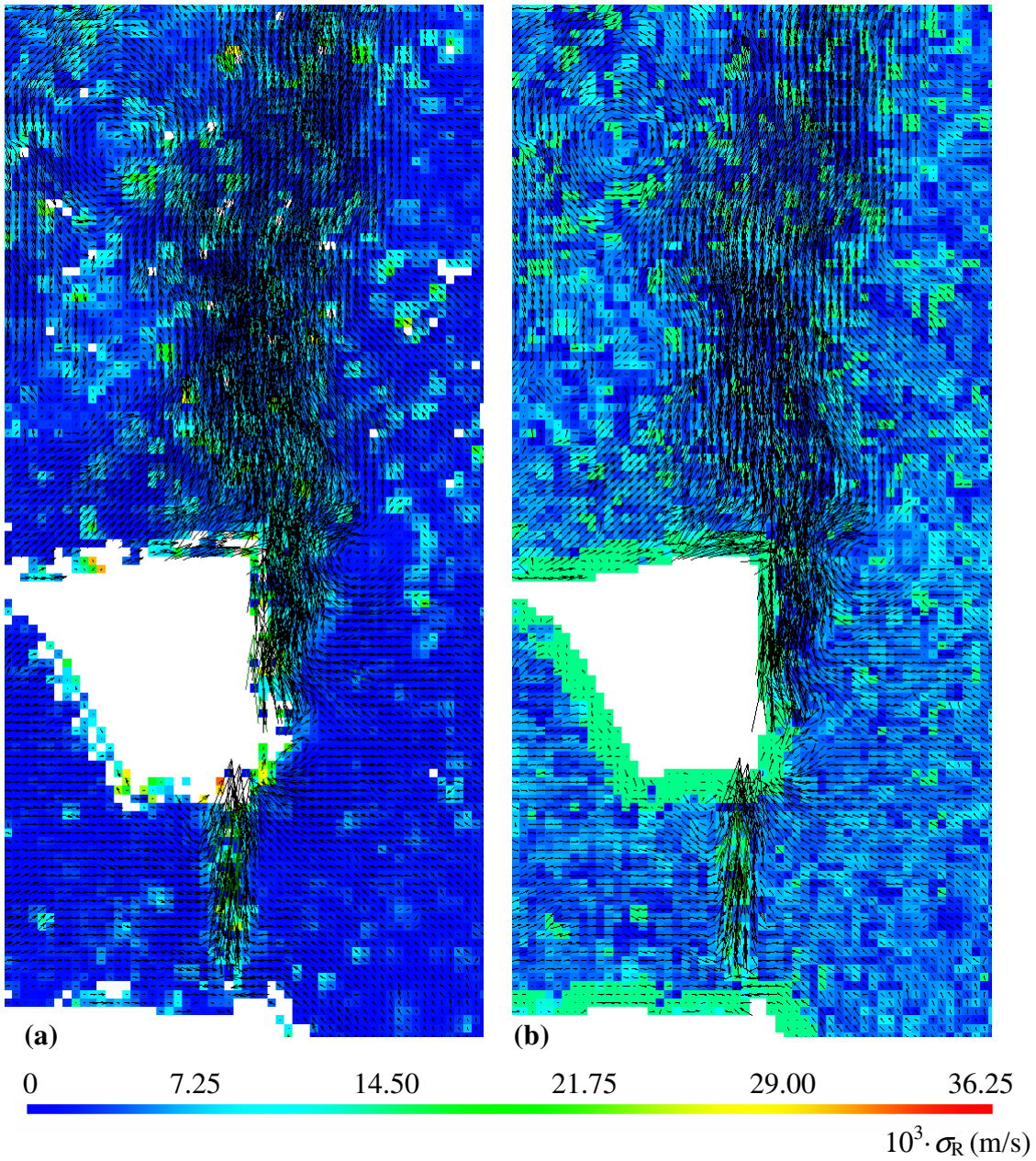

Fig. 3.4 Experimental uncertainty estimated for the present PIV measurement from:
(a) Method based on image matching according to Sciacchitano et al. [123],
(b) Method based on cross-correlation peak ratio according to Charonko and Vlachos [124].

squares are surrounded by colored squares and represent the IA where the displacement vector was not properly calculated (e.g., due to severe out-of-plane motion) and where the uncertainty was not calculated.

Just note here that the displayed computed uncertainty is based on a random error estimation, the systematic error is assumed negligible in modern PIV systems (see [113]).

The image matching technique provides (on average) a lower uncertainty estimation than the other one (in this case), however the typical uncertainty value is within $\sigma_R = 0.01$ m/s in both

methods. The typical velocity value is $U_{x\text{-}y} = 0.1$ m/s with a resulting 10% relative uncertainty. The higher uncertainties are near the experimental devices due to the influence of the reflections. The present uncertainty level is high because of the relatively low measured velocities and the very small dimensions of the experimental device and the jet itself.

A reliability of the PIV experiments depends on a balanced treatment of many problems. Some of them escalate at micro-size and low velocities measurements.

A compromise must be found in this case because the seeding particles must be small enough to accurately follow the flow The response time of the particles should be reasonably short and match an unsteady flow and a flow at high gradient of velocity and small enough for small disturbance of the flow. On the other hand, the particles must be large enough to scatter enough light so the image can be recorded.

In the present task, the diameter of the chosen particles (5 μm and 1-20 μm) is relatively large enough for the geometry, i.e., the particle diameter is only two orders of magnitude lower than the lateral dimension of the slot ($B = 0.36$ mm), i.e., the initial lateral dimension of the jet. This fact can influence the ability of the particles to follow the flow properly. Moreover, the slot width ($B = 0.36$ mm) is only 36% of the laser-sheet thickness.

Another problem results from near-wall effects. While the PIV experiment is a powerful tool in an area without solid boundaries, the presence of walls can contaminate the results and cause undesirable effects. Many reasons of this problem are linked with a flow character in near-wall flow regions (high gradient of velocity in the boundary layer and a lack of particles there). Other reasons are optical, such as the unavoidable reflection and scattering of a laser-light by a wall surface.

Therefore, the reliability of results at the vicinity of the nozzle is smaller than in the far field. Nevertheless, the measurement can still bring valuable qualitative information, particularly about the character of the jet close to its origin. Therefore, the results from the immediate surroundings, of the nozzle exit, will be shown here in some cases as well. In graphs, the unreliable region ($x/B < 15$) will be marked by a grey color.

3.3 Laser Doppler vibrometry (LDV)

Measurement of the oscillating piezoceramics diaphragm velocity was performed. The LDV technique was used.

The measurement of the vibrometer is based on the heterodyne interferometer principle (see [125]). The emitted laser beam is scattered back from the investigated vibrating surface. The scattered laser beam is Doppler-shifted due to the velocity of a vibrating surface. The frequency shift (or Doppler frequency) is given by the following expression

$$f_D(t) = 2\frac{v(t)}{\lambda}, \tag{23}$$

where v is the velocity of the vibrating surface, in the direction of the beam, and λ is the laser wavelength. The emitted and scattered beams are superimposed, and with the aid of the Bragg cell, the electrical signal is generated at the photodetector. The resulting electrical signal has an instantaneous frequency of

$$f_C(t) = f_B + f_D(t), \tag{24}$$

where f_B is the frequency shift due to the Bragg cell. The frequency demodulation is then performed, and the velocity of the investigated surface is obtained (see [125]).

A portable digital vibrometer (Ometron VH-1000-D, B&K 8338) was used in this study. The light source of the vibrometer is a helium neon laser. The frequency range is 0.5 Hz – 22 kHz and the possible velocity ranges (peak-to-peak) are 20 mm/s, 100 mm/s, and 500 mm/s. The resolution is better than 0.02 μm/s/Hz$^{0.5}$ (for the range rates 20 and 100 mm/s) and better than 0.1 μm/s/Hz$^{0.5}$ (for the range 500 mm/s).

The signal from the vibrometer was sent to an NI PCI data-acquisition device (6023E). The typical sampling frequency and number of samples are 10 kHz and 16,384, respectively. The data-acquisition process used two channels and recorded the LDV data and the reference TTL signal from the sweep/function generator. The procedure for data post processing, including phase averaging, was developed in MATLAB.

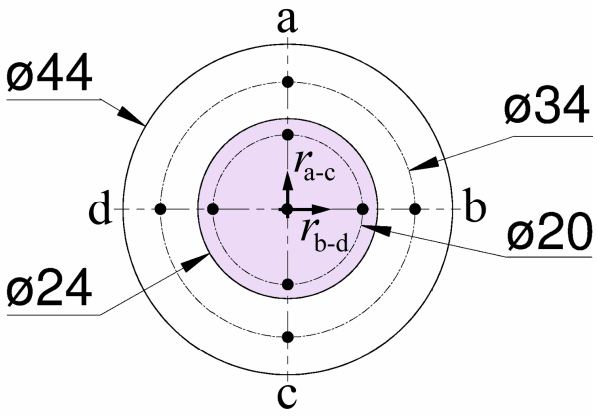

Fig. 3.5 Arrangement of 9 points for LDV velocity measurements of the oscillating diaphragm. The diameters of 24 mm and 44 mm show sizes the piezoceramic transducer and the cavity, respectively.

During the experiments, the SJ actuator was placed in a glass water tank filled with pure water (note the same device and procedure for the LIF experiment was used), then the SJ actuator was switched on. The laser beam was focused on the rear of the piezoceramic diaphragm. The velocity waveforms were investigated in the centre of the diaphragm and in another 8 points at diameters of 20 mm and 34 mm - the positions of the points are shown in Fig. 3.5. Note that the piezoceramic part of the diaphragm has a diameter of 24 mm, i.e., the points on the bigger diameter were placed on the outer brass part of the diaphragm, as indicated by Fig. 3.5.

Assuming harmonic (sinusoidal) oscillations of the diaphragm, the instantaneous position of the diaphragm center during the cycle can be express as

$$y(t) = -y_{\max} \cos(\varphi), \tag{25}$$

where $y_{\max}$ is the amplitude of the diaphragm displacement from its middle position and $\varphi = 2\pi ft$ is the phase angle (defined from the origin $\varphi = 0$ as the beginning of the pump stroke). The diaphragm velocity is then simply a derivation of the position

$$v(t) = \frac{dy}{dt} = 2\pi f y_{\max} \sin(\varphi) = v_{\max} \sin(\varphi) \tag{26}$$

By using LDV, the velocity waveforms at the selected points of the diaphragm were measured, phased-averaged and consequently integrated to obtain the time behavior of the deflected surface during the period. Knowing the deflections of 9 points on the surface, the evolution of the diaphragm shape during one actuation period was determined.

Considering the slug-flow (one-dimensional or "piston-like" flow) model for fluid flow through the SJ slot nozzle, the harmonic motion of the diaphragm results in a harmonic motion of the fluid through the nozzle outlet, so the instantaneous velocity in the nozzle outlet is

$$u_0(t) = U_{\max} \sin(\varphi), \tag{27}$$

where $U_{\max}$ is the maximum SJ velocity at the nozzle outlet. By using the continuity equation for incompressible flow, the maximum flow velocity can be express by

$$U_{\max} = 2c\pi f y_{\max}\left(\frac{A_D}{A_s}\right), \tag{28}$$

where A_D is the diaphragm area ($A_D = \pi D_D^2/4$), A_S is the cross-sectional area of the slot nozzle ($A_S = BL_s$), and c is the parameter that considers the diaphragm shape; in the case of a paraboloid, $c = 0.5$ can be considered as the first iteration.

3.4 Gravimetric method

Due to micro-size and expected low velocity of the CJ, the gravimetric method was used to evaluate the time-mean volume flux of the CJ. The experiment was made using precise laboratory scales (Mettler Toledo PR 8002 Delta Range) with the resolution, repeatability and linearity 0.01 g, 0.01 g, and ±0.02 g, respectively.

The amount of water discharged during the specified time (typically 3–10 min) was weighed and consequently the average volume flux Q, through the nozzle, was evaluated. The time and spatial mean velocity at the nozzle exit U_m was evaluated via the equation

$$U_{\mathrm{m}} = \frac{Q}{L_{\mathrm{s}} B}. \tag{29}$$

3.5 Temperature measurement

The cylinder temperature, T_{w}, was measured using a J type thermocouple and an Omega DP41-B thermometer. The thermocouple was plugged into the cylinder tube. The bulk temperature of water T_{∞} was measured by an NTC thermistor sensor (Ahlborn AMR, Therm 2280-3).

All experiments were made after a thorough stabilization of the temperatures. In this study, the temperature ranged between approximately T_{w} = 20.8–40 °C and T_{∞} = 20.8–26.8°C, depending on the adjusted heating power. Both thermometers with probes had been calibrated, and the maximum uncertainties of T_{w} and T_{∞} were less than ± 0.2°C and ± 0.1°C, respectively.

3.5.1 Uncertainties of the Nusselt number evaluation

An uncertainty analysis was performed, according to the method outlined by Kline and McClintock [126], for a single sample experiment. The overall uncertainty of the *Nu* consists of contributions of each measured variable in Eq. (8). Following the law of uncertainty propagation, the *Nu* uncertainty can be expressed in terms of the standard deviations from the individual contributions [126] via the expression

$$\frac{\sigma_{Nu}}{Nu} = \sqrt{\left(\frac{\sigma_I}{I}\right)^2 + \left(\frac{\sigma_V}{V}\right)^2 + \left(\frac{\sigma_k}{k}\right)^2 + \left(\frac{\sigma_{L_H}}{L_H}\right)^2 + \frac{\sigma_{T_w}{}^2 + \sigma_{T_\infty}{}^2}{\left(T_w - T_\infty\right)^2}}. \tag{30}$$

In the present experiments, at larger heating inputs, Eq. (8) yields the standard deviation σ_{Nu}/Nu for natural and forced convection 1.4% and 2.1 %, respectively. Thus, the resulting expanded uncertainties with a 95 % confidence (i.e., with the coverage factors of K_{j} = 2) are double the values of Eq. (30). Typical input and resultant values are summarized in Table 2 (all natural convection experiments) and Table 3 (typical forced convection experiments with SJ at larger heating values).

Table 2 Nusselt number uncertainty analysis for the natural convection experiments

Variables	Typical values	Coverage factors k_j	Uncertainties
I	1.88–9.78 A	2.576	2 %
V	0.100–0.523 V	2.576	0.05 %
L_H	35.3 mm	2.0	0.3 mm
T_w	23.1–45.0 °C	2.576	0.2 °C
T_∞	21.4–21.9 °C	2.576	0.1 °C
K	0.602–0.609 W/(m·K)	2.0	2 %
Nu	1.7–3.2	2.0	**2.8–10.6 %**

Table 3 Nusselt number uncertainty analysis - typical forced convection experiment (SJ)

Variables	Typical values	Coverage factors k_j	Uncertainties
I	9.79 A	2.576	2 %
V	0.516 V	2.576	0.05 %
L_H	35.3 mm	2.0	0.3 mm
T_w	29.2 °C	2.576	0.2 °C
T_∞	23.6 °C	2.576	0.1 °C
k	0.610 W/(m·K)	2.0	2 %
Nu	13.5	2.0	**4.2 %**

A determining factor in the overall uncertainty is the temperature difference T_w–T_∞. The smaller T_w–T_∞ differences, at lower input heat, imply increasing uncertainties. In the natural convection experiments, the minimum difference T_w–T_∞ was 1.7 °C, thus Eq. (30) yields the standard deviation of 5.3 % (i.e., the uncertainty of 10.6 % at the 95 % confidence level). However, the forced convection increases Nu and decreases T_w–T. When the T_w–T_∞ is below 1 °C, the standard deviations, calculated via Eq. (30), increases to 9%, thus the overall uncertainties based on a 95% confidence level increase to 19%; such experiments are considered as qualitative only and they should be omitted from the data processing. To demonstrate these effects for the present parameters, the experimental data will be complemented by error bars that indicate the uncertainties – see the Nu–P relationships in Fig. 5.43 and the relating text in Chapter 5.4.

4. Relevant parameters

4.1 Continuous jet

In the description of the submerged rectangular jet, with a high aspect ratio, one length scale is important: the width of the exit slot/nozzle B. In the case of a small aspect ratio, the length of the slot L_s also becomes important.

The Reynolds number of the jet is usually based on the width of slot B and the mean velocity at the exit slot U_m:

$$Re_{CJ} = \frac{BU_m}{\nu}. \tag{31}$$

When the obstacle is placed in the flow (cylinder in this case), scaling the Reynolds number with the dimension of the obstacle (the diameter of the cylinder D) is possible via the expression

$$Re_{CJ,D} = \frac{DU_m}{\nu}. \tag{32}$$

4.2 Synthetic jet

Two length scales are necessary to describe an SJ: the size of the exit slot/nozzle (i.e., the width B in the case of slot or rectangular nozzle) and the stroke length. The stroke length L_0 is the length of the column of fluid that is extruded from the cavity during one working period. The length can be determined via the expression

$$L_0 = U_0 T, \tag{33}$$

where $T = 1/f$ is the duration of a single period, f is the jet frequency and U_0 is the time-average velocity at the exit orifice obtained from the extrusion part of the period T_E (modified

from [29]). When the slug flow model is considered, the velocity U_0 can be evaluated from its instantaneous velocity on the jet axis at the nozzle exit, u_0 (see Eq. (27))

$$U_0 = \frac{1}{T}\int_0^{T_E} u_0(t)dt \,. \tag{34}$$

When Eq. 27 is obeyed (i.e., the waveform is purely sinusoidal), the relation $U_{max} = \pi U_0$ is valid. The Reynolds number of the SJ can be defined (similar to Eqs. 31 and 32 for the CJ):

$$Re_{SJ} = \frac{BU_0}{\nu} \tag{35}$$

and

$$Re_{SJ,D} = \frac{DU_0}{\nu}\,. \tag{36}$$

Another parameters that are important for the description of SJ are the Strouhal number

$$St = \frac{\pi B}{L_0} \tag{37}$$

and the Stokes number

$$S = \sqrt{StRe_{SJ}}\,. \tag{38}$$

Note here that the minimal parametric threshold must be obeyed to form the SJ. For more information about the formation criterion of SJ, see Holman et al. [33], Trávníček et al. [36] and Broučková et al. [127]. For the SJ that is issued from the slot orifice, the formation criterion was found by Smith and Swift [128] in the form

$$\frac{L_0}{B} = \frac{4}{\sqrt{\pi}} \doteq 2.26 . \tag{39}$$

4.3 Heat transfer

The governing parameters for the forced convection are the Reynolds and the Prandtl numbers (Eq. 7). For natural convection, the governing parameters are the Grashof (Eq. 5) and the Prandtl numbers (Eq. 7) [66].

5. Results and analysis

5.1 Continuous jet (CJ)

5.1.1 Evaluation of the time-mean exit velocity

Following the approach described previously, the time-mean volume flux of the CJ was evaluated using laboratory scales. The measurement was performed for three volume fluxes. The results are summarized in Table 4.

Table 4 Parameters of the CJ experiments

Q l/min	U m/s	Re
0.090	0.10	40
0.177	0.20	79
0.357	0.41	161

The measurement was performed three times for each case. The values in Table 4 are the average values of all three measurements. The Reynolds number for all three cases are higher than the limit for laminar flow reported by Blevins [3] ($Re_{CJ} = 30$) or by Sato and Sakao [22] ($Re_{CJ} = 33$), thus a turbulent flow can be expected in the present CJ.

The CJ with the lowest Reynolds number ($Re_{CJ} = 40$) was chosen for more detailed investigation.

5.1.2 Continuous jet - flow visualization

The next step in the investigation of the CJ is the qualitative visualization of the flow field. Figure 5.1(a) shows a visualization of the CJ across the slot. The laser sheet was positioned at x-y plane, in the middle of the exit slot ($z = 0$). Similarly, Fig. 5.1(b) represents a visualization of the CJ along the slot, i.e., laser sheet was placed in the x-z plane ($y = 0$), see Fig. 3.2. Both instantaneous pictures reveal that the jet keeps its initial nature for a great distance downstream; the jet only slightly gradually spreads in the lateral direction (Fig. 5.1(a)). On the contrary, only a slight contraction is visible in the spanwise direction (Fig. 5.1(b)). The individual disturbance of the jet shown in Fig. 5.1(b) is probably caused by the interaction

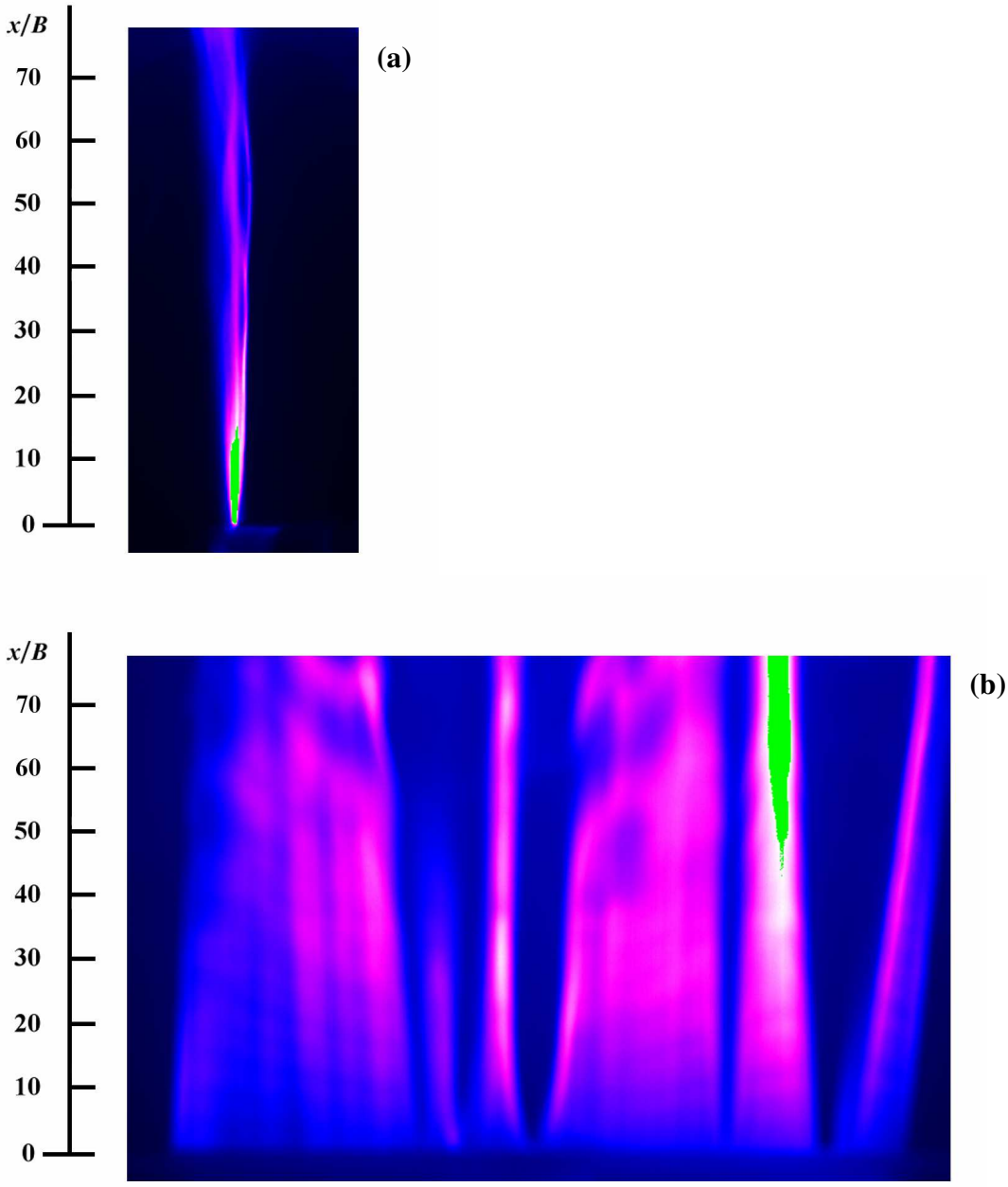

Fig. 5.1 Visualization of the CJ
(a) Across the slot (*x*-*y* plane),
(b) Along the slot (*x*-*z* plane).

with the free-water surface (approximately at $x/B = 100$, not shown in the picture). The jet is smooth, with no visible coherent structures (i.e., vortex formation), breakdown and transition process which are typical for turbulent macro-jets. These observations agree with the micro-jet results by Gau et al. [24] - the dimensionless breakdown length according to Eq. (3) should be very far downstream at $L_b/B = 350$. This is far beyond the present field of view.

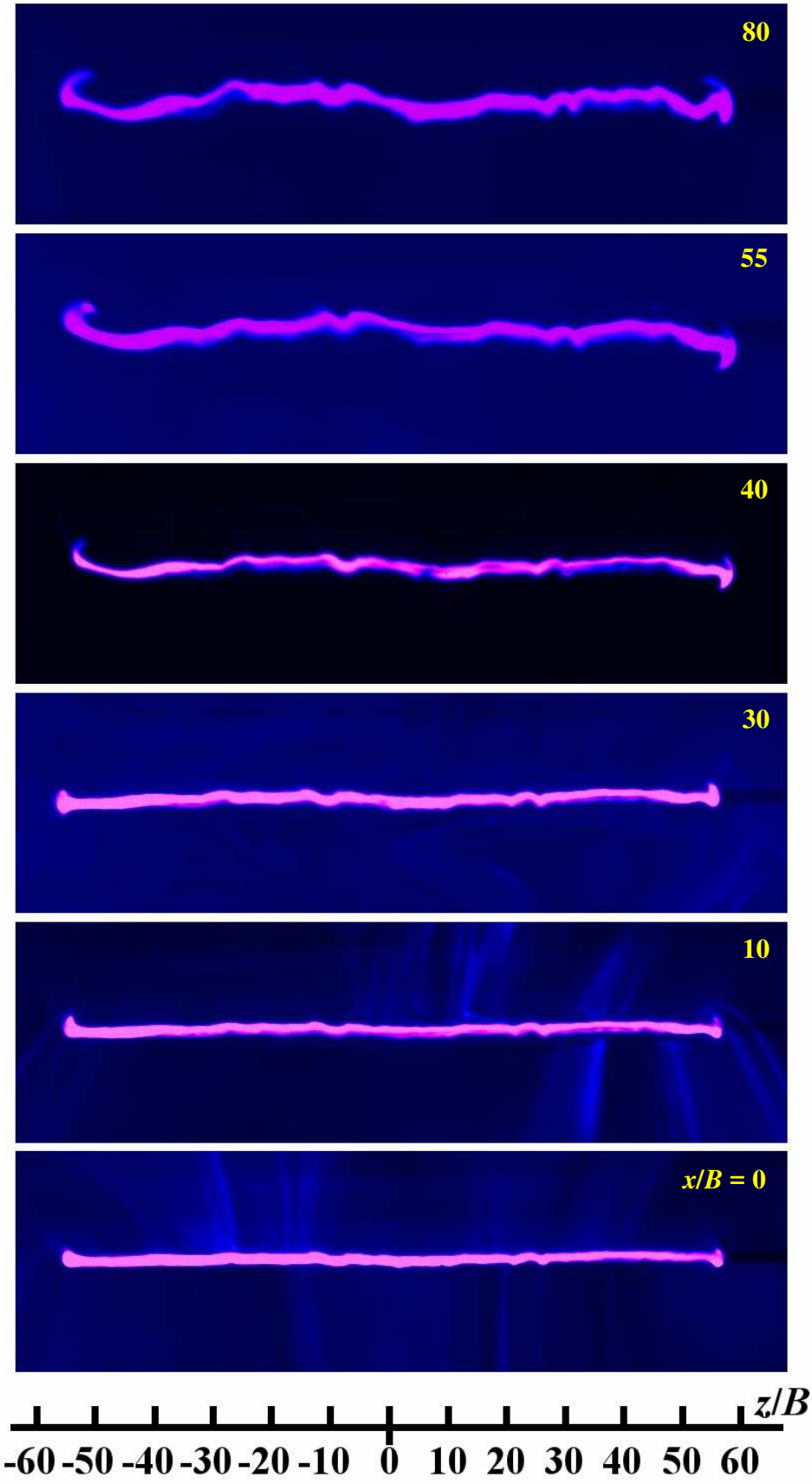

Fig. 5.2 Visualization of the CJ in *y*-*z* planes.

Fig. 5.1(b) also shows that the jet is not fully uniform in the spanwise direction. The flow is "weaker" in the central location (visible as a darker area around the position $z = 0$). The existence of a saddle-back velocity profile is expected.

To obtain a more complex idea about the evolution of the jet in space, the visualization in the y-z plane for several distances from the exit was also performed (Fig. 5.2). In this case the jet was oriented horizontally upwards during the experiments, due to technical reasons. The results confirm the observations from Fig. 5.1(a) and (b). The lateral width of the jet (i.e., in the direction of y-axis) does not change considerably with distance from the exit plane ($x/B = 0$). Moreover, the width of the jet is approximately constant along the span for each distance. The spanwise width does not change as well. The jet keeps its initial rectangular shape up to $x/B = 30$, where a gentle waviness in the lateral direction can be observed. The waviness becomes more dominant further downstream.

Note here that the instantaneous images, shown in Fig. 5.2, captures only one state of the jet for a single moment. When the jet was observed in time, instabilities in the lateral direction at distances away from $x/B \geq 55$ were visible. However, they were rather random and intermittent in character. An occurrence of the instability effects can be considered as an early indication of oncoming transition processes.

Obviously, deeper elucidation of the flow-field is beyond limits of the qualitative visualization – thus the present investigation continues by the PIV measurement in the following text.

5.1.3 Continuous jet - PIV results

For the quantitative examination of the flow field, the PIV method was used. The measurement was performed across the slot for 7 planes parallel to the x-y plane, specifically at z/B = -41.7, -27.8, -13.9, 0, 13.9, 27.8, 41.7 (i.e., z = -15, -10, -5, 0, 5, 10 and 15 mm), and along the slot, i.e., at x-z plane ($y = 0$). The schematic illustration of the individual positions of the laser sheet is shown in Fig. 3.2. All the pictures are the average from approximately 100 individual captures.

The velocity vector field of the flow along the span is shown in Fig. 5.3(a). The vector field is colored by the magnitude of the velocity $U_{x\text{-}z}$. As was expected from the visualization experiments, the flow is relatively smooth with dominant streamwise velocity component. The distinct differences between the near-end velocity and the velocity in the central part are

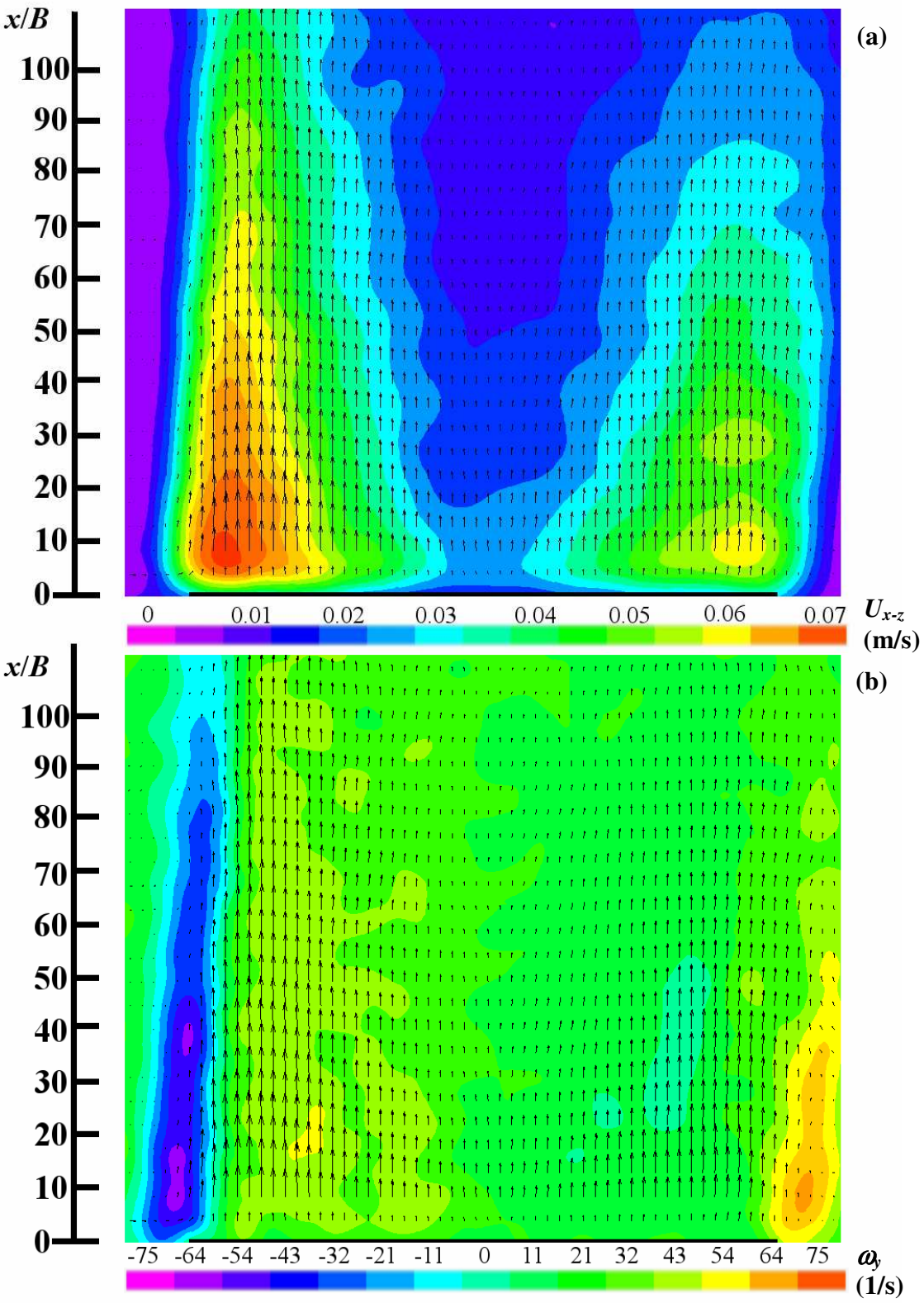

Fig. 5.3 Velocity vector field of the CJ along the slot (*x*-*z* plane) colored by
(a) Velocity magnitude,
(b) Vorticity.

evident. The differences are about 50%. The jet creates typical saddle-back velocity profiles. In this case, the existence of a saddle-back velocity profile is probably also supported by the shape of the cavity and consequent short exit channel, see Fig. 2.1. Moreover, the jet exhibits a slight asymmetry – the maximum velocity in the left part of the jet is higher by approximately 15% in comparison with the maximum velocity on the right. The small difference between the left and right part is probably caused by imperfections of the nozzle geometry.

Figure 5.3(b) shows another presentation of the same vector field as is in Fig. 5.3(a). Here, the vectors are colored by the corresponding vorticity ω_y. The vorticity field is rather monotonic, the values are low and almost constant in the entire flow. The higher values are identifiable only near the both edges of the jet where the jet in the shear layers interacts with the still ambient water.

To explore the behavior of the jet in more detail, two vector maps are shown in Fig. 5.4(a). The measurement was performed across the slot, at the positions z/B = -41.7 (z = -15 mm, left picture) and 0 (z = 0, right pictures). These coordinates correspond to positions where the maximum and the minimum velocity were identified, i.e., where the one of the local maxima and the local minimum of the saddle-back profile are situated. The vectors are colored by the velocity magnitude $U_{x\text{-}y}$. The velocity fields, in both locations, are qualitatively similar. The jet is acceptably symmetrical, although a slight asymmetry and deflection to the right is visible in the image from the middle of the slot. The width of the jet is also comparable in both cases. From a quantitative point-of-view, the pictures differ dramatically; as expected from previous measurement results (Fig. 5.3(a)), the velocities in the peak of the saddle shape (z/B = -41.7) are approximately 50% higher than in the central part (the local maximum $U_{x\text{-}y}$ = 0.055 m/s at the z/B = -41.7 against the local maximum $U_{x\text{-}y}$ = 0.024 m/s at the z/B = 0).

The corresponding vorticity maps for the velocity fields from Fig. 5.4(a) are shown in Fig. 5.4(b). The overall values of vorticity are higher in the z/B = -41.7 position where the distinctly higher velocity gradient in the shear layer results in higher vorticity values and thus more intensive mixing there.

The corresponding streamlines for the flow-field from Figs. 5.4(a) and (b) are shown in Fig. 5.4(c) and confirms the smooth nature of the jet.

To make the picture complete, note here that the velocity and vorticity maps of the jet in all the measured locations are shown in Appendix I.

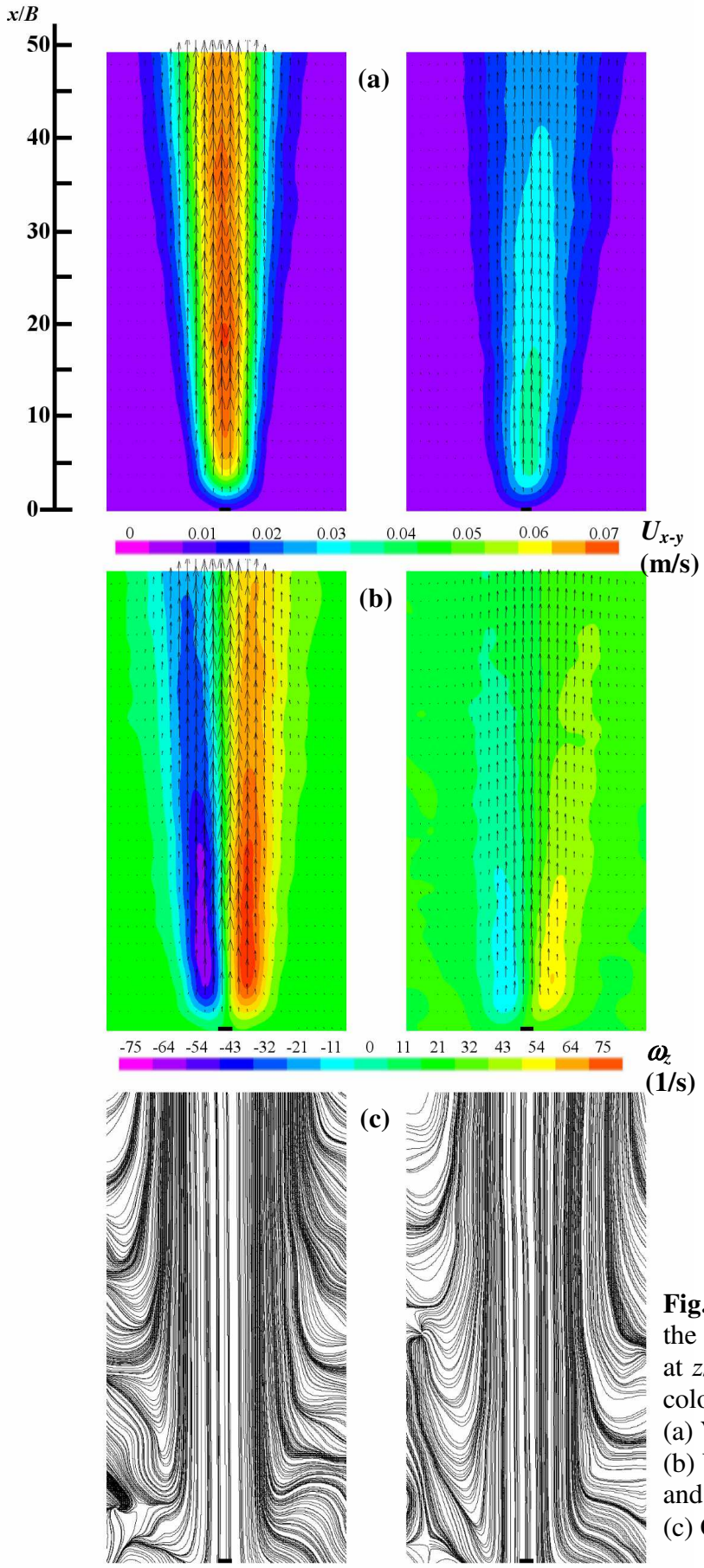

Fig. 5.4 Velocity vector field of the CJ across the slot (*x*-*y* plane) at z/B = -41.7 (left) and 0 (right) colored by
(a) Velocity magnitude,
(b) Vorticity
and
(c) Corresponding streamlines.

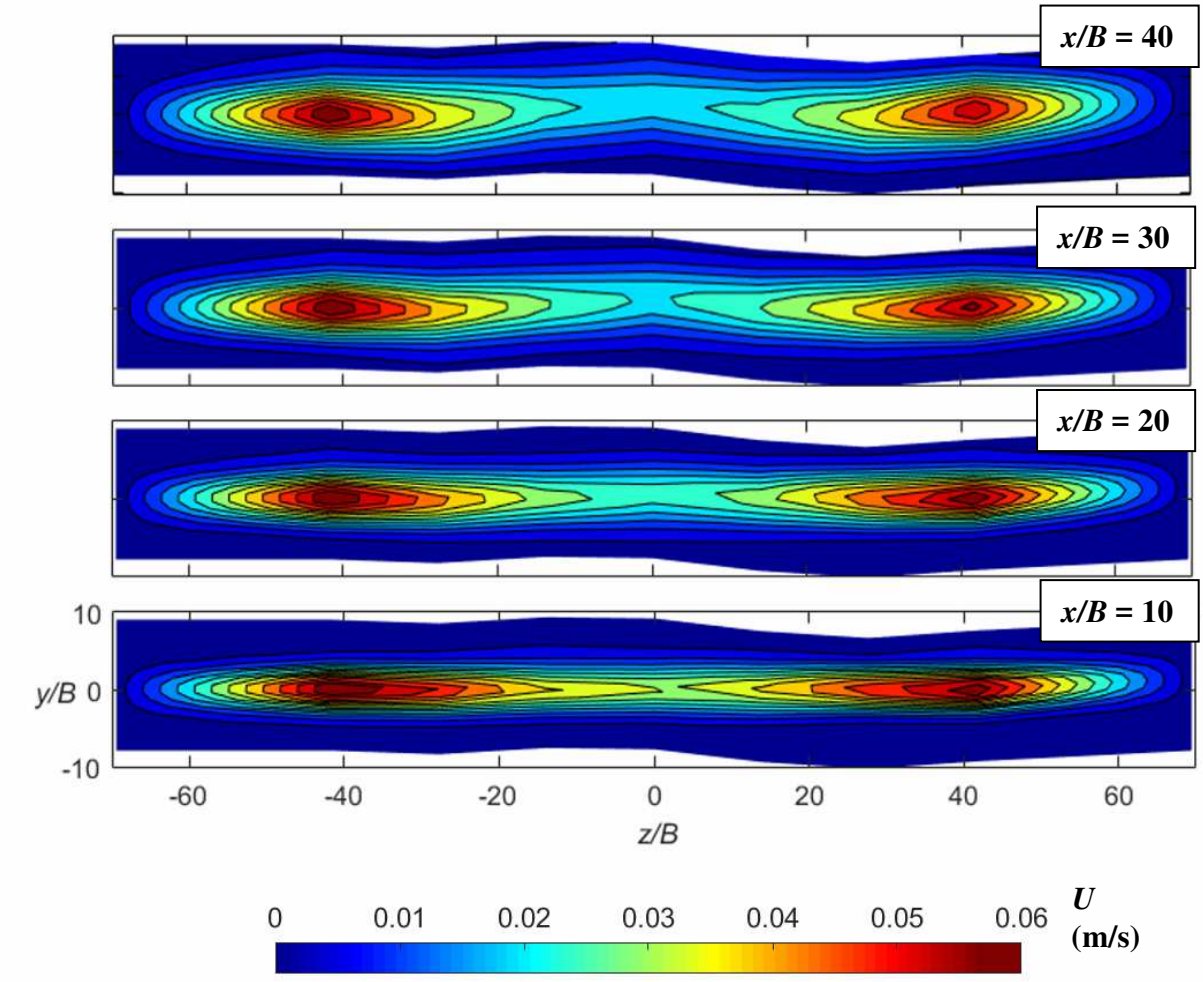

Fig. 5.5 Contours of the streamwise velocity component of the CJ.

Figure 5.5 shows the contours of the streamwise velocity component at 4 distances from the nozzle exit. The contour velocity maps are constructed from the measurements across the slot. At the coordinates from z/B = -69.4 (z = -25 mm) to z/B = 69.4 (z = 25 mm) the zero-velocity values were artificially added to the borders of the pictures. The measurement confirms the expected character of the jet; two off-axis velocity maxima are visible at distances z/B = -41.7 (i.e., z = -15 mm) and z/B = +41.7 (z = 15 mm) while the gradual decrease of the velocity in the center part of the jet is apparent.

For illustrative purposes the streamwise velocity maps from Fig. 5.5 are also shown as three-dimensional contour plots in Fig. 5.6. The nature of the jet is clearly visible – two off axis peaks near the ends of the nozzle slot ($z = +L_s/2$ and $z = -L_s/2$) and the lower velocity in the center of the jet create a typical saddle-back profile.

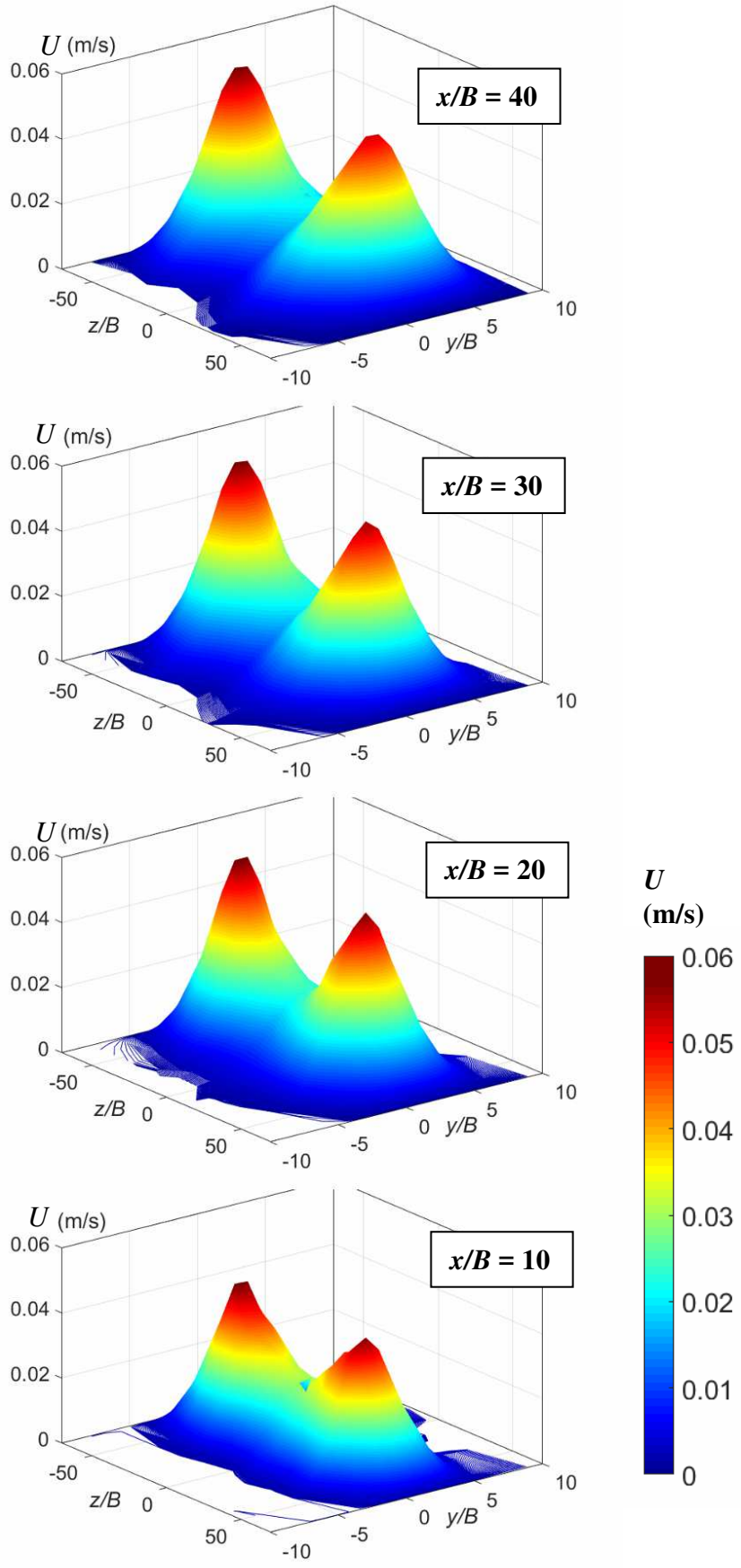

Fig. 5.6 3D contours of the streamwise velocity component of the CJ.

For these reasons described in section 3.2 the PIV measurement undervalues the velocity magnitude in the near field – approximately for the distance $x/B < 15$ (i.e., $x \approx 5$ mm). It is obvious from Fig. 5.6, the maximum velocity (z/B = ±41.7) at the distance $x/B = 10$ is unrealistically low.

From the pictures introduced above (Fig. 5.3-5.6) some observations can be summarized:

- The jet is smooth without the apparent coherent structures and no turbulent transition was observed in this case although the Reynolds number indicates the turbulent flow.
- Neither axis switching, nor gradual merging or disappearance of the side peaks were identified as is usual for macro-jets (e.g., [19,20]. The reasons are the quite high AR and the micro-size of the jet.

The distinct saddle-back velocity profiles and the absence of a gradual merging of peaks or even axis-switching can also be supported by the chosen shape of the cavity in this case. There is likely no systematic research on the relationship between the AR and the occurrence of saddle-back velocity profiles, with or without a merging of peaks and consequent axis-switching. Such a research was only performed for the larger AR ranges. Moreover, the investigation of rectangular jets with AR > 100 is rarely available in the literature. Thus, research in this area could be beneficial; however, investigations of this kind are far beyond the scope of this study.

Streamwise velocity profiles stemming from the central part ($z/B = 0$) of the jet are shown in Fig. 5.7. The velocity profiles are reasonably symmetrical. The slight deviations from the symmetry are likely caused by some geometric imperfections of the nozzle and a relatively short exit channel (see Fig. 2.1). Figure 5.7 shows that the velocity maxima gradually

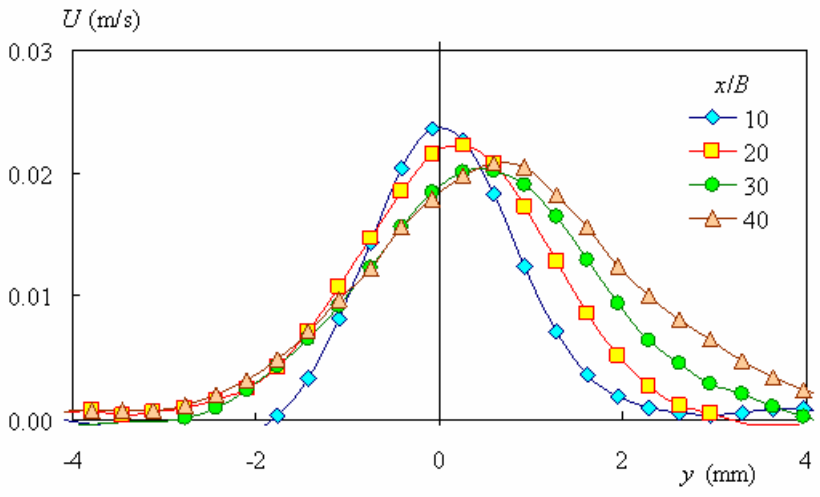

Fig. 5.7 Streamwise velocity profiles of the CJ (at $z/B = 0$).

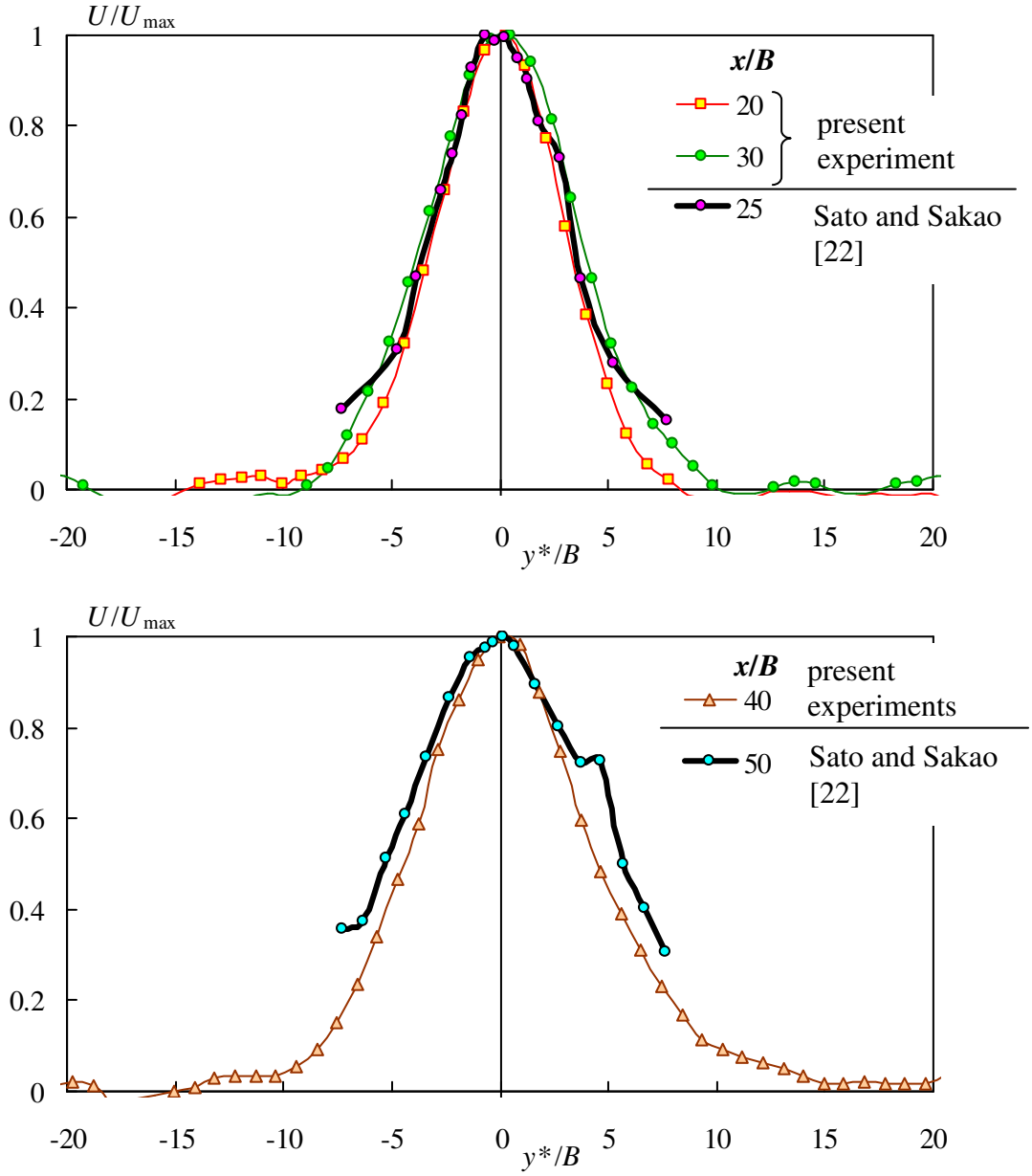

Fig. 5.8 Normalized streamwise velocity profiles of the CJ (at $z/B = 0$).

decrease as the distance from the nozzle exit increases. The position of the maxima also slightly moves to the right-hand side (a jet deflection is also visible in Fig. 5.1(a) and Fig. 5.5). The jet deflection is linked to a deformation of the whole jet along its span (see Fig. 5.2) and is likely promoted due to nozzle imperfections.

The following Fig. 5.8 shows the same velocity profiles in the dimensionless form. In order to allow the comparison with another experimental result, the profiles are shifted to ensure the maximum of every profile is on the axis (a new auxiliary coordinate y^* is used). The present results are compared with the experimental results by Sato and Sakao [22]. The present results

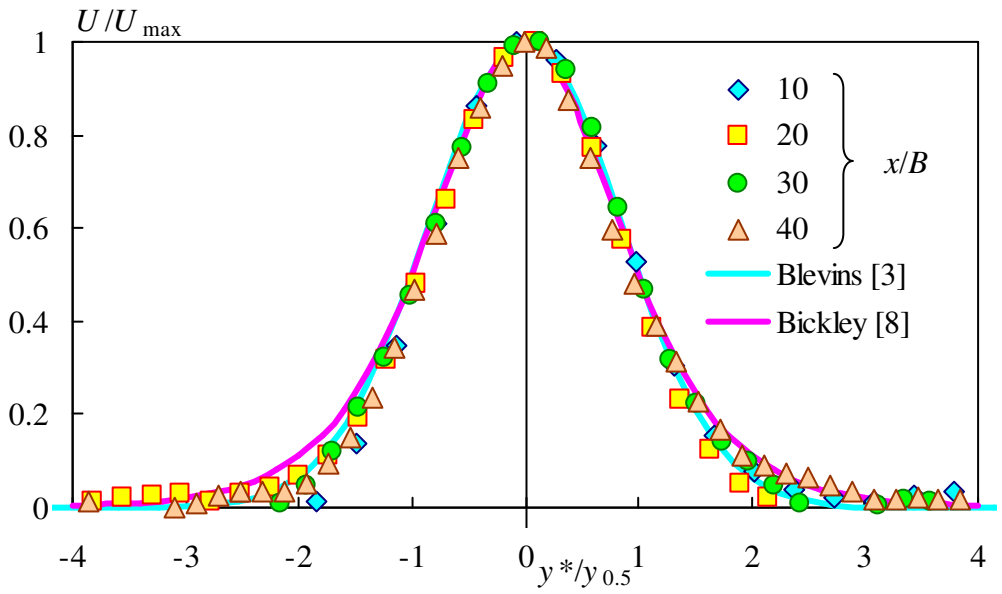

Fig. 5.9 Streamwise velocity profiles of the CJ (at $z/B = 0$) normalized using the half-width.

are in excellent agreement with older experiments [22], although the Reynolds number in [22] was even lower ($Re_{Sato} = 28$). Note that while the present jet has a Reynolds number above the limit of irregular fluctuations ($Re = 33$), the Reynolds number of the jet from the older experiments is below the limit. However both jets are rather close the limit and their behavior can be expected to be resembling. Moreover, the Reynolds number Re_{Sato} is defined in a different manner by Sato and Sakao [22], i.e., from the maximum velocity at the axis at coordinates $[x, y, z] = [0, 0, 0]$ (information about the calculations used in the present work are provided in Chapter 1.2.1.3) and no variation of the velocity along the span is assumed.

The velocity profiles from Fig. 5.8 were recalculated into non-dimensional form using the half-width of the jet $y_{0.5}$, i.e., the coordinate where the velocity $U = U_{max}/2$. It is obvious that all the profiles collapse reasonably into the same line in Fig. 5.9. For comparison purposes, the theoretical profiles according to Blevins [3] (turbulent flows, Eq. (1)) and Bickley [8] (laminar flows, Eq. (2)) are shown here as well. The difference between the present data and the representative profiles [3,8] are almost negligible around the axis. The bigger differences occur in the boundary of the jet, where the Bickley's model expects slightly higher values than the other one. The present experimental data agrees remarkably well with the theoretical results. The best agreement is obtained for the Blevins' prediction [3]. The results shown in Fig. 5.9 prove that the present velocity profiles are self-similar, even from a distance $x/B = 10$.

The relationship between the half-width of the jet and the distance from the nozzle exit is presented in Fig. 5.10(a). The curve for a turbulent 2D jet, according to Blevins [3], is plotted for comparison purposes. As expected, the half-width increases gradually with the axial coordinate, x, as the surrounding fluid is entrained into the jet. It is obvious that the half-width depends on the spanwise location and it decreases gradually with the coordinate z towards both ends of the jet (see Fig. 5.10(a) for z/B from 0 towards $z/B = \pm 15$). The present $y_{0.5}/B$ data for $x/B \geq 20$ reasonably agrees with the values determined by Blevins [3]. However, the inclination of the present results is smaller. The main reason for this is a relatively low Reynolds number of the examined jet, which is not typical in turbulent flow. Moreover, the absence of the side walls and the aspect ratio that may not be high enough does not allow the present case (rectangular jet) to react as a plane jet. Note that Blevins [3] considers a fully turbulent flow ($Re > 3{,}000$) and an infinite length of the slot. The experimental data by Vouros et al. [20] (Re = 46,000, AR = 10), Deo et al. [15] (Re = 3,000, AR = 61) and Sato and Sakao [22] (Re_{Sato} = 28 and 69, AR = 150) are also shown in Fig. 5.10(a). The present data reasonably agrees (for $x/B \geq 10$) with the results from [15,20], although the operational parameters of [15] and [20] were quite different. Thus, the results of this study are most like the results of Sato and Sakao [22], whose operating parameters (Re and AR) were like the present ones and whose velocity profiles agree with the present ones (see Fig. 5.8). It is interesting to note that although the jets from the papers [15] and [20] have relatively low AR, the inclination of the lines are like the inclination of the curve by Blevins for a pure 2D plane jet. On the other hand, the lines representing the present results and the results by Sato and Sakao [22] for both shown Reynolds numbers (i.e., jets with rather high AR) have similar inclinations with lower angle than the lines for the other mentioned works. The Reynolds number, instead of the aspect ratio, may have the dominant role in the evolution of the half-width, however, deeper study of this phenomenon is beyond the scope of this work.

The volumetric flow rate at the nozzle exit is defined as

$$Q_0 = \int_{-L_x/2}^{L_x/2} \int_{-B/2}^{B/2} u(y,z)\,dy\,dz = \int_{-L_x/2}^{L_x/2} Q_z(z)\,dz\,. \tag{40}$$

Figure 5.10(b) shows the volumetric flow rate relative to the z coordinate, Q_z. A fluid entrainment is highly dependent on the spanwise location. The entrainment and mixing with the surroundings are very intensive near the jet ends (z = -15 mm and z = 15 mm) because the

fluid entrainment is available from both lateral and spanwise directions. On the other hand, the entrainment around the centerline (i.e., around $z = 0$) is relatively weak. The results are compared with the relationship suggested by Blevins [3] for a turbulent 2D plane jet. Apparently, the volumetric flow near the jet ends is higher than that predicted for an ideal 2D flow and vice versa, the volumetric flow near the centerline is much lower; this is likely due to the saddle-back velocity profiles, i.e., the non-uniformly distributed velocities along the span. It is also obvious that the average experimental values lie under the Blevins' line, i.e., the entrainment of the jet is lower than in the case of a typical turbulent plane jet. This again indicates that, although the jet is not laminar, the jet's Reynolds number is not high enough to consider the jet fully turbulent.

The evolution of the streamwise centerline velocity of the CJ is shown in Fig. 5.11. As expected, the velocity differs with the particular position along the span and the highest values are near the ends of the span ($z/B = \pm 41.7$), whereas the lowest values are in the center. The corresponding velocity curves, from the left and right part of the span, are symmetrical. A very slow decay of the velocity can be observed approximately from $x/B = 20$ for all curves; however, the slope differs with the position along the slot. The velocity decay is much slower than expected for a 2D jet in the characteristic region ($U/U_m \sim (x/B)^{-0.5}$) or even in a fully developed region ($U/U_m \sim (x/B)^{-1}$), see [3,11,12]. The slowest velocity decay occurs near the end of the slot, which indicates the reach of the potential core, in the peaks of the saddle-back velocity profiles, are higher against the shorter potential core region at the slot axis. The results of this study are compared with experimental results from the literature. The slow velocity decay agrees well with the decay of jets with low Reynolds number by Sato and Sakao [22] and with the decay of the microjet by Gau et al. [24]. This indicates that the mixing of the present jet and its surroundings, which is responsible for the velocity decay, is less intensive than a rectangular macro-jet. The results also show that the reach of the jet is longer than in the case of the common macro-jet. This fact is confirmed by the visualization result (see Fig. 5.1) and is also confirmed by the observations by Gau et al. [24].

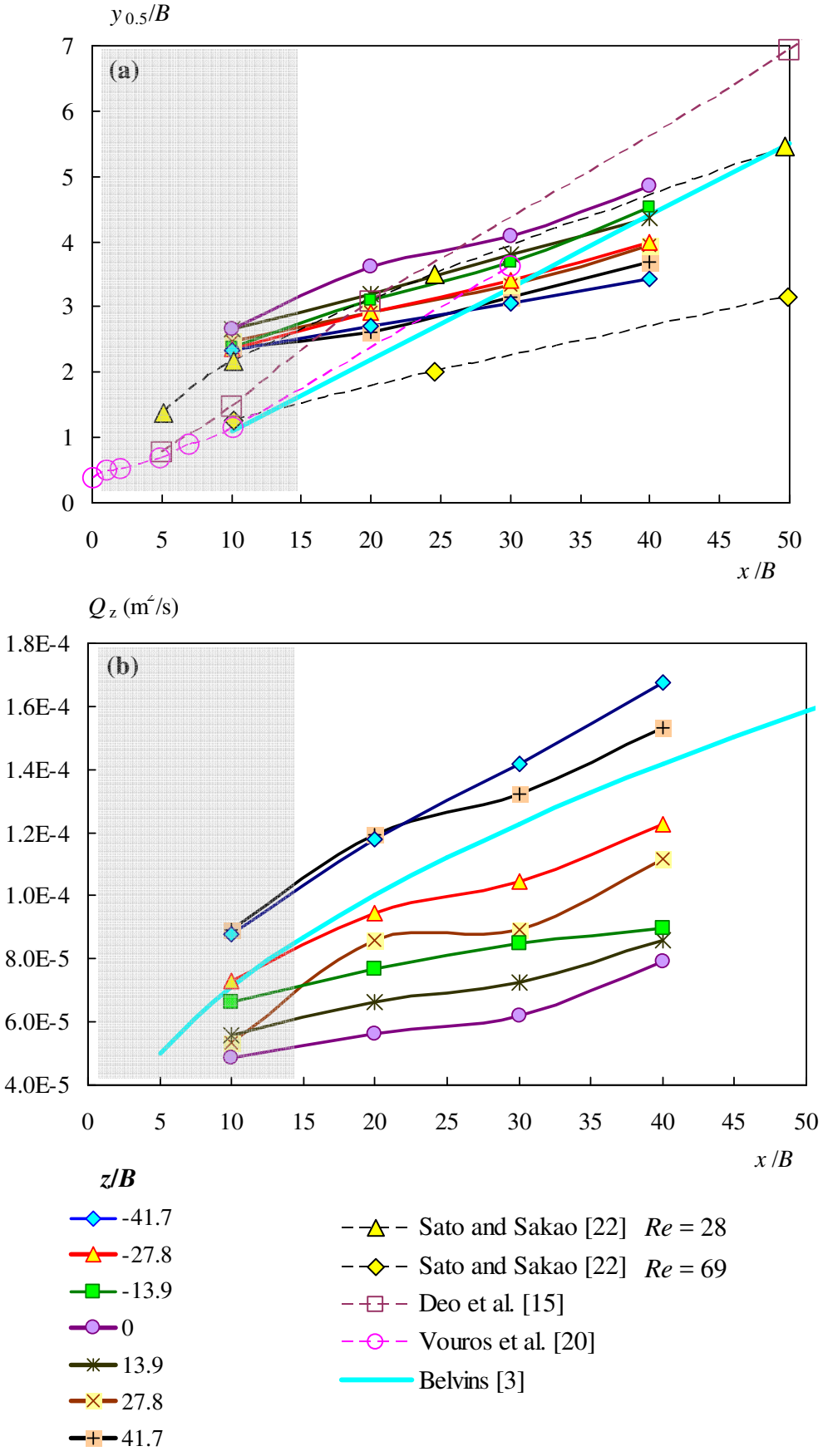

Fig. 5.10 Evolution of (a) half-width and (b) volume flux of the CJ.

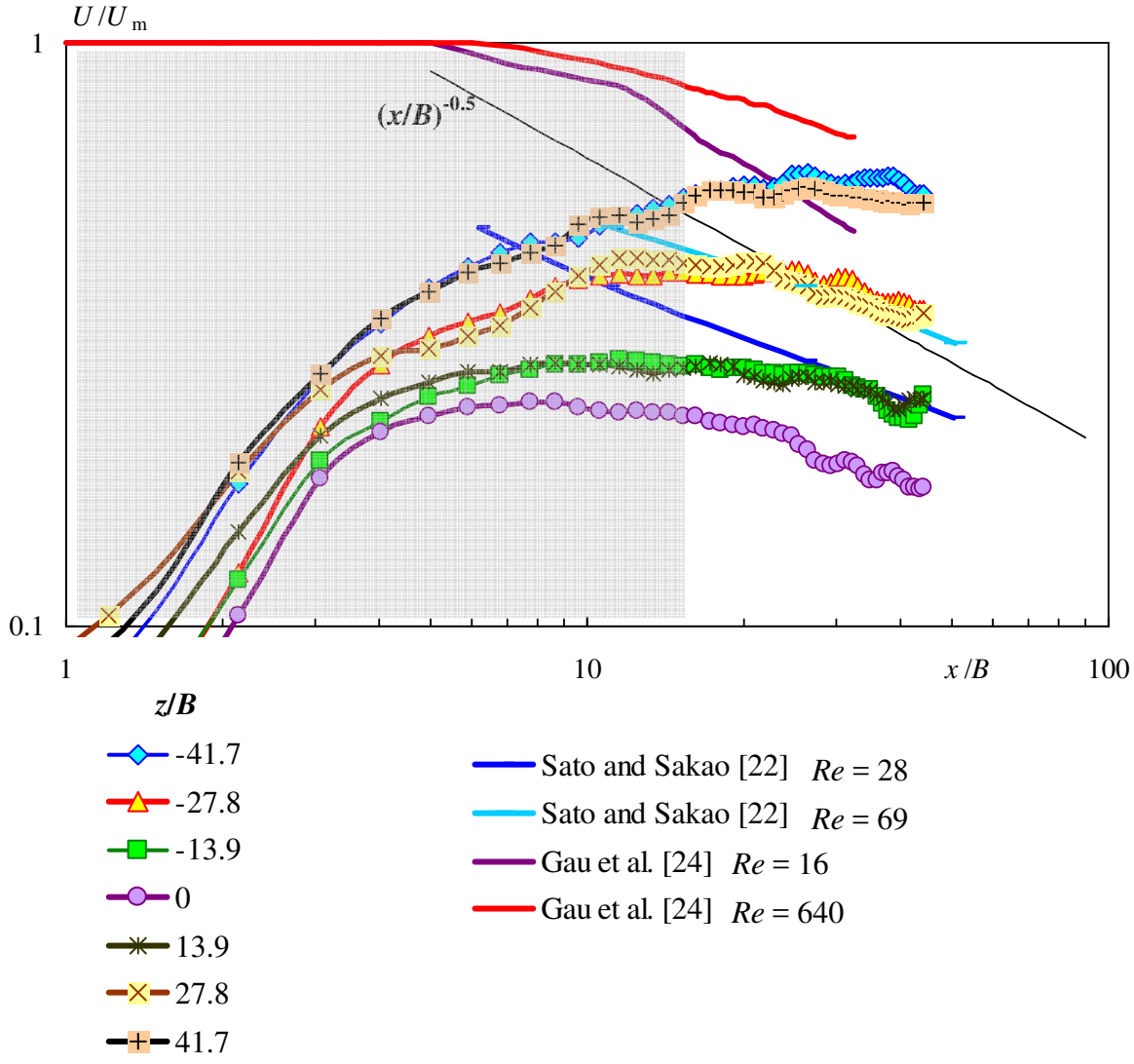

Fig. 5.11 Evolution of the streamwise component of the CJ centerline velocity.

5.2 Synthetic jet (SJ)

5.2.1 Resonance

It is known that the SJ actuators can operate very well near their resonance frequencies (see Broučková and Trávníček [129]). The theoretical first natural frequency of the present actuator is given by the equation (see [130])

$$f_{theory} = \left(\frac{1}{c2\pi}\right)\left(\frac{D_E}{D_D}\right)\sqrt{\frac{K_p}{\rho L_e}}\,, \tag{41}$$

where D_E is the equivalent diameter of the exit slot

$$D_E = \sqrt{\frac{4BL_s}{\pi}}, \tag{42}$$

$K_p = 2.2 \cdot 10^6$ N/m^3 is the diaphragm stiffness, ρ is the density of the fluid, $L_e = L + 8(2B)/(3\pi)$ is the effective length of the exit channel (see [131]) and c_s is the shape constant of the diaphragm deflection volume. The diaphragm deflection shape is approximately that of a paraboloid. To use this simplification, the shape constant would need to be set to 0.5. However, a sandwich design of the piezoceramic transducer, with an active piezoceramic central part and a larger metal diaphragm disc, results in slight differences in the paraboloid. To quantify these differences, the deflection shape of the actuator diaphragm during the cycle has been recently measured using LDV [132]. The diaphragm deflection volume was evaluated via surface integration over the diaphragm surface. Finally, the diaphragm deflection volume was evaluated as 24% greater than the paraboloid volume; hence, the shape constant of $c = 0.62$ was used in this work.

Equation (41) yields the theoretical frequency f_{theory} = 45 Hz. Note that the first resonant frequency results from mechanical oscillations of the working fluid and a flexible diaphragm (neither the second resonant frequency resulting from the Helmholtz resonator, nor the higher-order resonances are considered in this study). For most experiments, the frequency very close to the theoretical natural frequency was chosen: $f = 46$ Hz.

5.2.2 Synthetic jet - LDV results

Since the dimensions of the nozzle are small, and the expected velocities are low, the PIV method is burdened with near-wall effects. Therefore, information about the velocity at the nozzle exit is difficult to acquire. Thus, evaluating the time-mean exit velocity of the SJ, U_0, is also difficult. Because of the zero-net-mass-flux nature of the SJ, the gravimetric method (which was useful for CJ) cannot be used. To obtain the spatial-mean exit velocity, the LDV measurement of the piezoceramics diaphragm deflection, during the cycle, was performed.

Figure 5.12 shows a velocity cycle of the diaphragm center $v(t)$ at $f = 46$ Hz. The resulting curve was obtained via phase averaging over approximately 80 instantaneous velocity cycles.

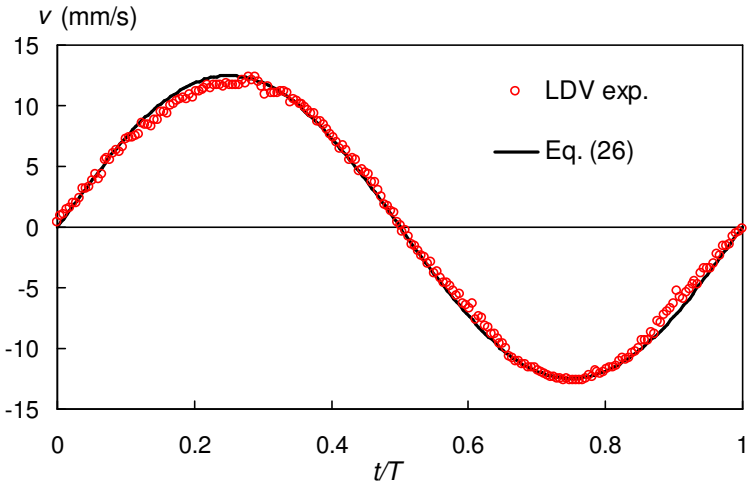

Fig. 5.12 Velocity of the oscillating diaphragm center – comparison of the LDV measurement (LDV exp.) and the sinusoidal approximation Eq. (26) with the maximum velocity of 12.5 mm/s.

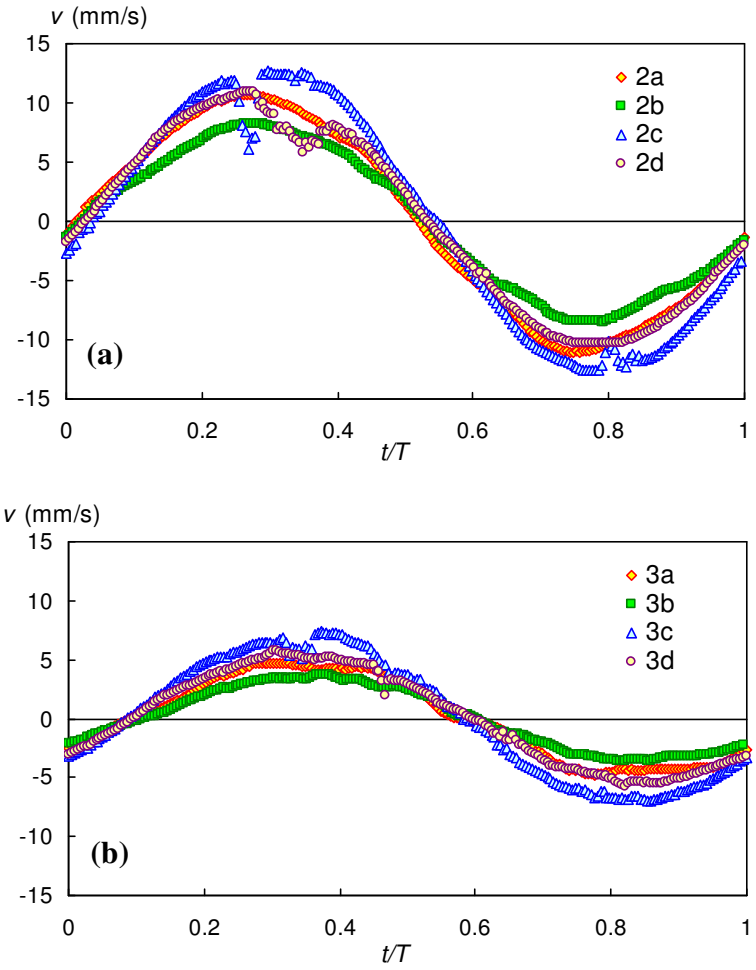

Fig. 5.13 Velocity of the oscillating diaphragm at the diameters of (a) 20 mm and (b) 34 mm.

Note that the half cycles, with positive/negative velocities, represent the extrusion/suction strokes of the SJ. The LDV experiment can be easily approximated via Eq. (26) with a maximum diaphragm velocity $2\pi f y_{max} = 12.5$ mm/s. A very good agreement of both curves is evident from Fig. 5.12.

Figures 5.13(a, b) show the phase-averaged velocity cycles evaluated from the LDV experiments at diameters of 20 mm and 34 mm, respectively. The measurements on a circle, with a 20 mm diameter, were made in 4 points (named 2a, 2b, 2c, 2d) that were equidistantly distributed, as shown in Fig. 3.5. Similarly, measurements on the concentric circle with a 34 mm diameter were made in the points 3a, 3b, 3c, 3d (Fig. 3.5). Again, resulting velocity cycles were obtained via phase averaging over approximately 80 cycles.

The approximately sinusoidal off-center cycles are like the cycles of the diaphragm center. Obviously, the velocity amplitude decreases with increasing distance from the diaphragm center. The amplitude slightly differs also along the investigated diameters (points a, b, c, d), i.e., the deflection of the diaphragm is not ideally symmetrical. The reasons are deviations from the geometry, namely deviations in diaphragm clamping around its perimeter and the non-homogeneousness nature of the transducer piezoceramics. Moreover, some disturbances and discontinuities of cycles (e.g., at the diaphragm perimeter, see curve 2c) can be of an optical nature, such as laser scattering at the rim of a piezoceramic transducer for the 24-mm diameter circle and a reflection of the non-uniformity of the measured surface. Minor reasons could be impurities in the water and non-uniformities of the glass wall.

A phase shift between the center and the perimeter of the diaphragm can be evaluated via a comparison of Fig. 5.12 and Figs. 5.13(a) and (b), respectively. The phase delay at the off-center locations, compared with the center, is approximately 13° (for a diameter of 20 mm, Fig. 5.13(a)) and 35° (for a diameter of 34 mm, Fig. 5.13(b)).

Using Eqs. (25 and 26), the local phase-averaged velocities from Figs. 5.12 and 5.13 were integrated in time and the local displacement Δy was obtained for every measured diaphragm point. As an example, the resulting profiles of the diaphragm displacement along the a–c line are shown in Fig. 5.14 at the four instants during the working cycle $\varphi = 0$, 90, 180, 270°. Despite some deviations from an ideal symmetry, Fig. 5.14 corresponds with the expectations since the center moves with the highest amplitude and the phase shifts are also visible.

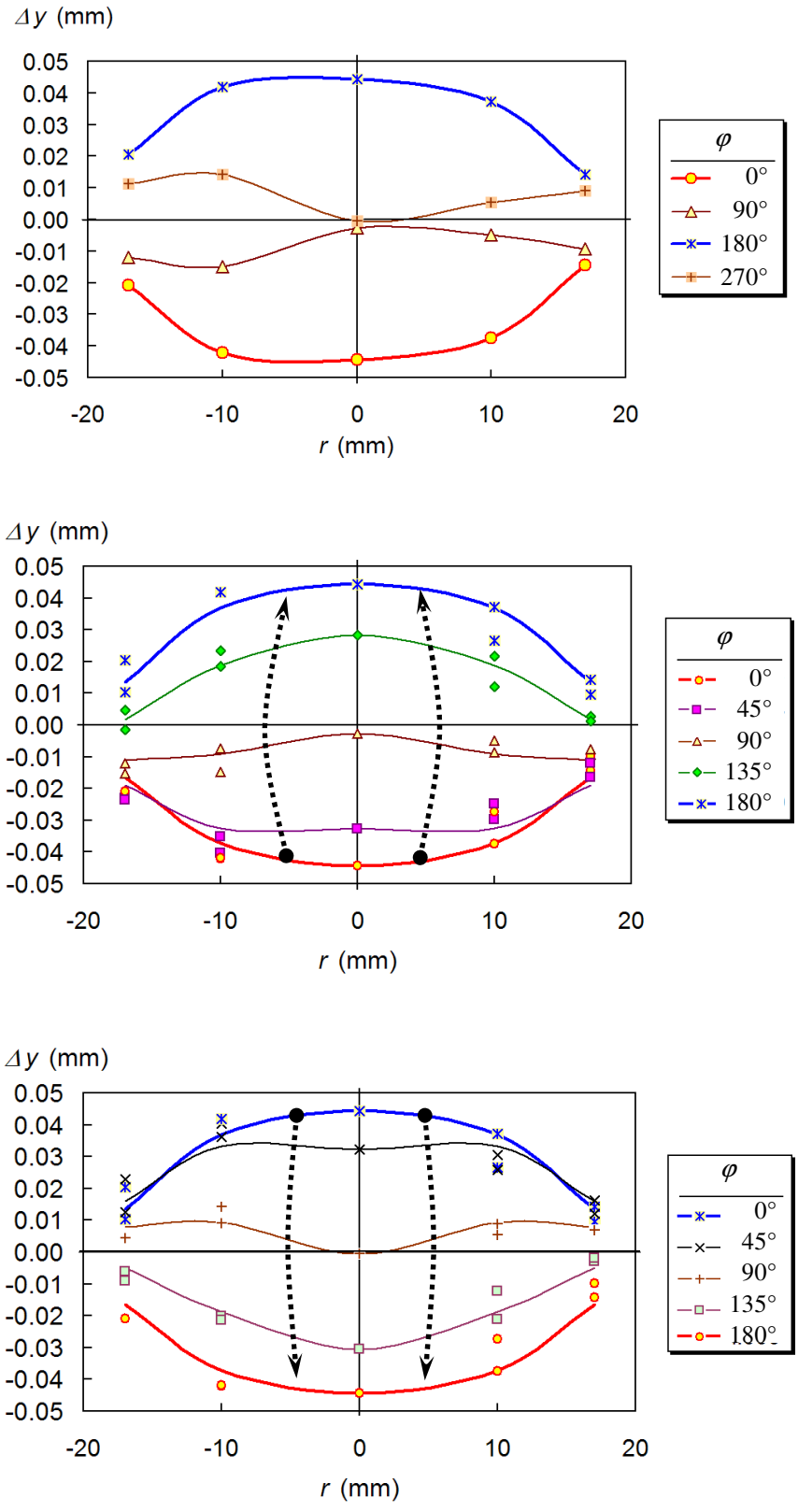

Fig. 5.14 Profiles of the diaphragm displacement
(a) measurement along the a–c line from Fig. 4.7,
(b) extrusion stroke, profiles averaged from all four a,b,c,d measurements,
(c) suction stroke, profiles averaged from all four a,b,c,d measurements.

The local displacements, measured using the same diameters, were averaged and the resulting deflection profiles are shown as lines for the extrusion and suction parts of the cycle, in Figs. 5.14 (b and c). To demonstrate the deviations of the point measurements from these averaged deflection lines, the experimental points are also shown in Figs.5.14(b, c).

To evaluate the fluid volume extruded during the working cycle, the averaged profiles from Fig. 5.14 were integrated. Assuming incompressible flow and the slug flow model for the fluid flow through the SJ slot nozzle (one-dimensional or "piston-like" flow), the continuity equation yields an SJ orifice velocity of $U_0 = 0.21$ m/s and a corresponding Reynolds number of $Re = 78$, as described in [132]. The LDV measurement of the diaphragm's deflection shape is reliable for an evaluation of the exit velocity U_0 (and the Reynolds number). However, this approach is too time-consuming, if not clumsy, when more complex experiments focus on many quantities, such as simultaneous flow visualization by LIF, PIV experiments and heat transfer measurements. In these cases, the U_0 exit velocity can be evaluated from a versatile and easier one-point measurement at the diaphragm center. Considering incompressibility, continuity equation and the slug flow model for fluid flow (via an SJ slot nozzle), the SJ exit velocity can be evaluated using

$$u_0(t) = c_s(A_D/A_s)\, v(t). \tag{43}$$

The time-mean exit velocity U_0 can be evaluated via integration of Eq. (34) of the sinusoidal process of $u_0(t) = U_{max} \sin(2\pi ft)$, where $U_{max} = 2\pi f c_s y_{max}(A_D/A_s)$. However, the variability in the deflection shape of the diaphragm can enhance uncertainties of the c_s value, which can enhance uncertainties of the resulting U_0.

Finally, the time-mean exit velocity U_0 and the SJ Reynolds number were evaluated as

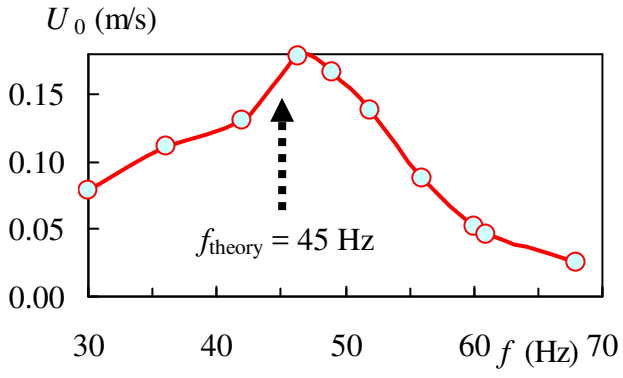

Fig. 5.15 Frequency characteristics of the SJ actuator obtained by LDV measurement.

U_0 = 0.18 m/s and Re_{SJ} = 67. The values reasonably agree with the previous LDV experiment (U_0 = 0.21 m/s and Re = 78, [132]); the reasons for the small differences were differences in the arrangement (the previous experiment was made without heated cylinder) and slight differences in the individual electromechanical parameters of various samples of the piezo-elements. Other dimensionless parameters were evaluated as L_0/B = 10.7, St = 0.29, and S = 6.28. The frequency characteristic resulting from the present LDV measurements are shown in Fig. 5.15. A significant local maximum of the velocity (U_0 = 0.18 m/s) was found at f = 46.4 Hz, which clearly indicates the resonance behavior of the system. This experimental finding agrees with the theoretically derived resonant frequency of 45 Hz, as indicated by the arrow in Fig. 5.15.

5.2.3 Synthetic jet - flow visualization

As in the investigation of the CJ, the SJ experiments began with a qualitative visualization of the flow field. The laser sheet was placed in the same location as in the CJ case, i.e., the visualization was performed via the following three arrangements (see Fig. 3.2):

- across the slot (laser sheet was in the x-y plane in the middle of the exit slot, z = 0),
- along the slot (laser sheet was in the x-z plane, y = 0) and finally,
- the laser sheet was placed in the y-z plane at several distances from the nozzle exit (specifically at x/B = 0, 10, 30, 40, 55 and 80).

The periodic nature of the SJ required to performe the visualization in a phase locked regime, i.e., for several phases of the SJ cycle.

Figure 5.16 shows the visualization across the slot in the middle of the nozzle. The pictures show the evolution of the jet during one working period. The formation and downstream evolution of the vortex pair is well visible. The vortex pair leaves the nozzle, grows and is advected further downstream. Two subsequent vortex pairs are clearly visible in each picture and the third pair is apparent until φ = 108°, where it subsequently breaks up in the next part of the cycle and merges with the previously extruded vortex puffs. Because of the chosen visualization method (i.e., the contrast dye is inside the cavity and it is extruded into the clear water), the suction process is not visible in these images. When compared with the CJ (see Fig. 5.1), the SJ is wider and the width of the jet grows gradually from the beginning to the distance around x/B = 30, where the jet breaks up and its width increases distinctly. This

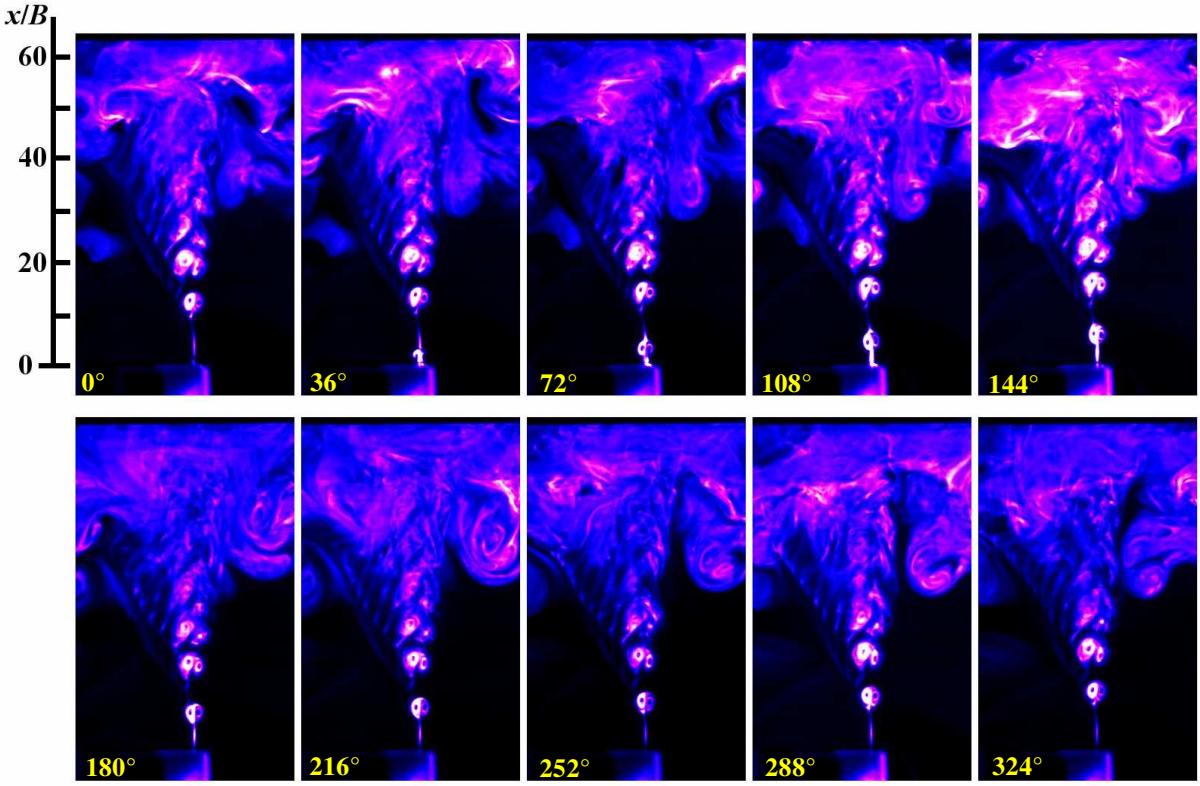

Fig. 5.16 Visualization of the SJ across the slot (*x*-*y* plane).

contrasts with the smooth and slowly changing CJ, which does not break up in the observed area.

Note another evident difference is in the visualized flow fields of SJ and CJ. The SJ has large vortices that appear at the top of the observed area – see $x/B > 40$ in Fig. 5.16. The reason is likely an interaction between SJ and the free water surface (approximately at $x/B = 80$). These unsteady impinging effects were not developed for the smooth CJ case (see Fig. 5.1).

The visualization of the SJ along the slot is presented in Fig. 5.17. Similarly to previous Fig. 5.16, the formation and the evolution of the rows of vortex pairs can be observed. The initially straight lines of the vortex pairs are slightly bent in their middle part. The advection velocity of the vortex pair is probably higher in the central part of the jet. Similar observations were reported by Amitay and Cannelle [62]. Likewise, in the CJ case, the non-uniformity of the jet along the span can be seen - the jet is "weaker" in the central part. The decrease of the width is gradual and rapid against the CJ (see Fig. 5.1). This agrees with the increase in the width of the perpendicular direction (Fig. 5.16). This indicates that the interaction of the shear layer, and its surroundings, are more intensive in this case.

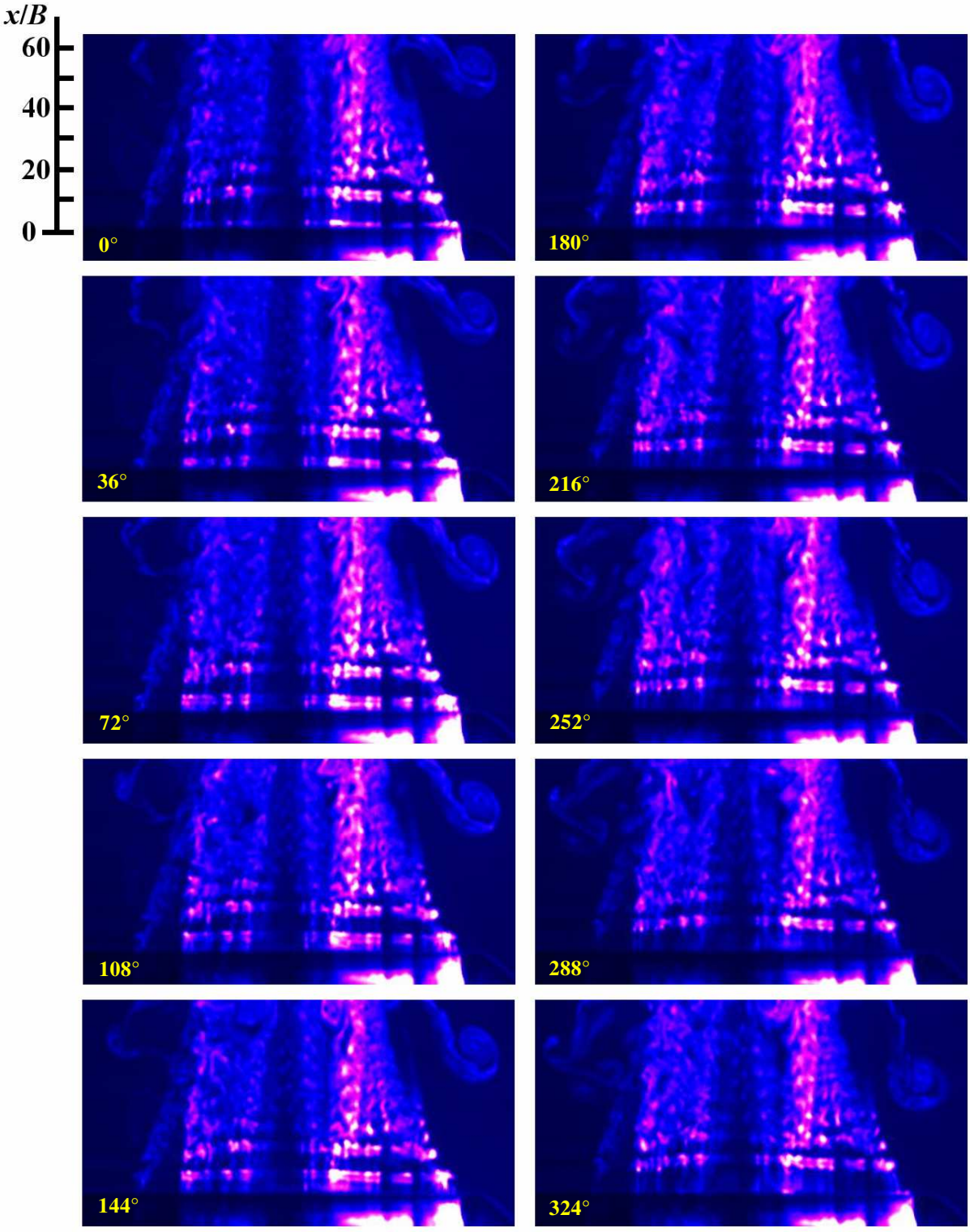

Fig. 5.17 Visualization of the SJ along the slot (*x*-*z* plane).

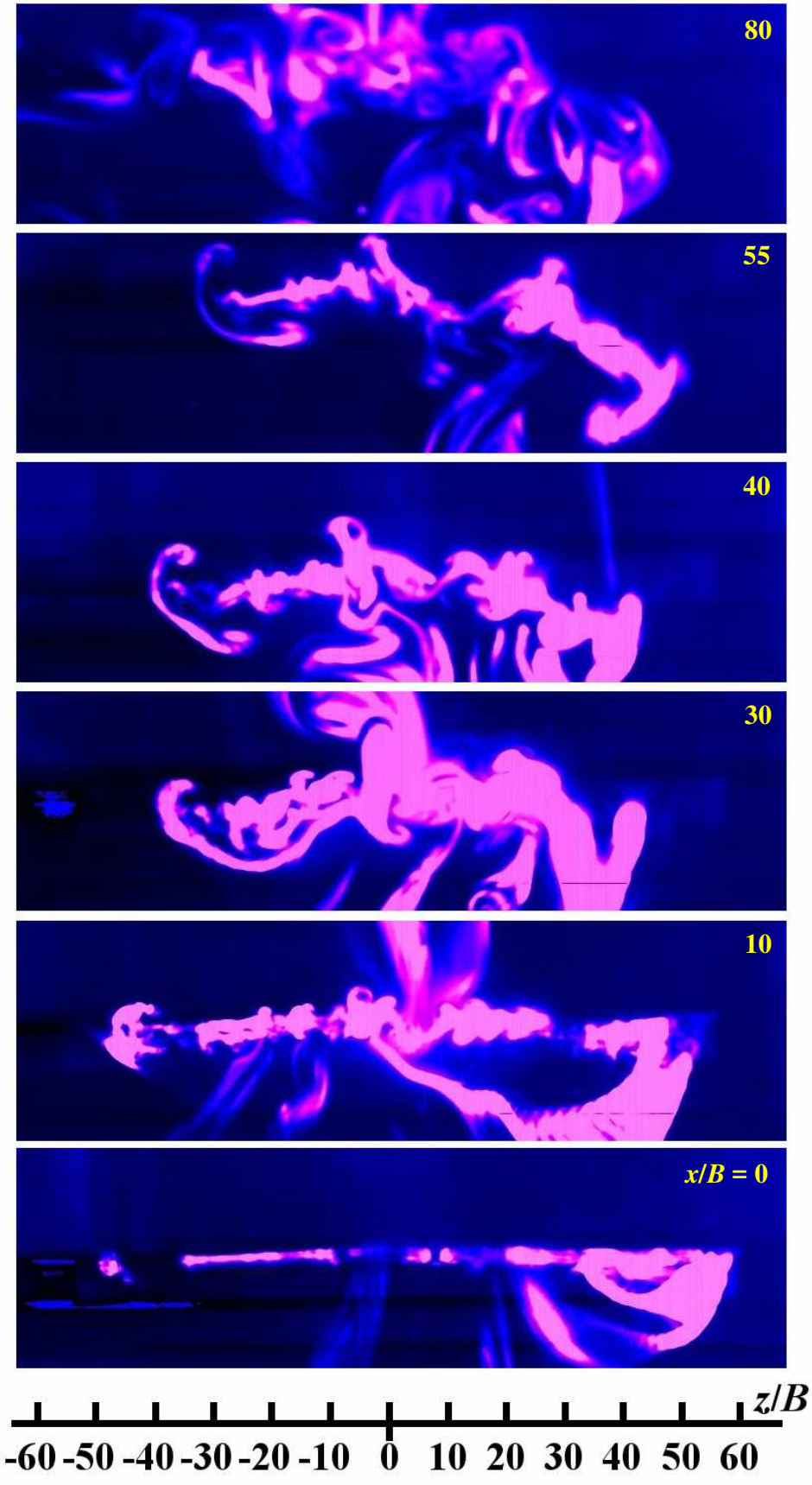

Fig. 5.18 Visualization of the SJ in *y*-*z* planes at arbitrary phase.

Figure 5.18 presents the results of the visualization in the *x*-*z* plane. The pictures were taken at arbitrary phases of the cycle. The pictures are in the agreement with the previous ones (Fig. 5.16 and 5.17) because the SJ width, both in the lateral and spanwise direction, changes distinctly. Moreover, the photographs reveal the strongly 3D nature of the SJ. Originally narrow straight SJ (at the nozzle exit $x/B = 0$) deforms considerably and becomes somewhat disturbed at larger distances. If this is compared with the corresponding pictures of the CJ (Fig. 5.2), the differences are apparent: the structure of the SJ is rather irregular at all the investigated distances (in contrast to the smooth lines of the CJ), the changes in width of the jet (which are almost negligible in the CJ case), the formation of the end vortex mushroom-like structures is distinct in the SJ case; in the CJ case the formation is also visible but only to a limited degree. The break-up of the CJ was not observed in the investigated area, on the other hand, the SJ loses its 2D appearance around $x/B = 30$. The described gentle lateral waviness of the CJ is contrasted with the quite strong and irregular lateral movement and deformation of the SJ shape observed in time.

5.2.4 Synthetic jet - PIV results

In the same manner as in the CJ case, for the quantitative examination of the SJ flow field, the PIV method was chosen. Unlike the steady CJ, the SJ experiments require to be performed in space but also in time, i.e., at several phases of the cycle. For this reason, eight phase-locked measurements, with the equidistant phase step of $t/T = 0.125$, (i.e. $\varphi = 45°$) were performed at every investigated position. Each of the resulting vector fields were obtained as the average of 100 instantaneous fields.

The measurement was performed across the slot for 4 planes parallel to the *x*-*y* plane, specifically at z/B = -41.7, -27.8, -13.9, 0 (i.e., z = -15, -10, -5, and 0 mm). The measurement along the slots were also made, i.e., at *x*-*z* plane ($y = 0$), again at 8 phases of the cycle. The schematic illustration of the individual positions of the laser-sheet is the same as shown in Fig. 3.2 (where only certain positions were considered). The periodical flow of the field for the investigated SJ were represented by a total number of 4000 instantaneous images, which were used for data processing.

Figure 5.19 shows the velocity vector field of the SJ along the span at 8 phases of the cycle. In Fig. 5.19, the vectors are colored by the velocity magnitude $U_{x\text{-}z}$. The first four pictures represent the extrusion part, while the others the suction part of the working period. The most marked feature of the jet is apparent in all the phases: the velocity distribution is not uniform

along the span. Like CJ, the local maxima of SJ are visible near the ends of the jet span, but also, the additional third peak appears approximately in the center of the span. Note that existence of the middle-peak was discussed in literature many times (see the experimental works by Smith an Glezer [29], Amitay and Cannelle [62] and Gillespie et al. [53]). In the present case, the initially 2D jet breaks into three nearly separate streams. However, the vector field located further downstream (around $x/B = 120$ and further) indicates that the separate jet streams merge again as the jet becomes narrower in the far-field. The jet does not change a lot during the period. Obviously, the most distinct changes would be visible near the vicinity of the nozzle exit, where the suction itself occurs. Capturing this phenomenon is not possible using the present method because of the near wall effects and the limitations of the present method, as discussed in section 3.2.

The vorticity fields (ω_y) corresponding to the vectors from the Fig. 5.19 is shown in Fig. 5.20. The break-up of the jet into three streams is apparent. The pairs of regions of the positive and the negative vorticity are visible not only at the ends of the jet span, but at borders of each of the three streams. The level of the vorticity is comparable in all three streams. Similar observations of "streaky-like" vorticity patterns were made by Gillespie et al. [53] and Amitay and Cannelle [62]. This phenomenon relates to the spanwise instability of waves as concluded by Amitay and Cannelle [62]. The present vorticity field resembles case (a) from [62] (AR = 50.8, $L_0/B = 16.6$), see Fig. 1.3, although the present operating parameters are a bit different (AR = 111, $L_0/B = 10.2$). The spanwise wavelengths at $x/B = 35$ are commensurate in both cases: $\lambda_z \sim 0.15L_s$ and $\lambda_z \sim 0.115L_s$ in the present case and the research by Amitay and Cannelle [62], respectively. The $\lambda_z \sim 0.15L_s$ wavelength is shown in Fig. 5.20. Surprisingly, the case with the most similar operating parameters (case (g) from Fig. 1.3, AR = 101.6, $L_0/B = 16.6$) has a much finer structure than the present case. On the other hand, the change of the stroke length, with a constant AR, only has a small influence on the value of the spanwise wavelength. The increase of the stroke length is manifested only by the less organized structure of the vorticity field, as reported by Amitay and Cannelle [62]. The spanwise instability waves and the corresponding spanwise wavelength are probably also influenced by another operating parameters, such as the frequency of the SJ, the absolute velocity and dimensions or the initial instabilities given by the individual geometry etc. However, deeper analysis of discrepancies between the present results and the results by Amitay and Cannelle [62] is beyond the scope of this work.

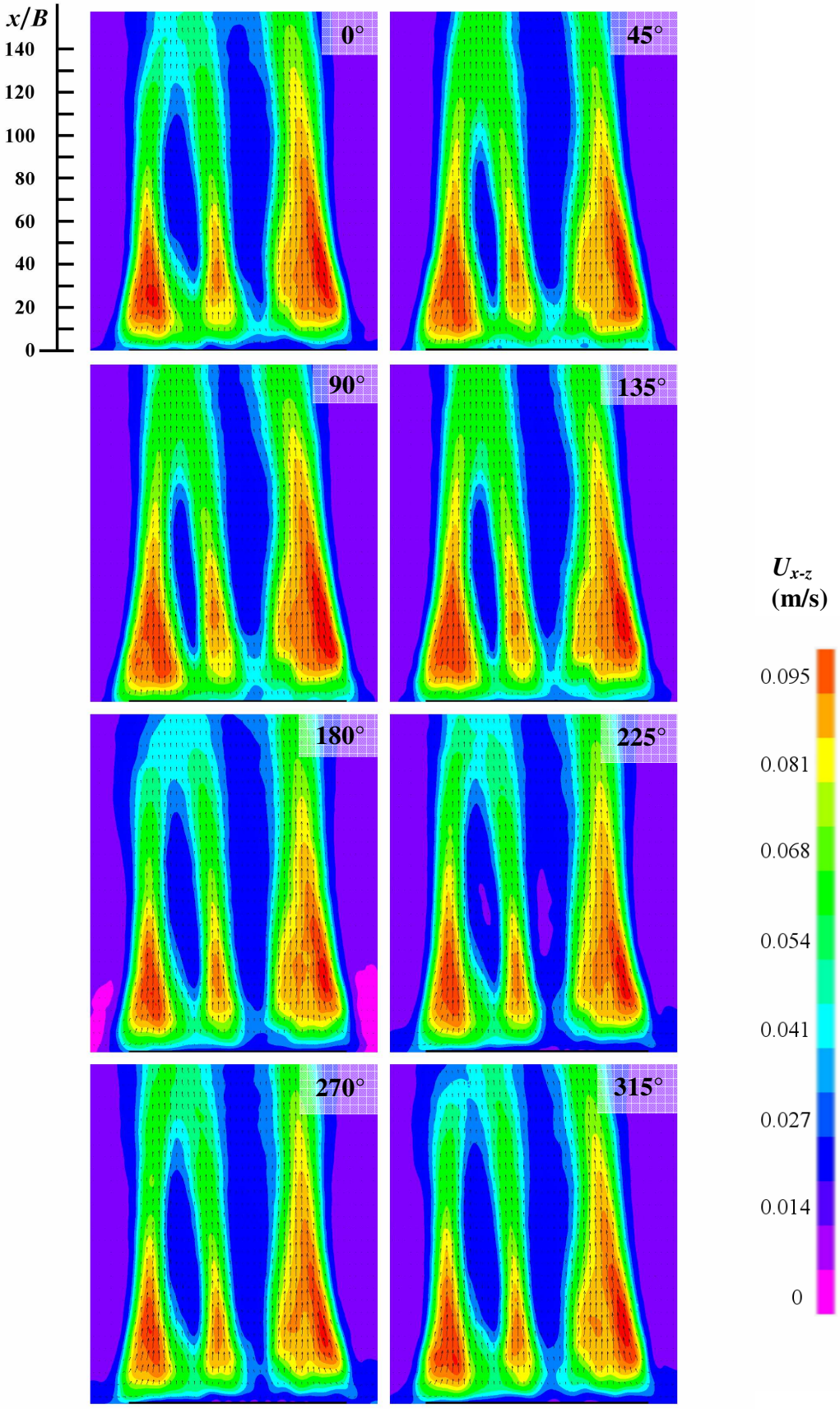

Fig. 5.19 Velocity vector field of the SJ along the slot (*x*-*z* plane) colored by the velocity magnitude.

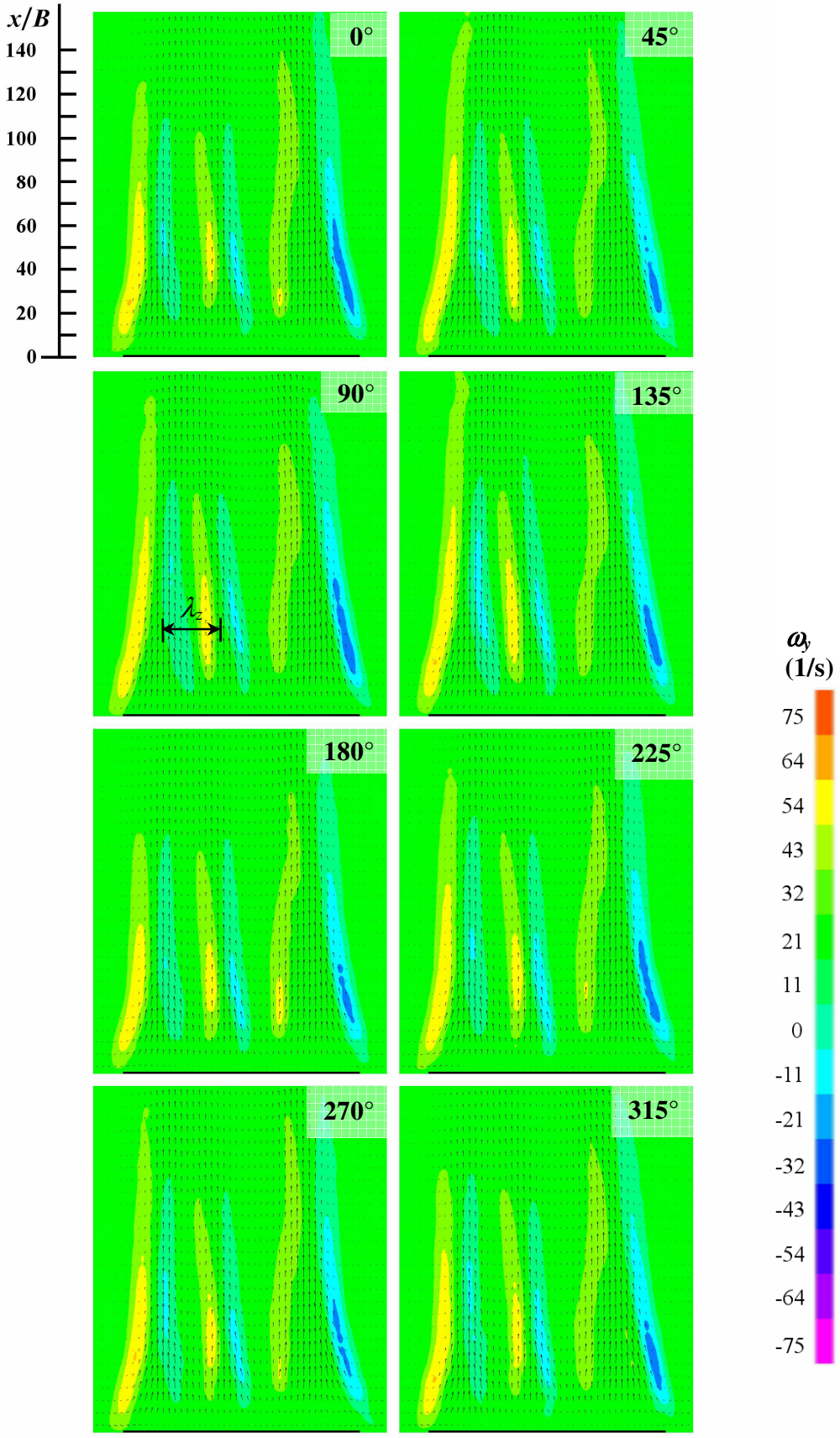

Fig. 5.20 Velocity vector field of the SJ along the slot (*x*-*z* plane) colored by vorticity.

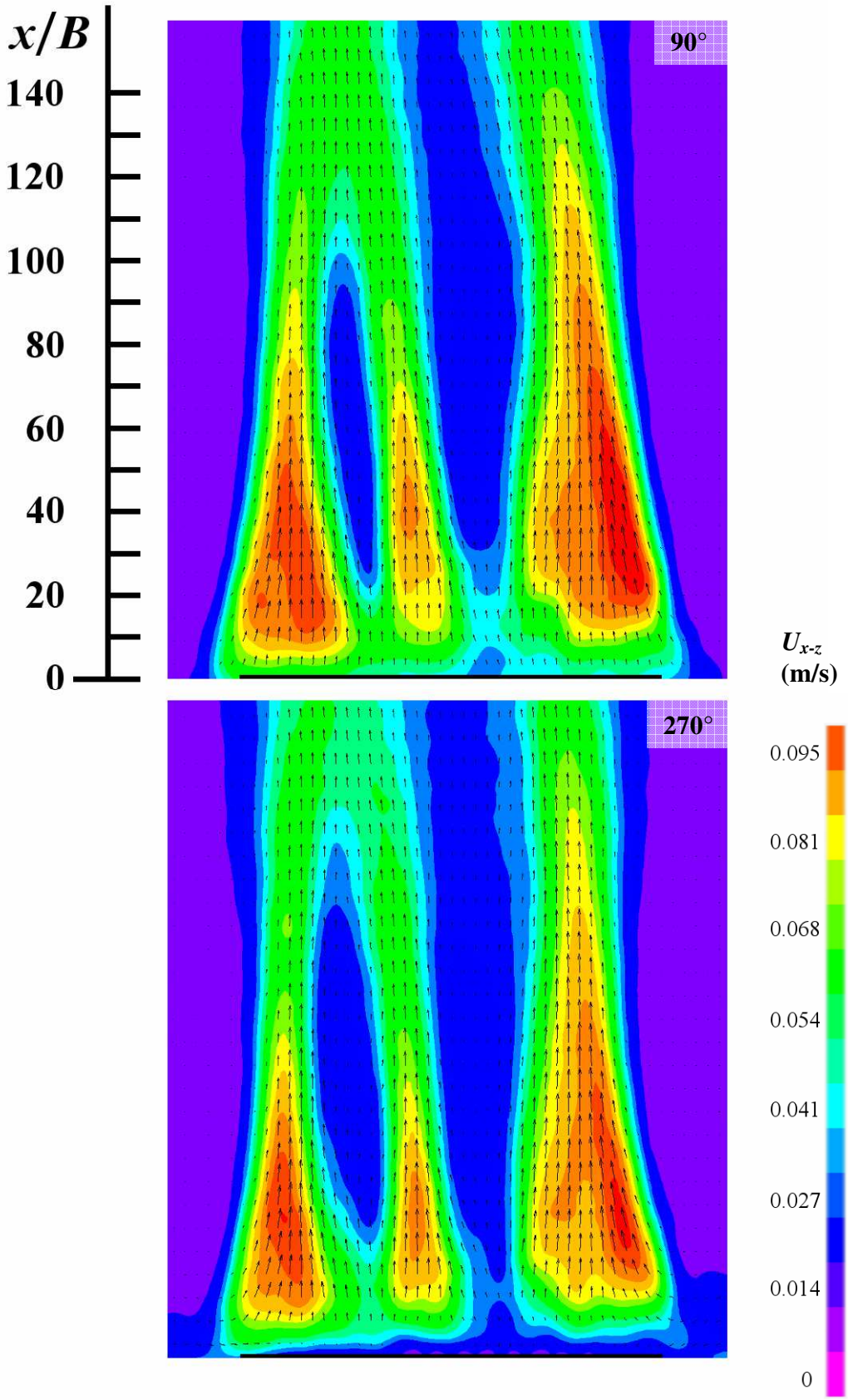

Fig. 5.21 Velocity vector field of the SJ along the slot (*x*-*z* plane) colored by velocity magnitude (detail view).

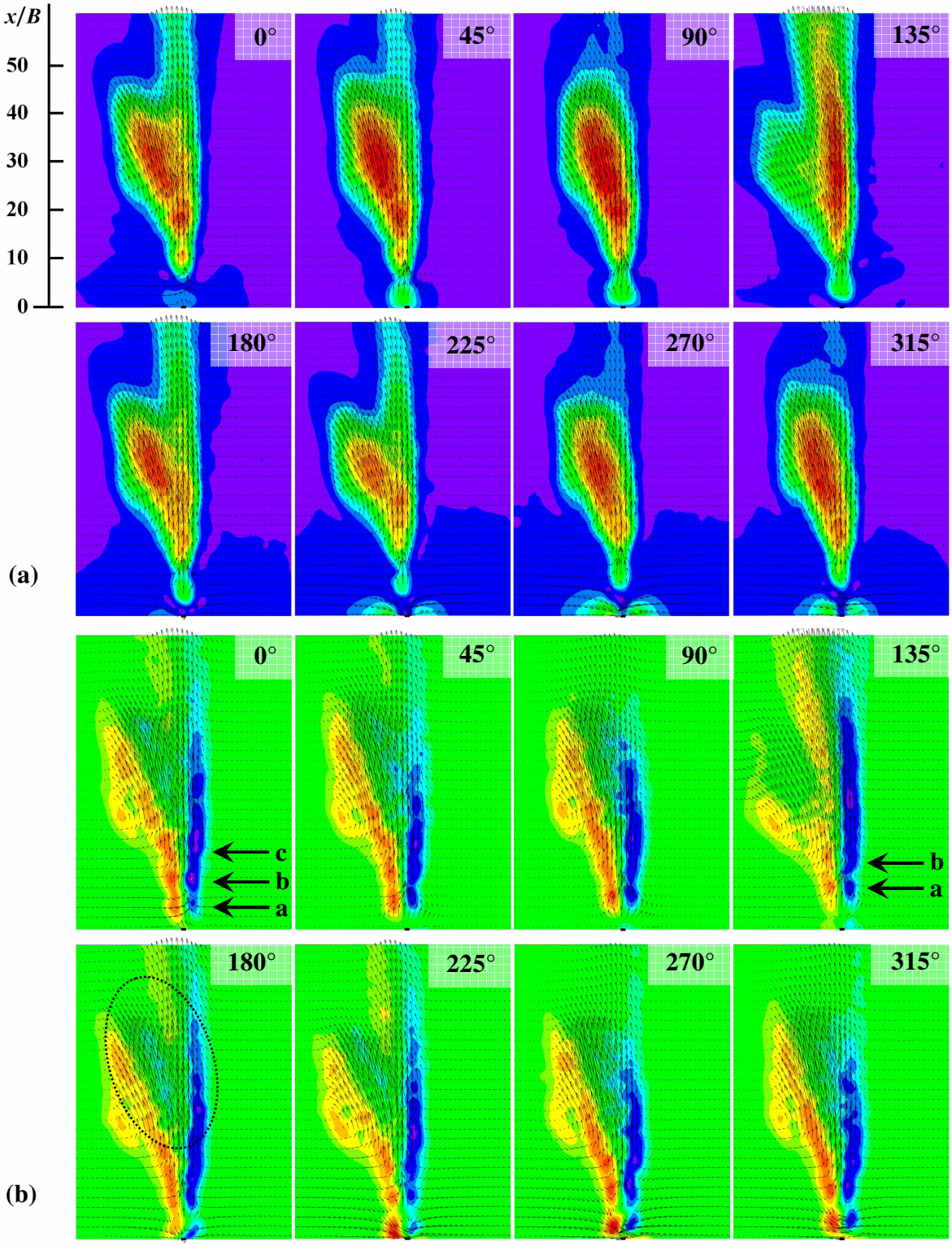

Fig. 5.22 Velocity vector field of the SJ across the slot (*x*-*y* plane) at *z*/*B* = -41.7 colored by
(a) Velocity magnitude
(b) Vorticity
(the velocity and vorticity scale is the same as in Fig. 5.19 and 5.20, respectively).

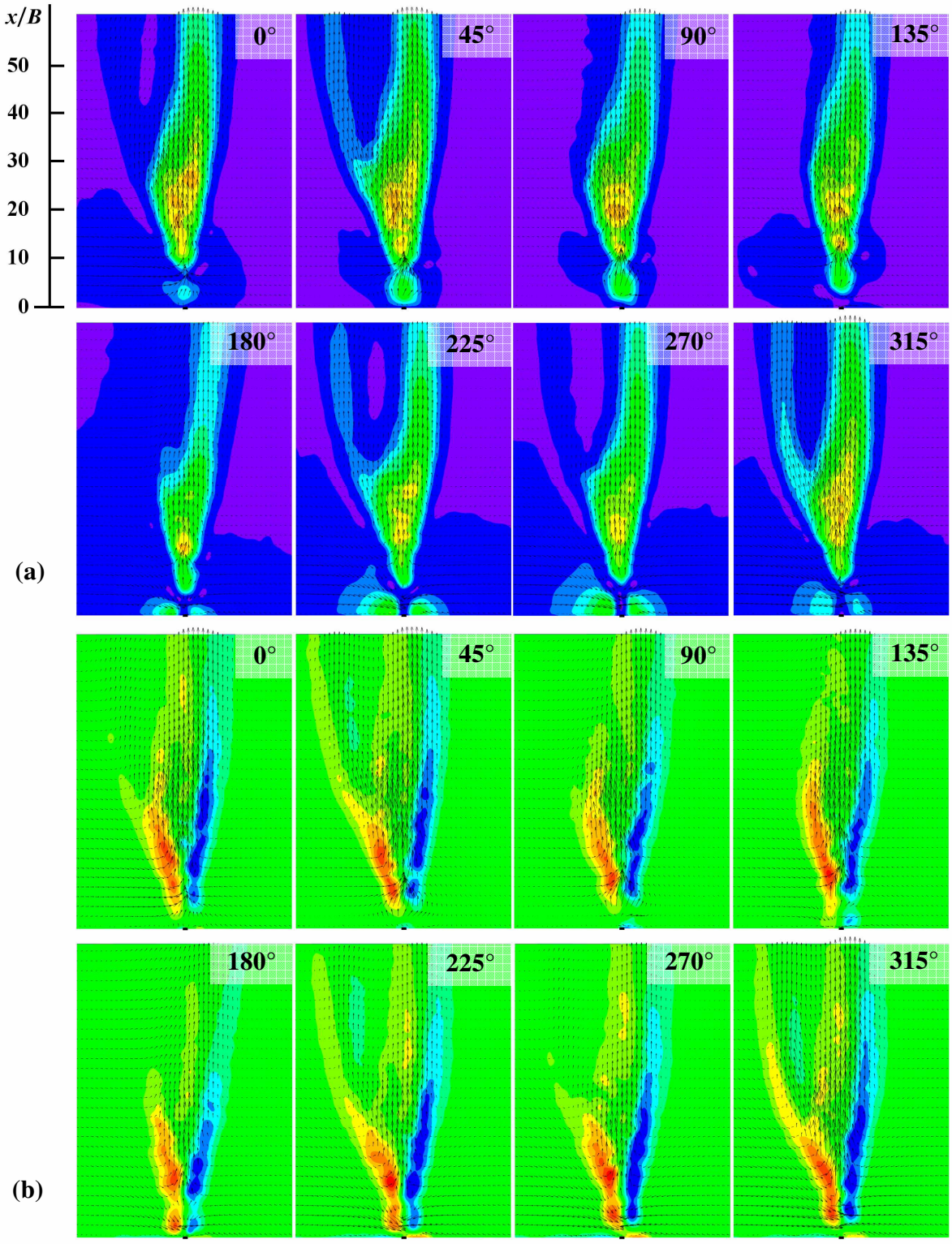

Fig. 5.23 Velocity vector field of the SJ across the slot (*x*-*y* plane) at $z/B = 0$ colored by
(a) Velocity magnitude
(b) Vorticity
(the velocity and vorticity scale is the same as in Fig. 5.19 and 5.20, respectively).

To show the vector field in more detail, the selected pictures from Fig. 5.19 are enlarged and shown in Fig. 5.21. The pictures show the instantaneous flow field of the maximum extrusion (φ = 90º, Fig. 5.21(a)) and maximum suction (φ = 270º, Fig. 5.21(b)). As in the previous picture, the three (nearly) separate streams are visible and the jet is approximately symmetrical in the near field. The slight asymmetry in the far-field is likely promoted by the initial imperfections of the nozzle geometry. Besides, Figure 5.21 indicates the very small influence of the jet origin (namely extrusion/suction phases) on the jet's far-field. The only clearly visible difference is a slight shift of the local maxima region near the ends of the span more downstream and also their reduction in the suction phase can be observed; the region of the highest velocity begins around x/B = 10 (left side) and 18 (right side) at the extrusion phase and around x/B = 18 (left side) and 23 (right side) at the suction phase.

Similarly, as with the CJ, the measurement in the x-y planes across the slot can reveal the SJ structure in more detail. To allow the comparison with the CJ, the same planes were chosen: z/B = -41.7 (z = -15 mm, Fig. 5.22) and 0 (z = 0, Fig. 5.23). In the SJ case, these locations correspond to the positions of the maximum velocity near the span end (z/B = -41.7) and the position of the central local maximum of the velocity at z/B = 0. Note that the additional measurements were made in planes of z/B = -27.8, -13.9 and the complete results (velocity and vorticity maps) are shown in Appendix II.

The representative results in Figs. 5.22 and 5.23 show the velocity vector fields at 8 phases of the period colored with the velocity magnitude $U_{x\text{-}y}$ and with the vorticity ω_z, respectively. In Fig. 5.22 the formation and evolution of the vortex pairs can be observed. For φ = 0º to 90º, the existence of three separate vortex pairs is clearly visible. The three-separate local velocity and vorticity maxima at the axis are marked in Fig. 5.22 at φ = 0º by the a, b, c arrows. On the other hand, from φ = 135º only two vortex pairs can be distinguished, i.e., the a and b arrows in Fig. 5.22 at φ = 135º. Obviously, the most downstream vortex pair loses its coherence and breaks down and merges with the previous pairs around the location x/B = 15. Moreover, the initially quite narrow symmetrical jet widens suddenly from $x/B \geq 15$. The more downstream the jet is, the more highly non-symmetrical it becomes. The prevailing part of the jet is deflected to the left and only the minor part continues straight up. The deflection of the jet part to the left is accompanied by the creation of the opposite sign of the vorticity in the jet's inner part, as is visible in Fig. 5.22 e.g., at φ = 180º and x/B = 15, where the jet stream tends to split into two separate parts. Further downstream, at x/B = 40–50, the jet becomes symmetrical again as the deflected part gradually disappears. The position where the jet width

increases, reasonably corresponds to the initialization of the break-up. This observation is in accordance with previous findings by Amitay and Cannelle [62].

In Fig. 5.23 the formation and evolution of the vortex pair at $z = 0$ can be seen in a similar way as in Fig. 5.22. The location of the breaking up of the vortex pair is slightly shifted more downstream, approximately at x/B = 15–20. The position of the break up agrees well with the corresponding visualization from Fig. 5.16. Also, the shift agrees with the visualization experiments. The deformation of the row of the vortex pair was observed (see Fig. 5.17). Except the obviously lower maximum velocity, the shape of the jet differs from that at z/B = -41.7 (Fig. 5.22). The jet is initially symmetrical and increases its width gradually from approximately $x/B = 8$. After the break-up of the coherent vortex structures the jet become non-symmetrical, and it is split into two streams; the prevailing amount of the fluid continues straightly downstream and the minor part of the jet is deflected to the left. Note a distinguishable difference from the jet splitting at z/B = -41.7 in Fig. 5.22:

- At z/B = -41.7 (Fig. 5.22), the major SJ part is deflected to the left-hand side.
- At $z/B = 0$ (Fig. 5.23), the major SJ part continues straightly downstream.

The measurement at $z/B = 0$ confirms the visualization of Fig. 5.16, where the weaker side of the flow can be observed in the left part of the jet from approximately $x/B \geq 18$. Obviously, this behavior indicates a process of 3D jet formation. Analogously to the CJ, based on the vector maps, Fig. 5.22 and 5.23 show that the present SJ cannot be considered as a 2D jet: the structure of the jet differs along the span and the strong 3D features (such as asymmetry and deflection from its initial direction) can be identified at every examined plane.

A smaller field of view seen during measurements across the plane (in comparison with the measurement along the span) allows the resolution of the measured velocity field to increase and thus to capture what happens near the nozzle exit. Thus, a fluid suction from the nozzle vicinity can be observed in both Figs. 5.22 and 5.23. The result near the nozzle exit and near the solid surfaces in general, are contaminated with high uncertainty (see section 3.2). The results can nevertheless provide qualitative information. To emphasize the differences between the suction and extrusion parts, the pictures in Figs. 5.22 and 5.23, showing the maximum extrusion and suction ($\varphi = 90°$ and 270°, respectively), were enlarged and are shown in Figs. 5.24 and 5.25, respectively. Moreover, the streamlines were evaluated and added into the pictures.

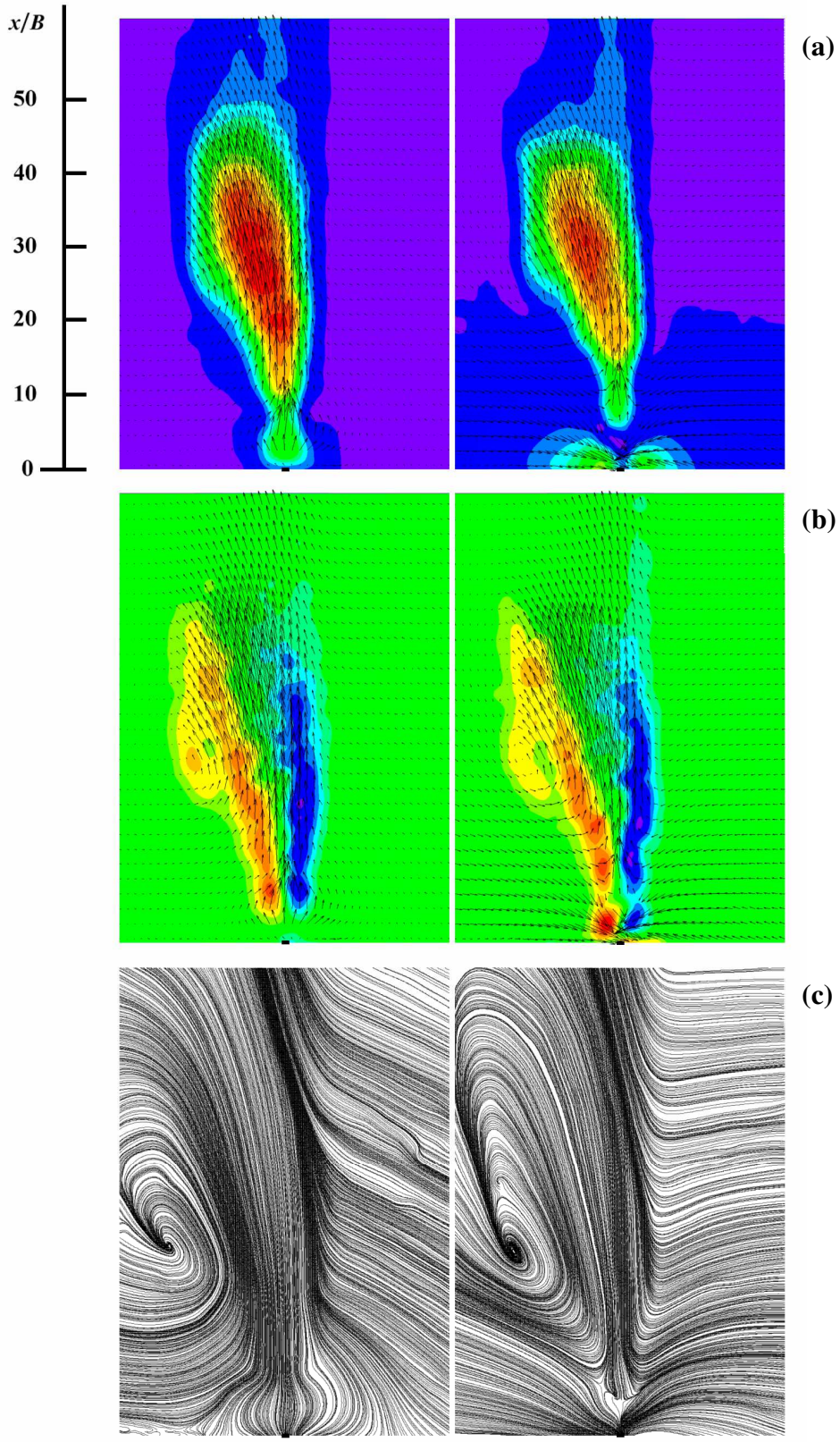

Fig. 5.24 Velocity vector field of the SJ across the slot (*x*-*y* plane) at $z/B = -41.7$ and $\varphi = 90°$ (left) and 270° (right) colored by
(a) Velocity magnitude, (b) Vorticity and (c) Corresponding streamlines
(the velocity and vorticity scale is the same as in Fig. 5.19 and 5.20, respectively).

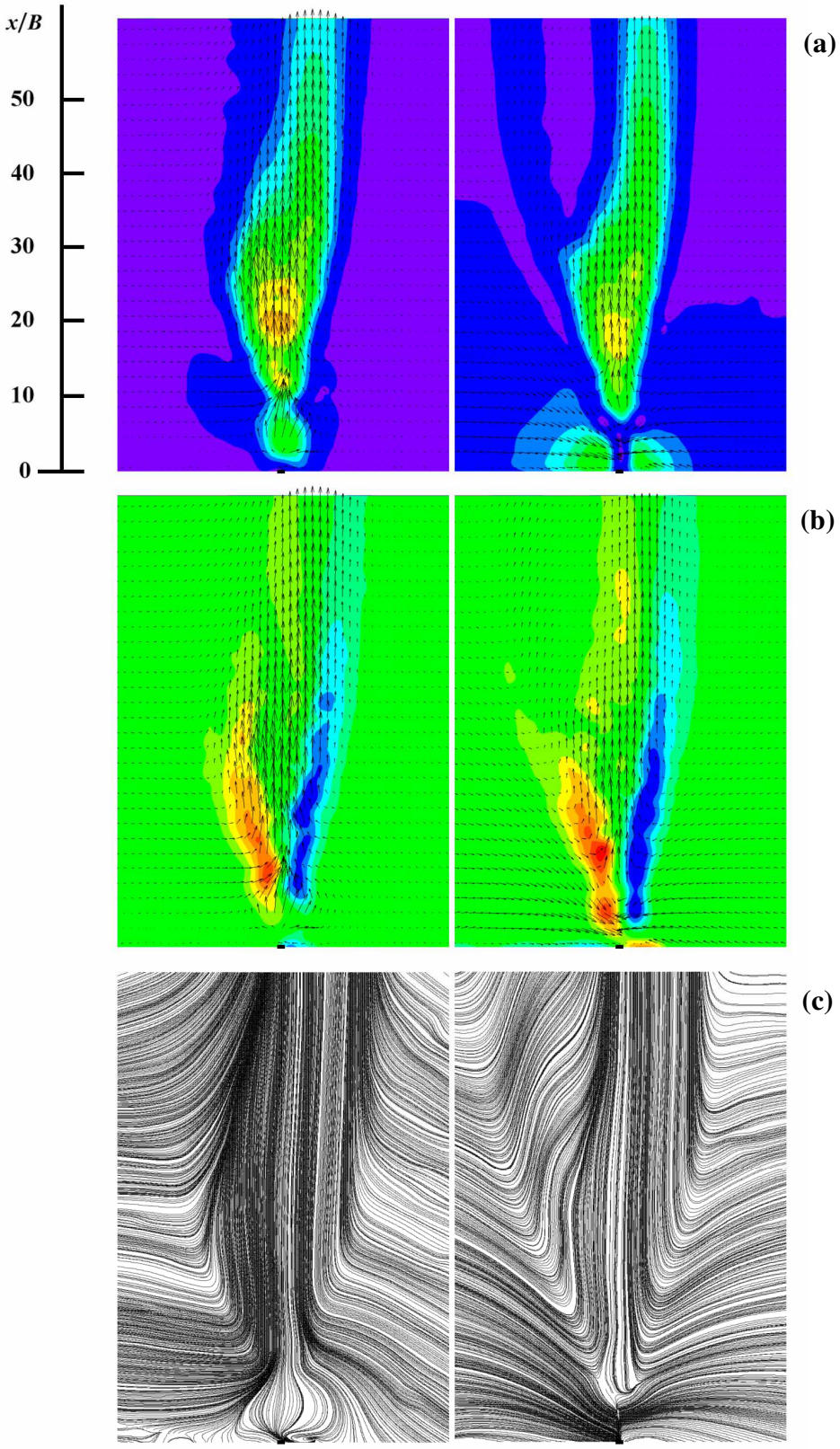

Fig. 5.25 Velocity vector field of the SJ across the slot (*x*-*y* plane) at $z/B = 0$ and $\varphi = 90°$ (left) and 270° (right) colored by
(a) Velocity magnitude, (b) Vorticity and (c) Corresponding streamlines
(the velocity and vorticity scale is the same as in Fig. 5.19 and 5.20, respectively).

At both distances, z/B= -15 and 0, Figs. 5.24 and 5.25 demonstrate similar SJ features. During the blowing stroke, the vortex pair is formed and the fluid is directed downstream. The vorticity concentration near the nozzle exit is negligible. Conversely, at the suction stroke, the fluid is sucked inside the cavity and the direction of the fluid motion is reversed in the immediate vicinity of the actuator. During this process, the vortex pair, with reversed direction, is formed and sucked. This is visible as a region of a vorticity concentration with an inverse direction in the very near vicinity of the nozzle. It is interesting to note that the non-symmetrical geometry (actuator cavity and external surface, see Fig. 2.1) causes a non-symmetrical flow field in the near field affected by the suction.

During the suction stroke, the stagnation point (sometimes called the saddle-point) is formed on the jet axis (see e.g., [40]). It represents the boundary between the region affected by the suction and the region not affected by suction. In other words, it shows the maximum reach of the suction area on the jet's centerline. The position of the saddle-point is commensurate in both cases. The reach of the suction is subtly higher at z/B = 0, around x/B = 7 against x/B = 5 at z/B = -41.7. Moreover, the difference between the entrainment of the surrounding water into the jet during the suction and extrusion parts of the cycle can be seen from the streamline map (both in Figs. 5.24 and 5.25).

The near field process of suction has a minor influence on the far-field. The streamlines also confirm the strong 3D nature of the present SJ; the jet near the nozzle edge (Fig. 5.24) is influenced by the end-effects and huge vortex structure is formed on the left and thus the jet is deflected, conversely, the flow-field in the middle of the slot is rather regular with no large-vortex formation.

Contours of the streamwise velocity components are presented in Figs. 5.26(a and b) at maximum blowing and suction for φ = 90° and 270°, respectively. The pictures were created in the same way as in the CJ case (cf. Fig. 5.5), i.e., they were constructed from the measurements across the slot and the zero velocity values were artificially added to z/B = -69.4 (z = -25 mm) and z/B = 69.4 (z = 25 mm). The same contour plots are transformed into 3D versions and are shown in the subsequent Figs. 5.27 (a and b). Two main velocity maxima appear near the span end and the central local maximum is apparent at z/B = 0 (for both phases of the cycle). While the peaks of the main maxima are located on the z-axis for every observed distance from the nozzle exit, the central local maximum moves slightly towards an off-axis position. Moreover, the central peak gradually diminishes as the pair of maxima move towards each other. There are no significant differences between the extrusion

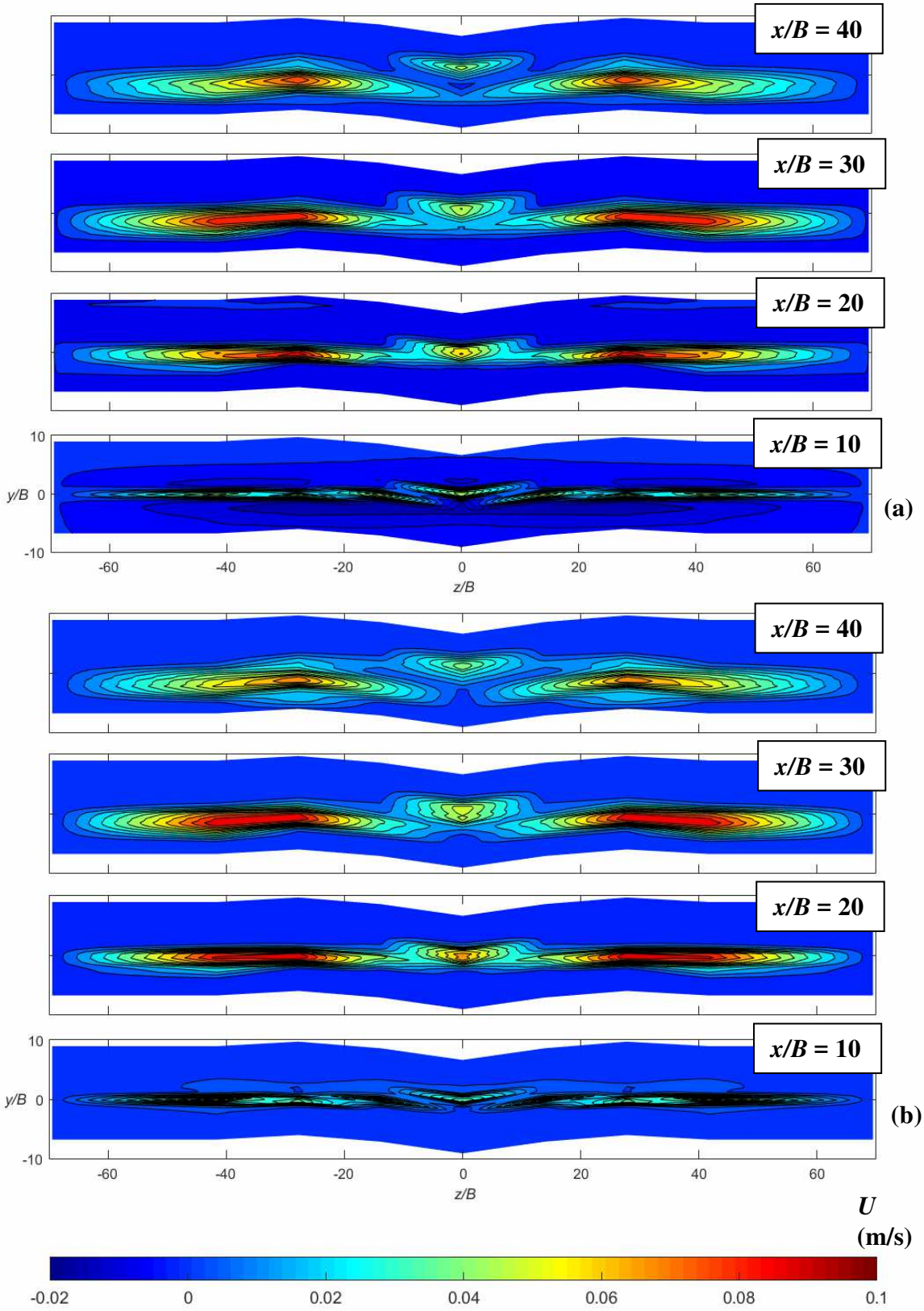

Fig. 5.26 Contours of the streamwise velocity component of the SJ at
(a) $\varphi = 90°$
(b) $\varphi = 270°$.

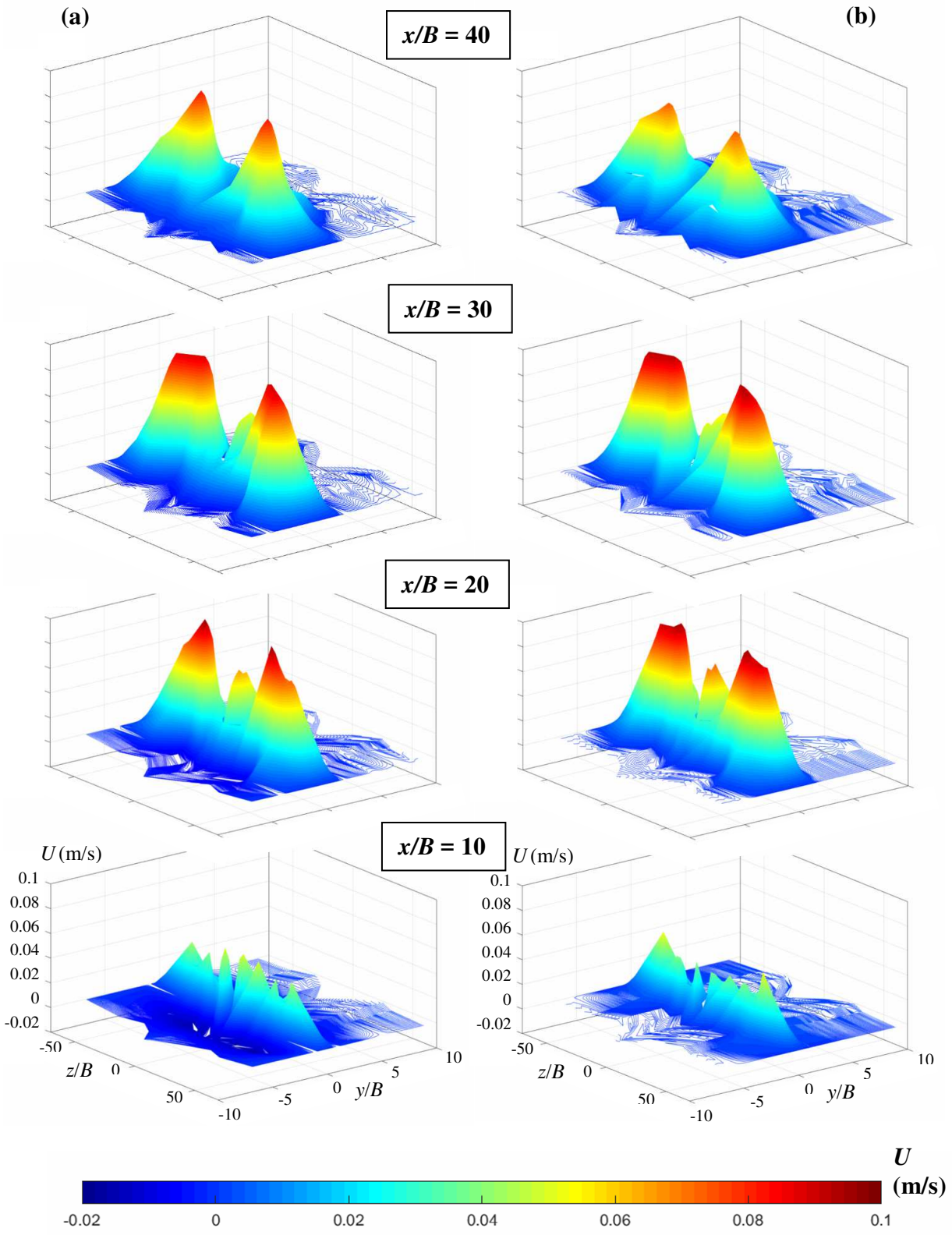

Fig. 5.27 3D contours of the streamwise velocity component of the SJ at
(a) $\varphi = 90°$
(b) $\varphi = 270°$.

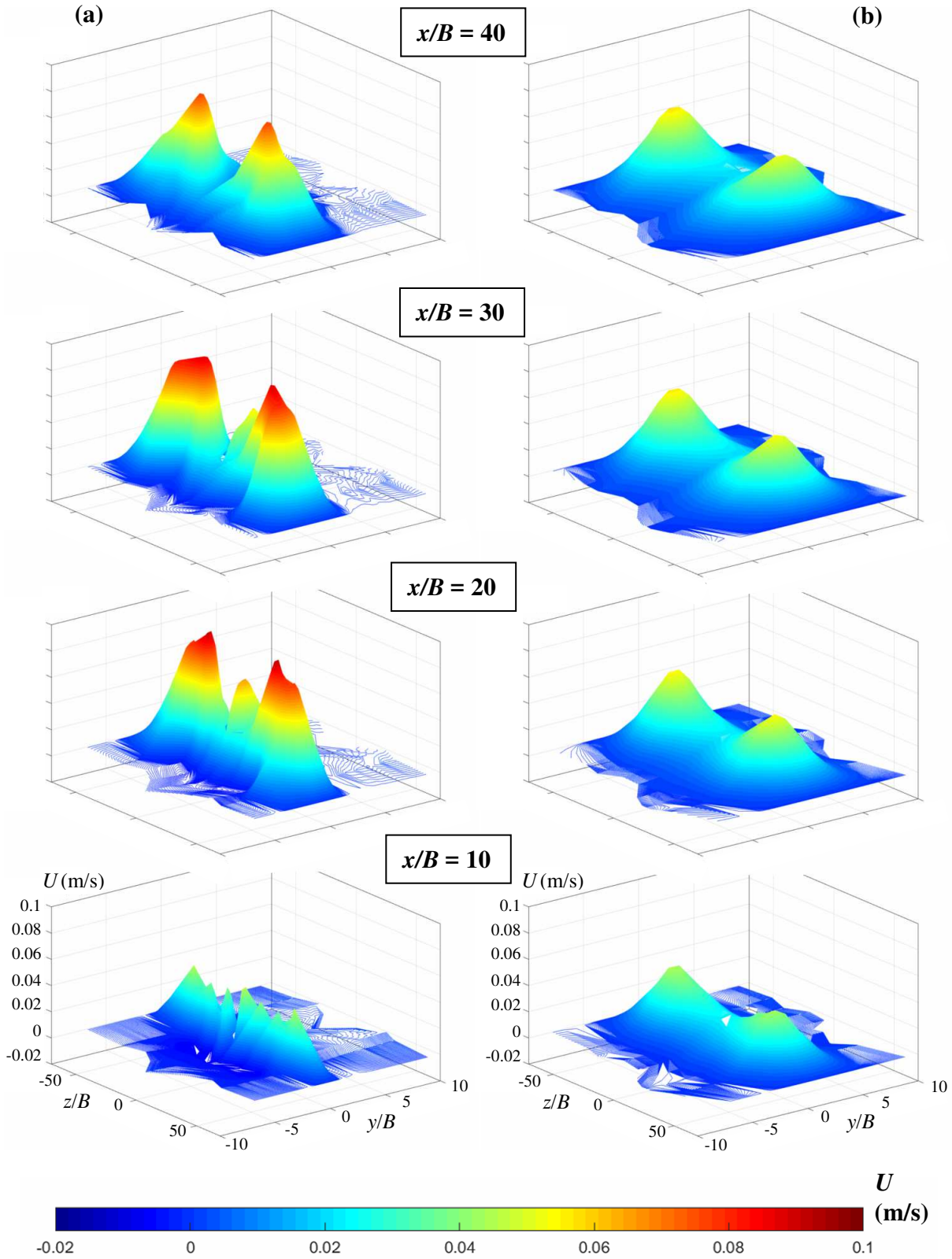

Fig. 5.28 3D contours of the time-mean streamwise velocity component
(a) SJ
(b) CJ.

and suction part of the period. The only variations that can be identified are in $x/B = 10$, where the position of the maximum along the span is visible around the mid-part of the slot during the extrusion and then it moves towards both edges of the slot during the suction phase.

The time-mean velocity profiles were calculated from the measured phase-locked velocity profiles and the 3D contours map of the time-mean streamwise velocity components are shown in Fig. 5.28(a). For comparison purposes, the 3D-contour graphs of the CJ are plotted in Fig. 5.28(b) as well (the CJ graph was replotted from data of Fig. 5.6). Both jets are strongly influenced by near-end effects and the existence of the pair of off-axis peaks is evident. The formation of the peaks is faster in the CJ case. There are peaks that are already formed at $x/B = 10$, while a series of several smaller peaks can be observed for SJ. The existence of the row of small peaks of the SJ at $x/B = 10$ is related to "streaky-like" structures that are finer, not organized in the near-field and become well-organized further downstream (see Fig. 1.3 and [62]). The "streaky-like" character of the SJ also initializes the formation of the middle peak, which is not present for CJ. However, with the increasing distance from the nozzle exit, the end effects begin to dominate, the middle peak is shifted along the y-axis and gradually diminishes. The position of the peaks remains almost unchanged in the CJ case (around $z/B = \pm 40$) but varies with distance in the SJ case (from $z/B = \pm 25$ to ± 35). The change of the position is not monotonic; however, the peaks are always placed symmetrically. The unsteady character of SJ along with a "streaky-like" structure causes a less symmetrical, less "smooth" and less organized velocity field in SJ compared to CJ.

The time-mean, streamwise and cross-stream velocity components across the slot at $z/B = 0$ are shown in Figs. 5.29(a and b), respectively. The jet is tolerably symmetrical up to $x/B = 20$. Further on, the deformation of the jet is apparent (see streamwise velocity component, Fig. 5.29(a)), as observed in the contour plots (Fig. 5.26 and 5.27). Unlike CJs, the cross-stream velocity component of the SJ case plays an important role, not only during the suction itself but even from the time-mean point-of-view, especially in the near field, which is shown in Fig. 5.29(b). At $x/B = 10$ the order of magnitude of the cross-stream component is commensurate with the magnitude of the streamwise component. Furthermore, the cross-stream velocity weakens and its order of magnitude is much smaller in comparison with the streamwise velocity.

The present time-mean results and experimental data is compared to data from the experiments of other authors, specifically the streamwise velocity profiles by Gillespie et al. [53] (Fig. 5.30(a)) and the streamwise velocity profiles by Amitay and Cannelle [62] (Fig.

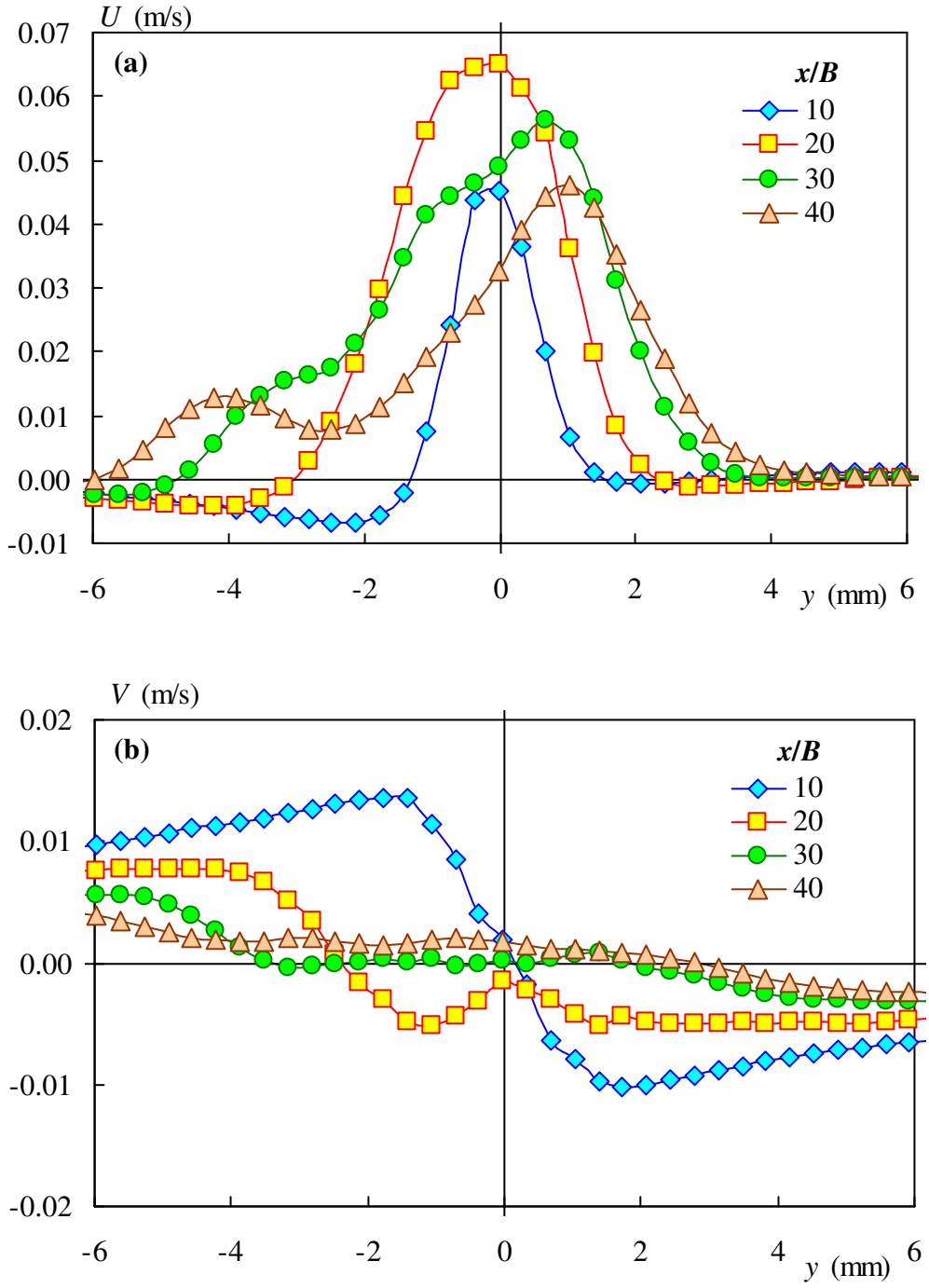

Fig. 5.29 Velocity profiles of the SJ
(a) Stream-wise velocity component,
(b) Cross-stream velocity component.

5.30(b)). The present profiles were recalculated into a dimensionless form so that they agree with the original coordinates of the comparable research (i.e., the vertical axis is either U/U_{max} or U/U_0) and the new horizontal coordinate y^* is used (in the same way as in the CJ case).

Fig. 5.30(a) shows that the present data are in excellent agreement with the data by Gillespie et al. [53] in the very near field (x/B = 10), however the profiles differ in the far field; The

profiles by Gillespie et al. [53] are symmetrical and much wider. The reason for the former feature is the geometry of the nozzle (a symmetrical exit channel was used by Gillespie et al. [53]). The reason for the latter feature is that the jet by Gillespie et al. [53] undergoes axis-switching, which leads to a considerable increase in the width of the jet in the lateral direction. Axis-switching does not occur in the present jet and so the jet remains rather narrow (the topic of the jet width will also be discussed later).

A different point-of-view of the results gives a comparison of the profiles, which are related

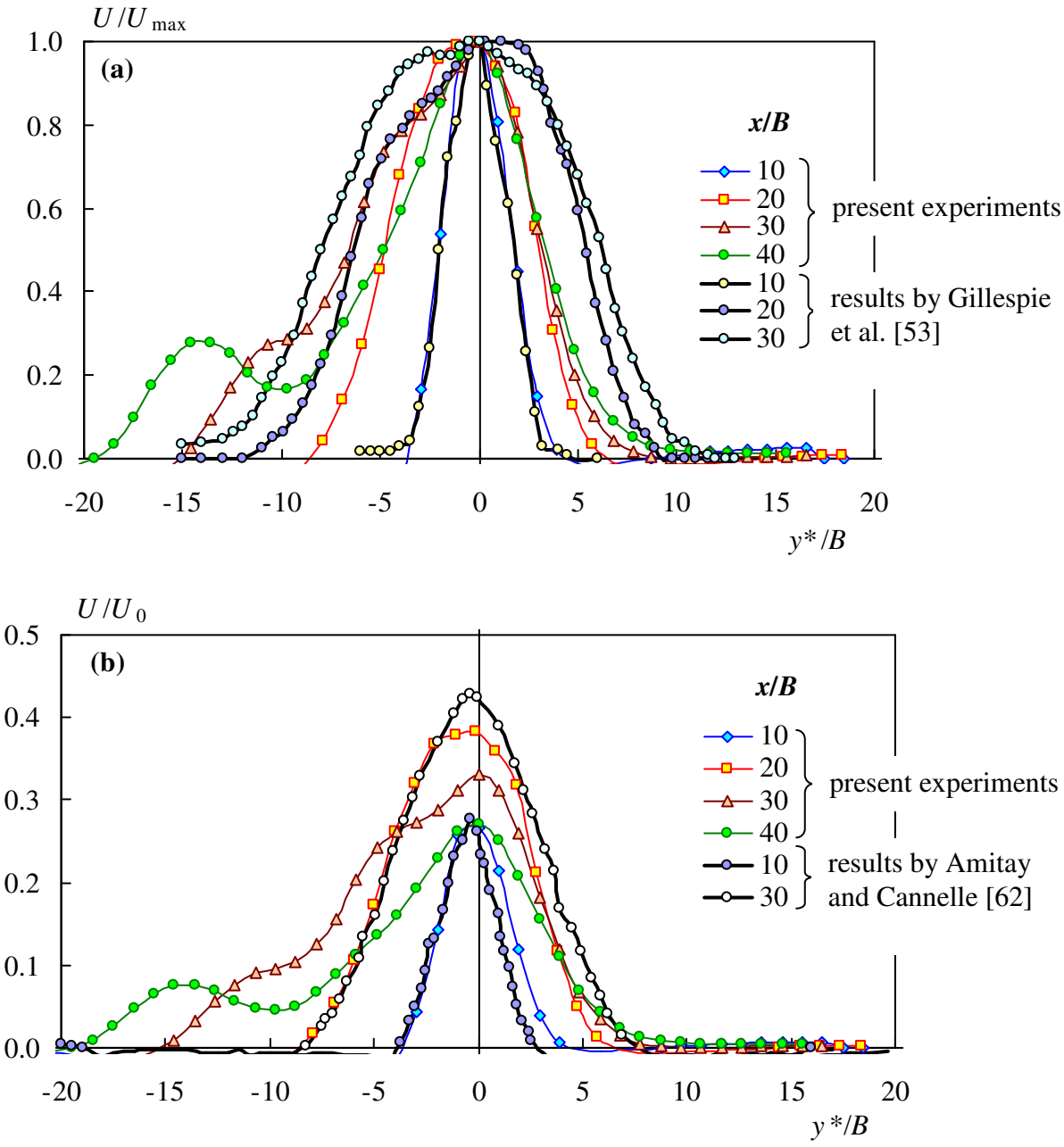

Fig. 5.30 Dimensionless streamwise velocity component of the SJ normalized by
(a) Maximum (axial) velocity $U_{max,}$
(b) Time-mean exit velocity U_0.

to the time-mean exit velocity U_0 in Fig. 5.30(b). Again, the profile at $x/B = 10$ agrees with the data by Amitay and Cannelle [62]. At further distances, the jet changes its character and becomes non-symmetrical, while the jet by Amitay and Cannelle [62] remains symmetrical. Moreover, the maximum centerline value of the ratio U/U_0 is considerable lower in the present case (by approximately 23%). The reason is the deformation of the jet and redistribution of the fluid on the wider cross-section of the jet, which leads to a large drop in the centerline velocity (as will be discussed later).

Finally, the streamwise velocity profiles in the lateral direction were transformed into the dimensionless form, using the half-width of the jet (Fig. 5.31). Because of the asymmetry of the profiles, the average values from the left and right part of the profiles were used. The profiles collapse onto one curve and are self-similar, which agrees well with the referenced theoretical solutions by Blevins [3] and Bickley [8]. The bigger differences are in the regions with low velocities where the strong asymmetry in the origin profiles occurs (see Fig. 5.29).

The evolution of the half-width along the x-axis presents Fig. 5.32(a) and in detail Fig. 5.32(b). For comparison purposes, the data by Smith and Glezer [29], Gillespie et al. [53], Sato and Sakao [22] and the theoretical prediction for the CJ by Blevins [3] are also plotted in Fig. 5.32. The trend of the present curves is not monotonic. At $x/B = 10$, the width of the jet is commensurate with the span. Further downstream, the half-width of the jet near the end ($z/B =$ -41.7) differs significantly. The near-end effects, which result in the distinct

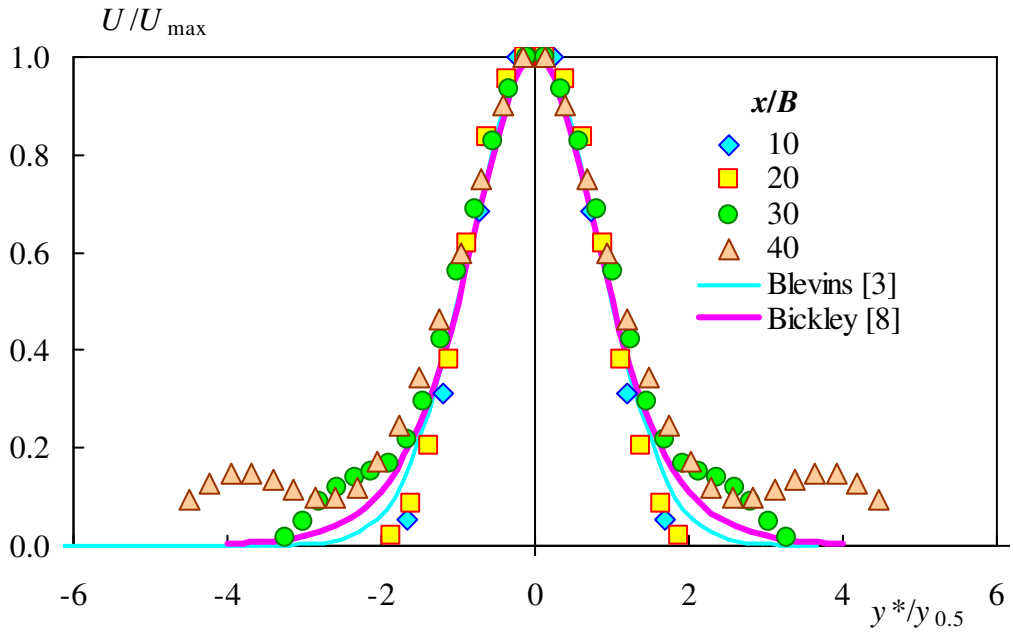

Fig. 5.31 Dimensionless streamwise velocity component of the SJ.

deformation of our jet, and the non-monotonic level of the entrainment from the surroundings cause the difference (see consequent Fig. 5.34). Interestingly, the comparison with the other data show the values of the half-width approximately agree with the solution for the CJ by Blevins [3] and with the results by Sato and Sakao [22] for CJs at lower Reynolds number ($Re = 28$). On the other hand, the increase of the half-width of the SJ by Smith and Glezer [29] and Gillespie et al. [53] agrees with the present results only in the near field, around $x/B = 10$; further downstream the behavior is completely different. Moreover, the compared results differ from one another as well. The slope of the curve by Smith and Glezer [29] is constant and much steeper than in the present case. On the contrary, the evolution of the half-width of the jet from Gillespie et al. [53] can be divided into three regions: the initial region ($x/B < 8$), where the slope of the curve agrees with the present one, the transition region ($8 < x/B < 16$), where the increase of the width is faster, and the developed region ($x/B > 16$), where the slope by Gillespie et al. [53] agrees with the curve by Smith and Glezer [29]. The non-monotonic behavior, and the sudden increase of the width, is caused by the presence of axis-switching, which occurs around $x/B = 15$. The process of axis-switching was not observed in the present case, nor in the experiment by Smith and Glezer [29].

Useful information can be obtained by a comparing the half-widths of the SJ and the CJ in Fig. 5.33. The width of the SJ is slightly higher than that of the CJ, especially in the near field, further downstream the width decreases, while the width of the CJ increases continuously. In the far-field, the widths of both jets are commensurate. The one exception is the width of the SJ at $z/B = -41.7$ which is at first lower; further downstream ($x/B = 30$–40) it is twice higher than that of the CJ at corresponding plane. However, this effect diminishes for $x/B = 50$ and the half-widths of the SJ and CJ are comparable. The reasons are the 3D end-effects which are promoted by the non-steady character of the SJ. Although the SJ is "wider", i.e., it affects a larger area in the space, the jet can be considered self-similar (see Fig. 5.31) and commensurate with the conventional CJ.

The evolution of the volume flow rate is shown in Fig. 5.34. The most intensive entrainment was identified near the end plane ($z/B = -41.7$) where the flow rate rises sharply to $x/B = 30$ and then falls equally sharply down. Qualitatively similar trend (sharp increase and then sharp decrease), though at a lower level, can be seen for $z/B = 0$. Conversely, the lowest flow rate was observed at $z/B = -13.9$. The abrupt changes of the flow rate are caused by the 3D effects of the flow, i.e., the fluid moves quickly and suddenly from one plane to another. The great difference between the SJ and the CJ is obvious from Fig. 5.35, where the volume flow rates

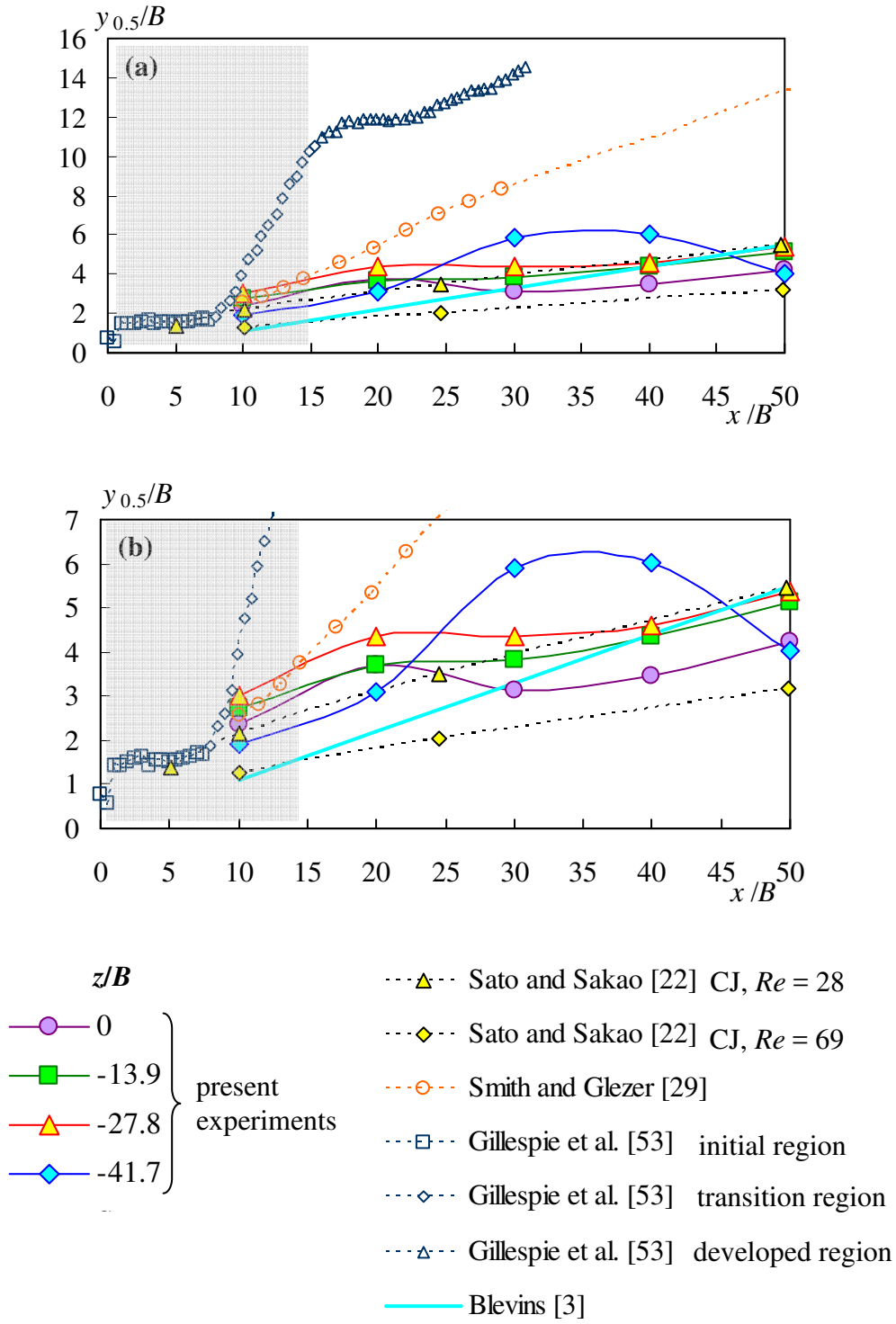

Fig. 5.32 Evolution of the half-width of the SJ
(a) Entire plot,
(b) Detail view.

of both jets were transformed into dimensionless form using the calculated volume flow rate in the nozzle's exit Q_{z0}, where $Q_{z0} = Q_z(z=0)$. While the shape of the curves for CJ is rather

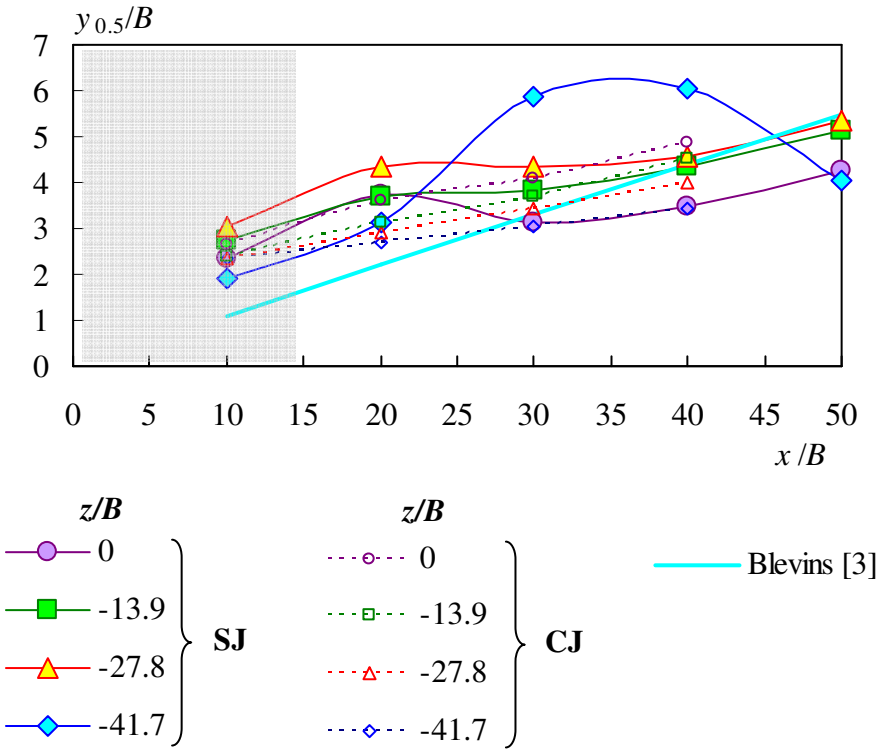

Fig. 5.33 Evolution of the half-width - a comparison of the SJ and CJ.

monotonic, and the values are lower than the theoretical prediction by Blevins [3] for 2D jet, the slope of the curves of the SJ changes rapidly with the distance. Between x/B = 20 and 30, the values are higher than for the CJ and higher than the Blevins curve than drop quickly below the value Q_z/Q_{z0} = 2 (except for the plane x/B = -27.8, where the slope corresponds to the one by Blevins [3]).

The evolution of the time-mean streamwise velocity component of the SJ along the jet axis is shown in Fig. 5.36. Due to the considerable deflection of the jet from its initial vertical direction, the new coordinate x^* was chosen to follow the individual deflection of the jet at every position along the span. For comparison purposes, the curves for the CJ (from Fig. 5.11) are also plotted in Fig. 5.36 (for the CJ, $x = x^*$). Similarly as in the CJ case, the velocity values differ with the position along the span, however, the differences in the SJ case are not as large as for the CJ. The lowest values exhibit the position z/B = -13.9. This agrees with the previous observation from e.g., Fig. 5.27. The time-mean SJ velocity profiles are affected by the suction phase in the nearfield and by the considerable 3D character of the jet. Unlike the CJ case, the steep decay appears in the SJ velocity curves around x^*/B = 40. These abrupt

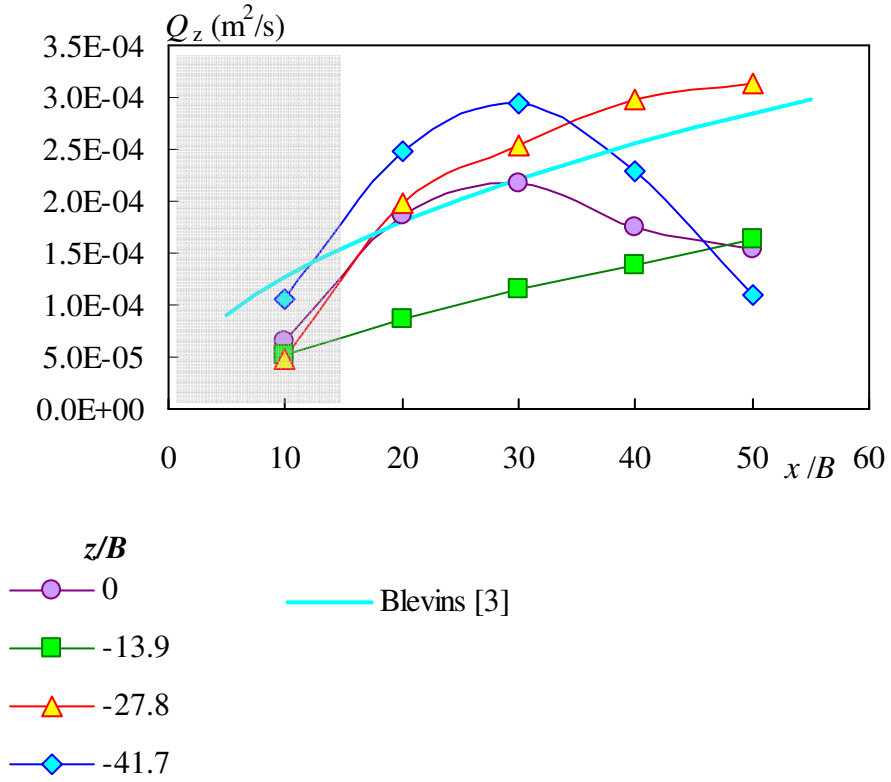

Fig. 5.34 Evolution of the volume flow rate of the SJ.

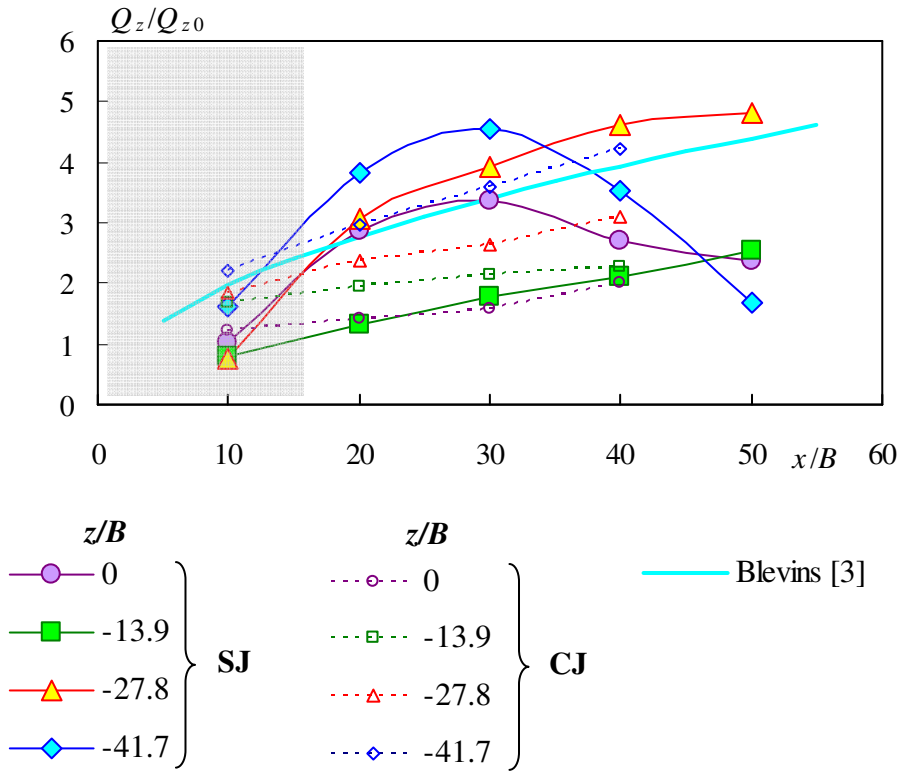

Fig. 5.35 Evolution of the volume flow rate - a comparison of the SJ and CJ.

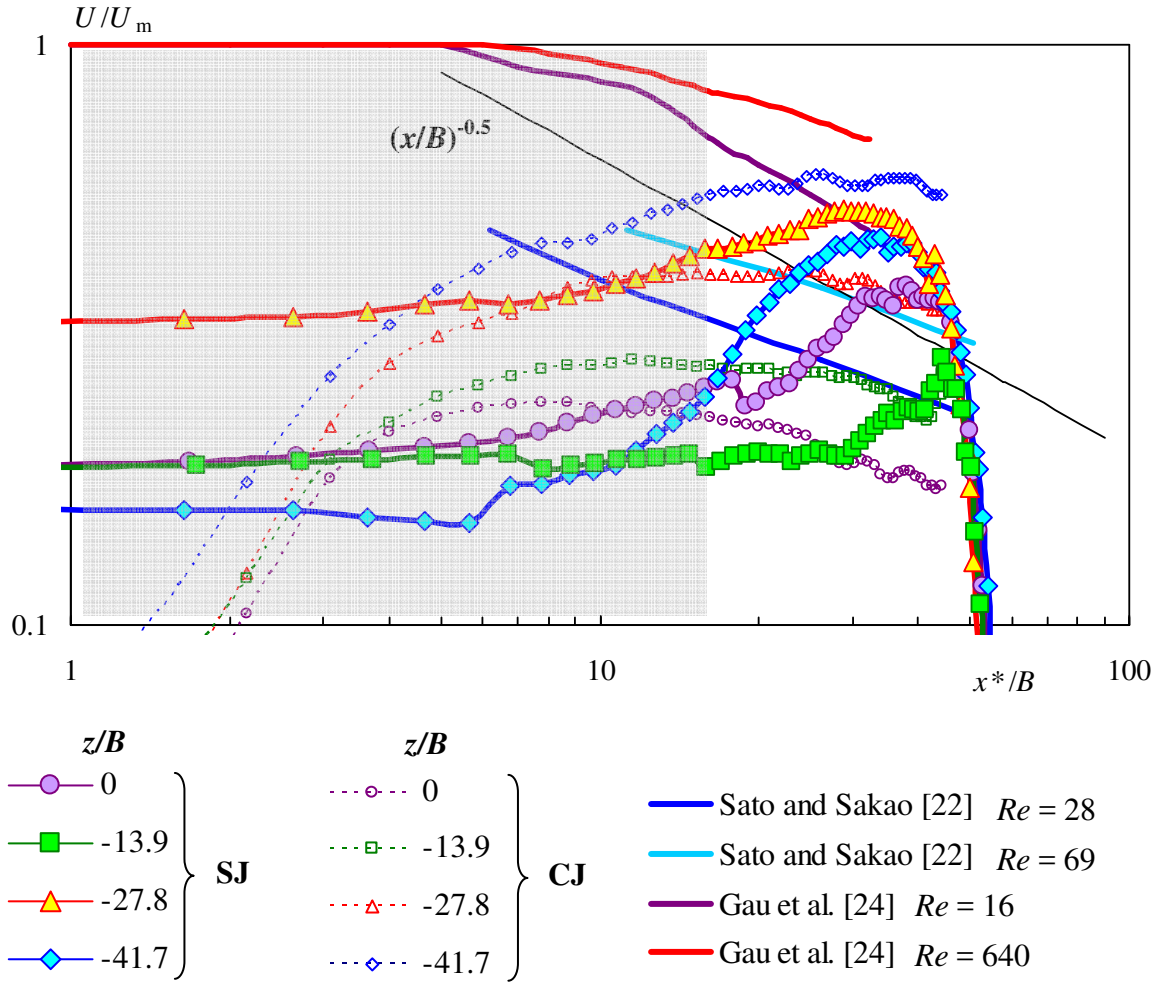

Fig. 5.36 Evolution of the time-mean streamwise centerline velocity of the SJ and the comparison with CJ.

changes do not correspond either to the present CJ microjet, or the results by another author (Sato and Sakao [22], Gau et al. [24]) which are also shown in Fig. 5.36. It is obvious that the sudden decrease in the curves relates to the break-up of the jet (visible e.g., in Fig. 5.16) and this indicates rather massive mixing with the jet's surroundings. The results confirm that the character of the present SJ is strongly 3D.

5.3 The jet impinging onto the cylinder

The previous chapters were focused solely on the jets (CJ and SJ) without the cylinder. In the next step, the cylinder was placed downstream of the nozzle (see Fig. 2.3) and the basic characteristics of the flow-field with obstacle were investigated. The preliminary results have been published recently [133,134].

In Table 5, the experimental settings for both CJ and SJ are summarized (the settings for the CJ corresponds to the values shown in Table 4, the SJ is the nominal case).

Table 5 Parameters of the experiments - CJ and SJ impinging onto the cylinder

	Q l/min	f Hz	P_{SJ} mW	U m/s	U_0 m/s	Re_{CJ}	Re_{SJ}	$Re_{CJ,D}$	$Re_{SJ,D}$	Re_{Dc}
CJ	0.090			0.10		40		135		102
	0.177			0.20		79		267		203
	0.357			0.41		161		542		412
SJ		46	17		0.18		67		225	171

As the initial step, the selected cases were visualized using the LIF technique. The resulting visualizations of the CJs and SJs are shown in Fig. 5.37 and 5.38, respectively. The actuator slot is on the bottom margin of the images, and the orifice-to-cylinder spacing was adjusted as $H = 20.8\ B$. For the sake of readability, the cylinder axis is plotted using a dash-and-dot line, and the cylinder cross-section in the laser sheet plane is plotted using light circles.

Based on the flow visualization results shown in Figs. 5.37 and 5.38, three main effects can be distinguished: the Reynolds number effect, the thermal effect, and the effect of the nature of the jet (CJ vs. SJ).

• The Reynolds number effect is demonstrated via a comparison of Figs. 5.37(a) and 5.37(b). Both jets are identical in character (CJs) and identical in thermal conditions (unheated, i.e., $T_w = T_\infty$.). The Reynolds number is increased from $Re_{CJ} = 40$ (i.e., $Re_D = 135$, Fig. 5.37(a)) to $Re_{CJ} = 161$ (i.e., $Re_D = 542$, Fig. 5.37(b)). Fig. 5.37(a) shows the CJ impinging on the cylinder. From the stagnation zone, the jet is divided into two halves. A flow separation occurs very soon on the windward cylinder side. Finally, the flow leaves the cylinder in two halves, forming a Y-shaped pattern. The flow around the leeward cylinder side is weak (not visible in Fig. 5.37(a)), which indicates a highly probable decrease in the overall heat transfer rate (it will be quantified in the text below). Probable reasons are effects of the mini scale and the low Reynolds numbers. Conversely, the flow pattern is different for greater Re_D values, as shown in Fig. 5.37(b). Unlike Fig. 5.37(a), the flow around the leeward cylinder side exists in Fig. 5.37(b). The flow pattern resembles a vortex-shedding wake known for cylinders in a cross-flow.

• The thermal effect is demonstrated via a comparison of Figs. 5.38(a) and 5.38(b). Again, for comparison purposes, both jets are identical in character (SJs) and the $Re_{SJ} = 67$ is identical as well. Only the thermal conditions are changed: while Fig. 5.38(a) shows the

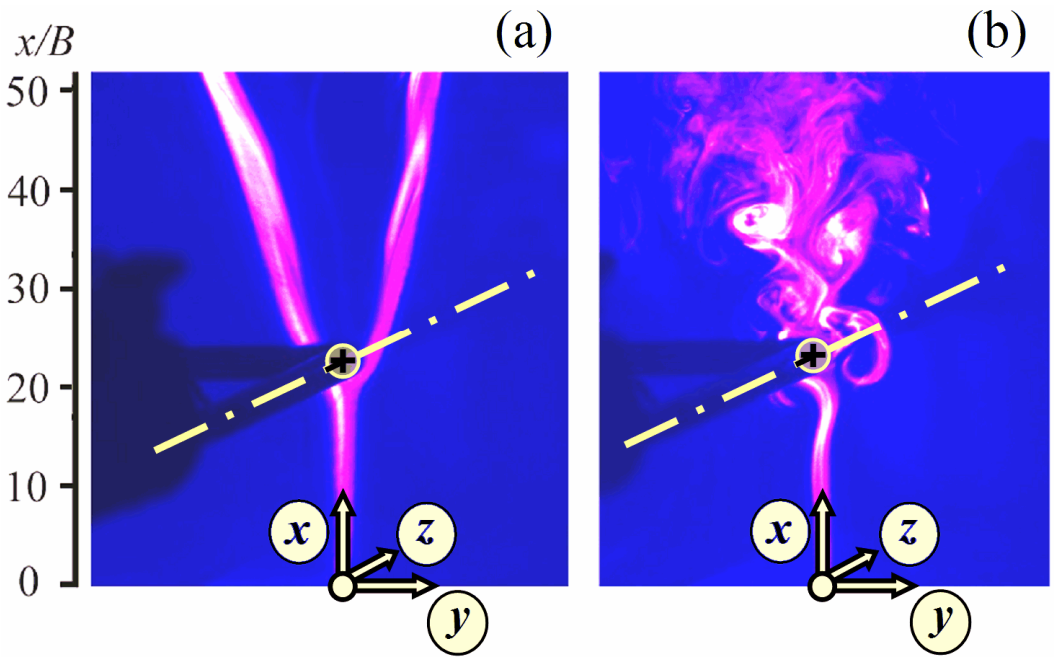

Fig. 5.37 LIF visualization of the CJs, unheated cases at $T_w = T_\infty$ and H/B = 20.8 for
(a) Re_{CJ} = 40 (i.e., $Re_{CJ,D}$ = 135),
(b) Re_{CJ} = 161 (i.e., $Re_{CJ,D}$ = 542).

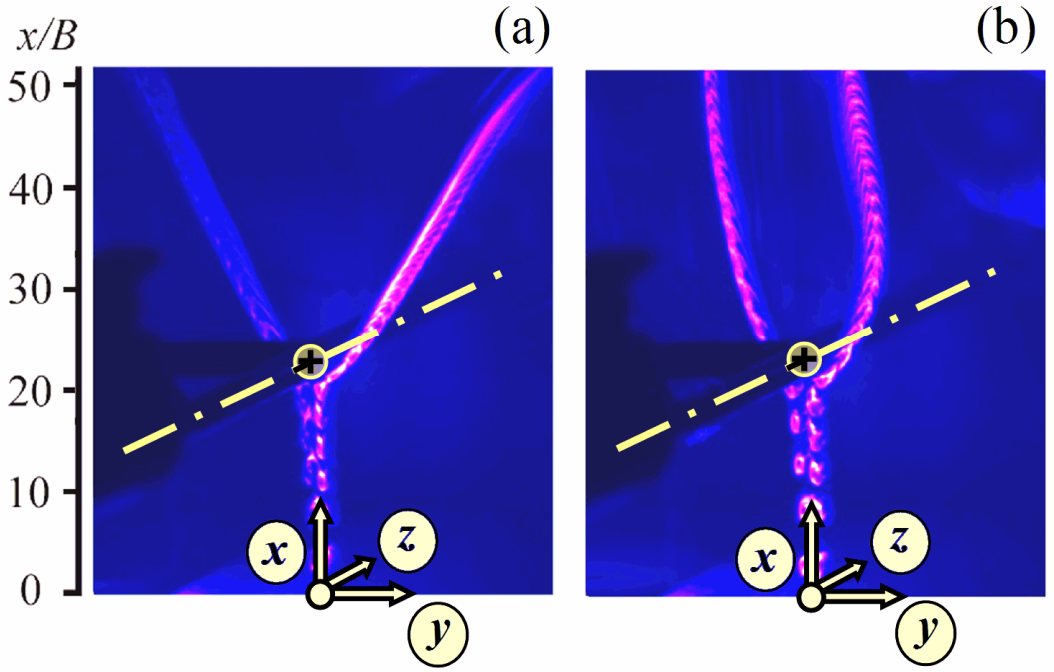

Fig. 5.38 LIF visualization of the SJs, Re_{SJ} = 67, H/B = 20.8
(a) Unheated case,
(b) Heated case at T_w = 28.4°C and T_∞ = 22.8°C.

unheated cylinder case, the heated cylinder case is shown in Fig. 5.38(b) and has the temperatures T_w = 28.4°C and T_∞ = 22.8°C. For both cases, the SJ impinges on the cylinder surface and is divided into two halves. A flow separation occurs very soon on the

windward cylinder side and the flow leaves the cylinder in two halves, forming a Y-shaped pattern. The flow around the leeward cylinder side was weak and not visible in both cases (i.e., Figs. 5.38(a) and 5.38(b)). Note some specific features of the heated cylinder case in Fig. 5.38(b). While both branches of the Y-shaped flow leaving the cylinder for the unheated cases in Fig. 5.38(a) are straight and directed nearly tangentially from the cylinder surface, these flow branches from the heated cylinder in Fig. 5.38(b) are curved towards each other. This thermal effect in the far field indicates a thermal plume that is released from the leeward cylinder side where the forced jet flow does not reach. Obviously, the thermal plume is not visible.

• The effect of the jet's nature is demonstrated via a comparison of Figs. 5.37(a) and 5.38(a), respectively. Both unheated cylinder cases are different in terms of the nature of jets: CJ vs. SJ, respectively. Differences in the Reynolds numbers of the jets are not dominant: $Re_{CJ} = 40$ vs. $Re_{SJ} = 67$, respectively. The distinct character of the streaklines clearly indicates both jets: while the smooth streaklines in Fig. 5.37(a) indicate the CJ, a train of vortices (expressed after [269]) in Fig. 5.38(a) is typical for the SJ. However, the dominant features of both cases are qualitatively similar as was described in the text above: the jet impingement and division into two halves, flow separation on the windward cylinder side, and two jet halves leaving the cylinder as the Y-shaped pattern.

Another effect that is clearly manifested in Fig. 5.37(b) is the low-frequency side-to-side motion of the CJ, upstream of the front stagnation line. Based on the observations, the frequency of these self-sustained oscillations was estimated to be approximately 1–2 Hz. Note that the vortex shedding frequency of a cylinder in cross flow under similar conditions can be expected to be approximately 10 times higher (cf. Williamson [135]). Therefore, the mechanism of the observed sweeping-jet effect seems to be different from the vortex shedding. However, a deeper discussion of the effect is beyond the scope of this study (as well as beyond the abilities of the instruments used).

To investigate the flow-field around the cylinder more deeply, PIV measurements were taken. As shown in Figs. 5.37 and 5.38, the CJ and SJ with approximately corresponding *Re* are identical in character. Thus, the more complicated and time-consuming measurement of an SJ flow-field was omitted and only the flow-field of the CJ was investigated. The resulting vector velocity maps, together with the corresponding streamlines, are shown in Fig. 5.39. The pictures from left to right correspond to the CJ cases from the lowest *Re* to the highest one (according to Table 5). The position of the cylinder is depicted by a green circle. The

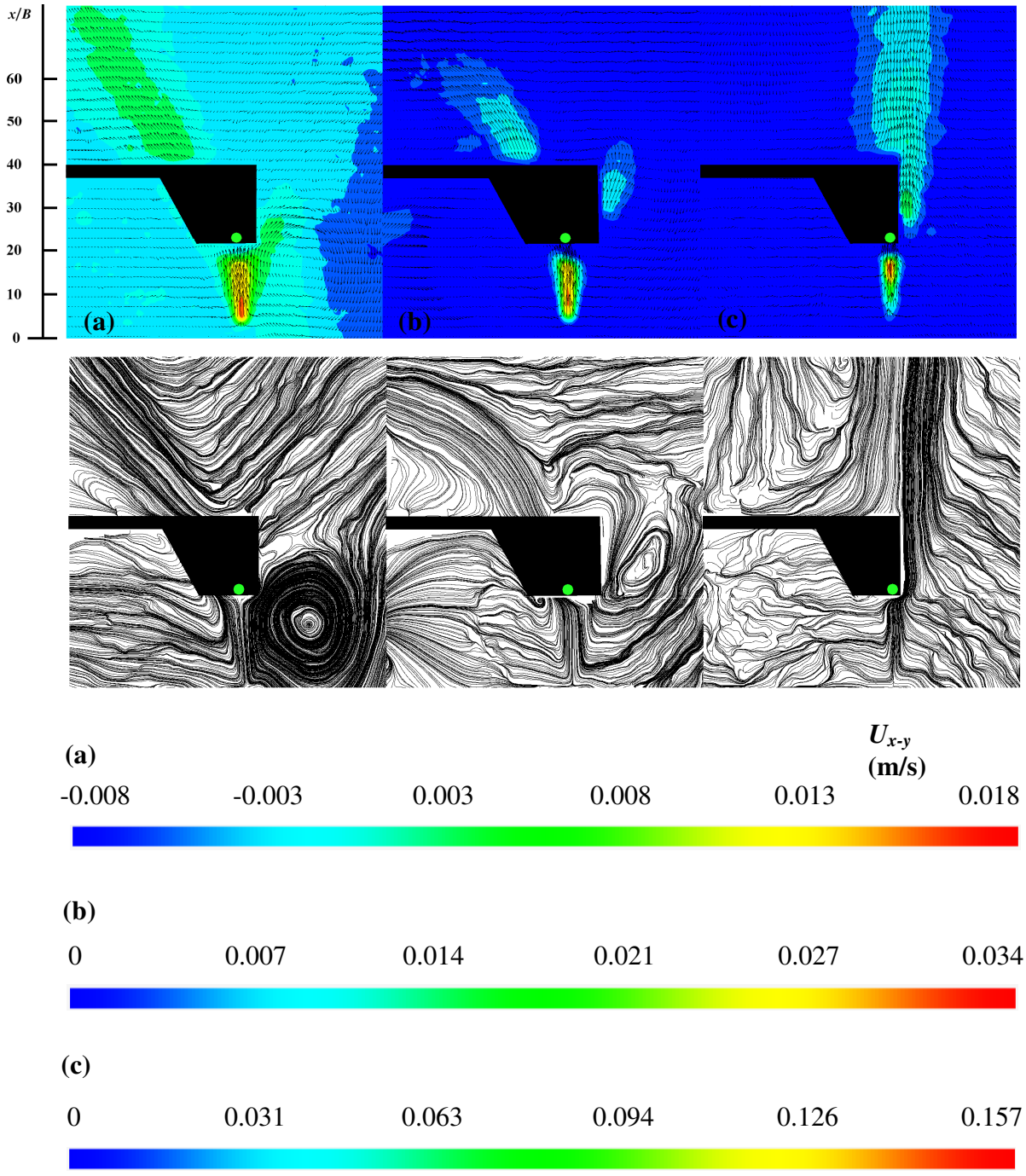

Fig. 5.39 Velocity vector field colored by velocity magnitude and the corresponding streamlines of the CJ impinging onto the cylinder
(a) Re_{CJ} = 40 ($Re_{CJ,D}$ = 135),
(b) Re_{CJ} = 79 ($Re_{CJ,D}$ = 267),
(c) Re_{CJ} = 161 ($Re_{CJ,D}$ = 542).

laser-sheet was placed in the *x-y* plane, i.e., in the middle of the actuator slot. The pictures are created as the average from 100 instantaneous vector maps. The vector maps agree well with the behavior expected from qualitative visualization: The jet with the lowest *Re* = 40 impinges onto the cylinder and splits into two halves creating a Y-shaped pattern (see Fig. 5.37(a) and

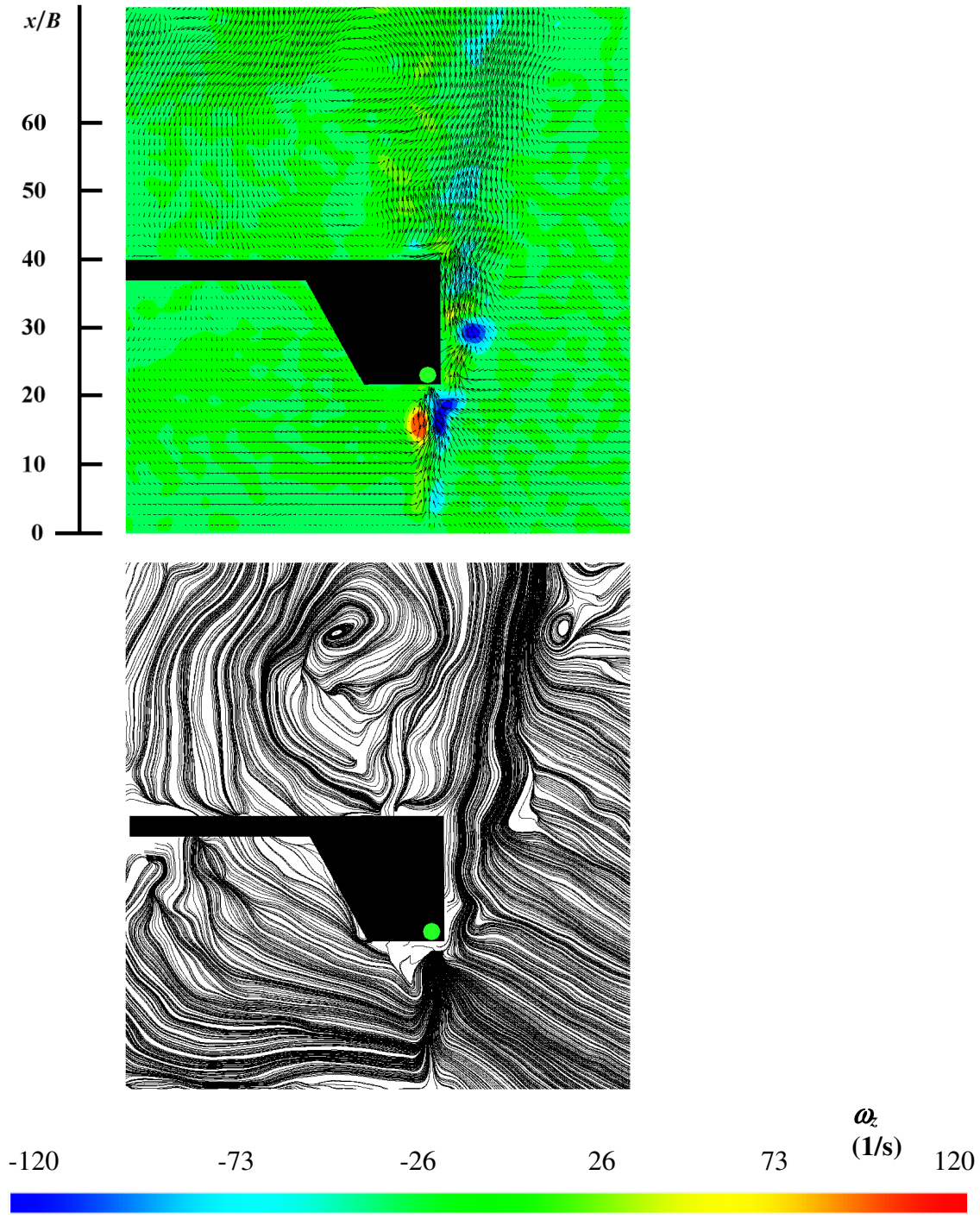

Fig. 5.40 Instantaneous velocity vector field colored by the vorticity and the corresponding streamlines of the CJ impinging onto a cylinder at Re_{CJ} = 161 ($Re_{CJ,D}$ = 542).

Fig. 5.39(a)). The jet remains smooth with no visible vortex structures. The separation occurs on the windward side of the cylinder and the leeward part of the cylinder is not influenced by the incoming jet. The Y-shaped pattern is somewhat asymmetrical with a stronger left part.

As the Reynolds number is increased to Re = 79 (Fig. 5.39(b), not shown in Fig. 5.37) the flow field does not change significantly. Again, the jet impinges on the cylinder surface and

the Y-shape pattern is subsequently formed. The angle between two branches is commensurate with the previous case, approximately 65°.

As the Reynolds number increases further (*Re* = 161), the flow-field changes considerably. The jet (see Fig. 5.37(b) and Fig. 5.39(c)) is not separated on the leeward side of the cylinder and the Y-shaped pattern is not seen in this case. The structure of the jet, behind the cylinder, resembles the wake behind the cylinder in the cross-flow. To show this behavior in more detail, the instantaneous velocity vector field and corresponding streamline map of the jet with *Re* = 161 are shown in Fig. 5.40. The individual vortices can be observed; however, unlike the cylinder in the cross-flow, no periodicity of the vortex structures were found in this case.

The width of the undisturbed jet (i.e., before it impinges onto the cylinder) is apparently reduced with increasing Reynolds number in all the jets from Fig. 5.39. This trend agrees with the observation by Sato and Sakao [22].

5.4 Convective heat transfer

The knowledge of the flow-field of both CJ and SJ (either solely standing or impinging the cylinder) allows to perform more complex experiments, i.e., the heat transfer investigation. The preliminary results have been published recently [133,134].

5.4.1 Natural convection

To validate the heating setup, the heat transfer experiments were initiated via a natural convection investigation, i.e., the cylinder was heated and no jet was operated. Just note here that the cylinder was placed in a tank large enough to avoid horizontal confinement and water level was high enough to avoid the vertical confinement (see Fig. 2.3 and description in Chapter 2). During the experiment, the heating power $P = UI$ was gradually enhanced from $P = 0.19$ W to 5.12 W. The results of the validation experiment are shown in Fig. 5.41 as *Nu*-*Gr* relationship. The selected experimental correlations [70,81,87] from Fig. 1.4 are also shown for comparison purposes. The correlation by Morgan [70] is shown with the declared 5% uncertainty range. It is obvious that present experimental data agree well with correlations, moreover, the present data are within a 5% uncertainty range of [70].

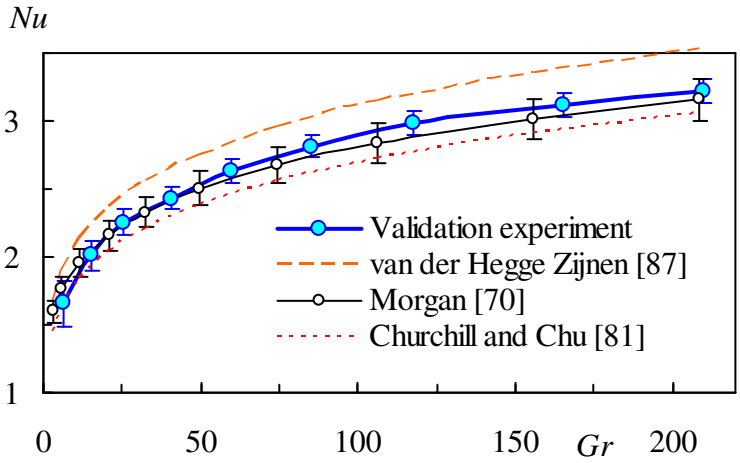

Fig. 5.41 Validation experiment - natural convection.

The corresponding Rayleigh number range of the experiment was Ra = 19-1035. The Rayleigh number range is far below the limit for a laminar-turbulent transition in the boundary layer and below the limit for the transition in the plume. Thus, the investigated plume is considered fully laminar.

5.4.2 Forced convection

After the successful validation experiment, the forced convection investigation was performed. First, the frequency characteristic of the SJ actuator was measured. The resulting *Nu*-*f* relationship is shown in Fig. 5.42. The nozzle-to-cylinder distance was H = 7.5 mm (H/B = 21).The measurement was performed simultaneously with the LDV measurement that was described previously in Chapter 5.2 (Fig. 5.15). This curve is also shown in Fig. 5.42 for comparison purposes. Obviously, the increasing velocity of the jet impinging on the cylinder

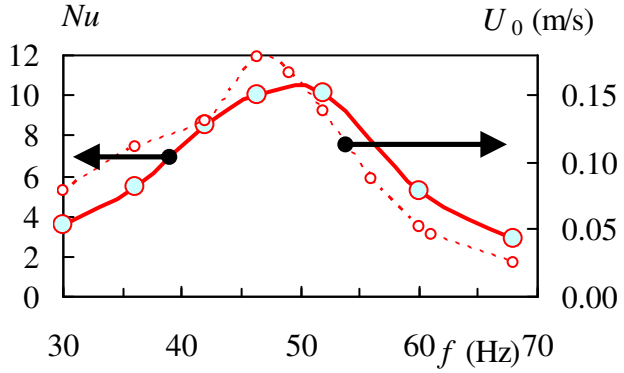

Fig. 5.42 Frequency characteristic of the SJ.

surface increases the Nusselt number. The local maximum (Nu = 10.0-10.4) was found at f = 46-52 Hz. This result reasonably agrees with the LDV experiment and with the theoretical prediction (see Chapter 5.2).

Small differences in peak locations between the curves in Fig. 5.42 may manifest the two relevant physical mechanisms of fluid mechanics and heat transfer, respectively. Namely, the U_0 maximum shows the resonant behavior of the actuator by means of the SJ formation at the nozzle. On the other hand, the Nu maximum shows the resultant heat transfer, which is influenced by many effects, e.g., the jet velocity decay in the nozzle-to-cylinder space and the flow field character at the cylinder surface, including a flow separation regime. Moreover, the relationship between the heat transfer rate and the SJ velocity is basically nonlinear in character, as will be confirmed by correlation Eq. (46) in the following text. Therefore, differences in physical mechanisms are the major reason for differences in peak locations in Figs. 5.42, while the minor reasons may be the experimental uncertainties of both measurements.

The following Fig. 5.43 demonstrates the heat transfer enhancement by means of the SJ at H/B = 10. It is obvious that the SJ causes the Nusselt number to enhance by 4.2–6.2 times against the natural convection. Moreover, Fig. 5.43 demonstrates the uncertainty of the experiments via the error bars indicating the expanded uncertainties of the 95 % confidence level (i.e., ±2 standard deviations σ_{Nu}). As discussed in section 3.5, the experiments with larger heating inputs and higher T_w–T_∞ differences have smaller uncertainties (the error bars

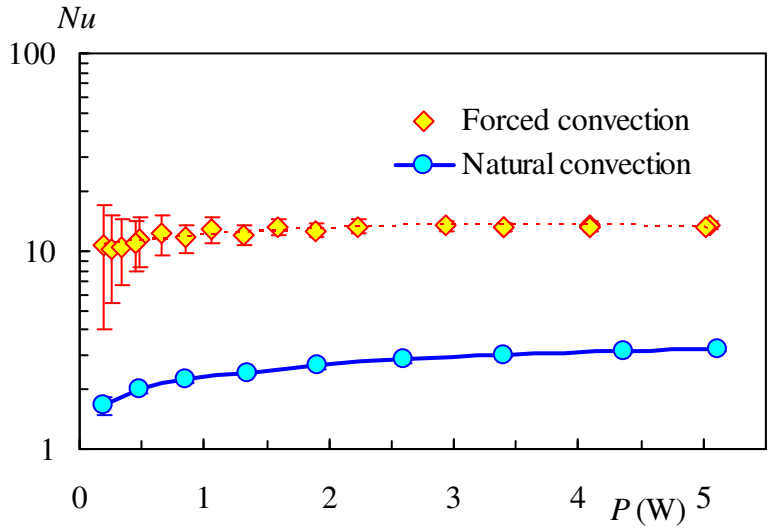

Fig. 5.43 Comparison of the natural and forced convection (SJ, H/B = 10); the error bars indicate the expanded uncertainties with a 95% confidence level (i.e. ±2 standard deviation σ_{Nu}).

cannot be visible in Fig. 5.43 because they are smaller than the data marks). On the other hand, the forced convection of smaller input heating and lower T_w–T_∞ have higher uncertainties. For example, SJ experiments for $P < 0.8$ W have T_w–T_∞ < 1 °C and uncertainties $2\sigma_{Nu} > 18$ %; such experiments are qualitative only and they are omitted from data processing. Nevertheless, the results of these experiments are also plotted in Fig. 5.43 to demonstrate these effects.

In the next step the effect of the nozzle-to-cylinder spacing H/B was investigated while the Reynolds number was kept approximately constant (Re = 220-270), see Fig. 5.44. The effect of the H/B spacing on Nu appears to be negligible, which agrees with the literature for lower Reynolds numbers (cf. Jeng et al. [106], for $Re_D < 1300$). The dashed line representing Eq. (46) is also plotted in Fig. 5.44, it will be described and explained in the text below.

Figure 5.45(a) shows the present forced convection data in the Nu-Re_D relationship. For comparison, two references are used that relate to the heat transfer from a circular cylinder to a uniform cross-flow (Morgan [70]) and to an IJ (Amiri et al. [105]). Note that the results by Amiri et al. [105] are the only authors from the list of available literature that fit the range of Reynolds number investigated in this work; moreover, the comparison of the present results with the data by Amiri et al. [105] is still very rough because no results exist in the available literature with closer parameters, namely with small cylinders (1 mm order of magnitude of diameters) in a jet flow. The Nusselt numbers for the present CJ and SJ were evaluated at temperature T_w, which was measured at the center plane $z = 0$. Additionally, the data series labeled as "CJ, near-end data" uses a Nu evaluation from T_w, which was measured at the end of the cylinder test section where the local maximum of the CJ velocity occurs; see Fig. 5.5 at

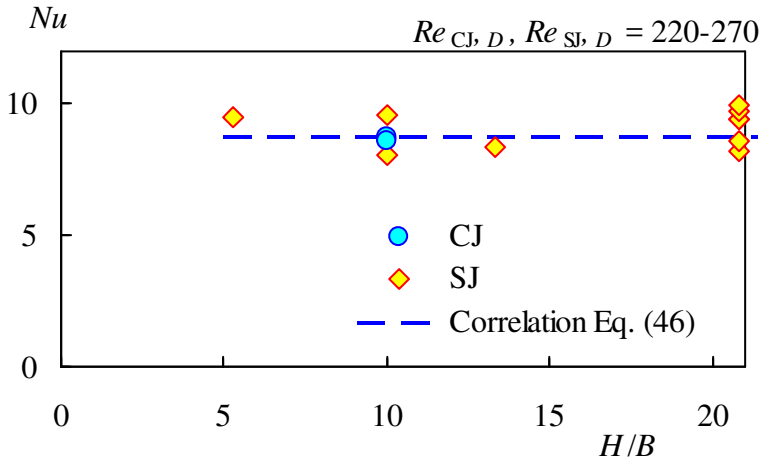

Fig. 5.44 Effect of the nozzle-to-cylinder spacing on Nu.

z = -15 mm. Obviously, the near-end *Nu* values were greater than *Nu* values for the center plane. The reason is the saddle-back velocity profile. Namely, the mean center plane exit velocity is smaller than the mean exit velocity U, whereas the near-end exit velocity is higher. To quantify this effect, the $C(z)$ factor is defined as the ratio of the exit velocity in the z location to the mean exit velocity U_m, i.e.,

$$C(z)= u(x=0, y= 0, z) / U_m. \quad (44)$$

This factor was evaluated for the saddle-back velocity profiles at x/B = 10–40 for z-locations at the center plane where z = 0 and the near-end plane where z = 15 mm. The resulting values are $C(z=0) = 0.76 \pm 0.06$ and $C(z=15 \text{ mm}) = 1.55 \pm 0.06$. Finally, the C factor was used to correct the Reynolds number for the center plane conditions via

$$Re_{DC} = C \cdot Re_{CJ,D}. \quad (45)$$

Considering the described corrections, the results from Fig. 5.45(a) are replotted in Fig. 5.45(b) as the Nu-Re_{DC} relationship. By using a least-squares fitting, the results were correlated via

$$Nu = 0.63\ Re_{DC}^{0.49}, \quad (46)$$

for Re_{DC} = 110–830. The maximum and standard deviation of the experimental data from Eq. (46) are 13% and 7%, respectively.

Figure 5.45(b) demonstrates similar slopes for all correlation lines, i.e., a qualitative agreement of the present data with the correlation performed by Morgan [70] (who proposed the exponent of 0.471). However, the present *Nu* values were much smaller than the results of [70,105], approximately 50% of their results. The present smaller *Nu* values are a manifestation of the flow patterns discussed above when only a relatively small windward side the cylinder circumference is effectively cooled by the jet and flow separation occurs there – see the flow visualizations in Figs. 5.37 and 5.38. The reasons for this result are a combination of the mini-scale effect from the narrow slot (B = 0.36 mm), the relatively small B/D ratio, and the relatively low Re_D with a prevailing laminar flow character. However, the

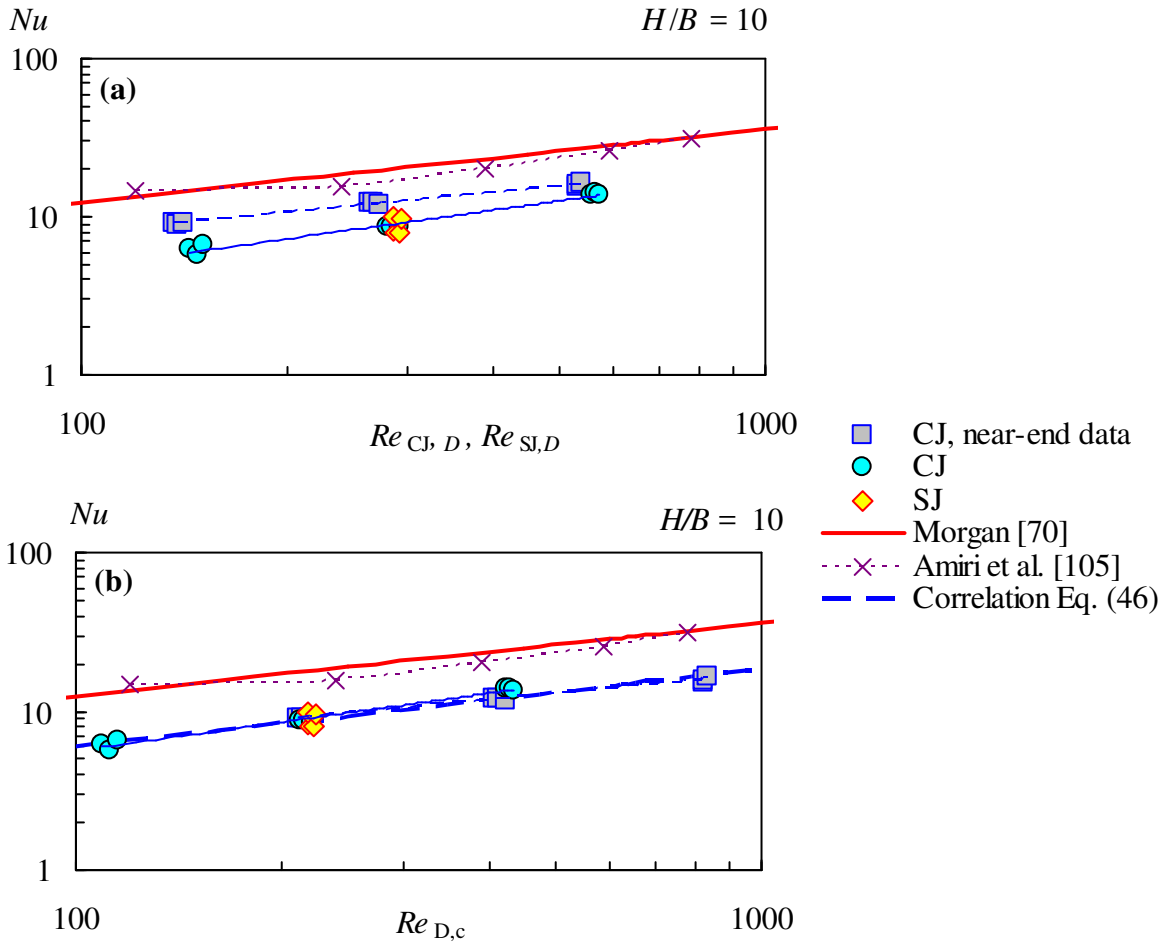

Fig. 5.45 Overall heat transfer (a) Nu-Re_D and (b) Nu-Re_{DC}.

choice of small values for B, B/D and Re_D follows the requirements for potential applications on mini/micro scales, even though this choice reduces the Nusselt number compared with a cylinder in an infinite uniform cross-flow and significantly saves the volume flux of the cooling fluid. A small volume flux is a principal capability of very compact, piezoelectric-driven actuators. Moreover, scaling down this alternative appears to be possible, compared with the classical, compressor-driven macro scale devices investigated in [70,105] because neither a pump (a blower), nor fluid supply piping is required.

6. Conclusions

6.1 Results and contribution of the thesis

This experimental work dealt with submerged water micro jets (the width of the jet is B = 0.36 mm) issuing from a rectangular nozzle with a relatively higher aspect ratio (AR = 111) at lower Reynolds numbers (Re = 40–160). The focus was given on a piezo-electrically driven synthetic jet. For comparison purposes, the continuous jet issuing from the same facility was also investigated. The task was studied from a fluid mechanics and heat transfer point-of-view.

In the Introduction part of the thesis, three aims were given. The fulfillment of the objectives is summarized in the following list:

(1) Fluid mechanics of a synthetic jet (SJ) issuing from a rectangular slot with small Reynolds numbers and small slot width – namely, the (micro) SJ with a slot width below 1 mm.

First, an extensive literature review was performed. Consequently, the free submerged synthetic jet was generated using a piezo-electrically driven actuator (Re_{SJ} = 67). The actuator was operated close to its resonant frequency (f = 46 Hz). The flow field was investigated using flow visualization (LIF technique) and velocity measurement (PIV technique). The time-mean output velocity was evaluated using surface measurements of a diaphragm deflection (LDV technique).

The present measurements revealed the highly 3D character of the initially rectangular jet. The strong variation of the velocity magnitude along the nozzle span was observed. The existence of streaky-like patterns in the velocity/vorticity field was confirmed. The present results are in good agreement with data from available literature.

(2) Fluid mechanics and heat transfer characteristics of the SJ impinging on a horizontal cylinder. A comparison of SJs and CJs is based on a hypothesis of their similarity.

The continuous jets were investigated at Re_{CJ} = 40, 79, 161 and the basic characteristics of the flow-fields were compared with data from available literature. The highly 3D nature of the initially 2D jet was revealed. The dependence of the velocity field on the spanwise location was identified. Saddle back velocity profiles were observed - as expected.

On the other hand, no gradual merging of the peaks or axis switching was revealed in this

case. The results agree with the literature for common macro jets. Moreover, some findings relate to the micro-size of the present jet, thus neither large coherent structures nor break-up effects were identified. The low mixing intensity and a slow axis velocity decrease were found.

- The synthetic jet was compared to continuous (steady) jets and several similarities were found in terms of the time-mean characteristics: highly 3D character of the jet issuing from a rectangular slot, highly non-uniform velocity distribution along the span and an absence of the axis switching phenomenon. Visualization of both continuous and synthetic jets impinging onto a circular cylinder confirms the expected flow-field similarity in this case, i.e., both jets are split into two halves after hitting the cylinder surface.
- The overall heat transfer characteristics were evaluated for both the continuous and synthetic jets impinging onto the cylinder. The average Nusselt numbers are commensurate in both cases. A quantification of the results was concluded by a proposal of a new correlation equation, as described in point 3.
- To determine synthetic jets, the Reynolds number was defined from the extrusion stroke of the cycle. The suitability of this approach for fluid mechanics and heat transfer components of the problem was confirmed.

(3) Quantification of the overall convective heat transfer rate in terms of the average Nusselt and Reynolds numbers.

To validate present overall convective heat transfer measurement, the natural convection from cylinders was measured. The results are in excellent agreement with representative references.

The enhancement of the average Nusselt number, using both continuous and synthetic jet, against natural convection was found to be 4.2–6.2 times. The influence of the nozzle-to-cylinder distance on the average Nusselt number was found to be negligible. The Nusselt number obtained for the present microjet was lower than the Nusselt number for conventional macro jet. A new correlation equation for the present range of parameters was proposed:

$Nu = 0.63\ Re_D^{0.49}$.

The results of the thesis contribute to

- deepening the basic knowledge of synthetic jet behavior from a fluid mechanics and heat transfer point-of-view,

- establishing more precise background for future investigations of potentially suitable cooling alternatives (e.g., highly loaded up-and-coming electronic components).

6.2 Future work

The future work could incorporate several of the following suggestions:

The present synthetic jet actuator can be optimized. The optimal working parameters to reach the maximal heat transfer rate and/or maximal efficiency can be found. An advanced variant of the actuator geometry with fluidic diodes (i.e., hybrid synthetic jet) could be applied.

Another important point that is admittedly far beyond the fluid mechanic and heat transfer point-of-view, is the design and utilization of more efficient piezoceramic transducers. Just note here that the present study used an available piezoceramic transducer, which is (in principle) not appropriate for underwater use.

Finally, the future work could and should apply more advanced measurement techniques and technologies. For example, the used experimental methods did not allow an investigation in the very nearfield of the jets. The present experiments focused on the time-mean and phase-averaged characteristics, which revealed many interesting features of the flow-fields and heat transfer mechanisms. However, advanced measurement technologies, with finer scaling in the spatial and time domains, could provide more valuable results. The use of micro-PIV and time-resolved PIV techniques can bring deeper sights into the physics of the micro-synthetic jets.

List of references

[1] K.C. Cheng, A History of Flow Visualization: Chronology, Journal of Flow Visualization and Image Processing. 1(4) (1997) 9-27.

[2] H. Schlichting, K. Gersten, Boundary-Layer Theory, Springer-Verlag, Berlin (2000).

[3] R.D. Blevins, Applied Fluid Dynamics Handbook, Krieger Publ. Comp., Malabar, Florida (2003).

[4] Nuventix/Aavid SynJet Cooling, web pages of the producer, available online http://www.aavid.eu/led-cooling/synjet-coolers, cited July 10th, 2017.

[5] Murata microblowers, web pages of the producer, available online http://www.murata.com/products/mechatronics/fluid/demo, cited July 10th, 2017.

[6] GE's Dual Piezoelectric Cooling Jets (DCJ), available online https://www.digitaltrends.com/cool-tech/ge-jet-engine-tech-silent-cooling/, cited July 10th, 2017.

[7] F. M. White, Viscous Fluid Flow, McGraw-Hill, New York (1991).

[8] W.G. Bickley, The Plane Jet, Philosophical Magazine 23 (7) (1937) 727-731 (cited according to [22]).

[9] E. Gutmark, I. Wygnanski, The Planar Turbulent Jet, Journal of Fluid Mechanics 73, part 3 (1976) 465-495.

[10] J. Mi, R.C. Deo, G.J. Nathan, Characterization of Turbulent Jets from High-Aspect-Ratio Rectangular Nozzles, Physics of Fluids 17 (2005) 1-4.

[11] P.M. Sforza, M.H. Steiger, N. Trentacoste, Studies on Three-Dimensional Viscous Jets, AIAA Journal 4(5) (1966) 800-806.

[12] N. Trentacoste, P. Sforza, Further Experimental Results for Three-Dimensional Free Jets, AIAA Journal 5 (5) (1967) 885-891.

[13] G.P. Lemieux, P.H. Oosthuizen, Experimental Study of the Behavior of Plane Turbulent Jets at Low Reynolds Numbers, AIAA Journal 23 (12) (1985) 1845-1846.

[14] I. Namer, M.V. Ötügen, Velocity Measurement in a Plane Turbulent Air Jet at Moderate Reynolds Numbers, Experiments in Fluids 6 (1988) 387-399.

[15] R.C. Deo, J. Mi, G.J. Nathan, The Influence of Reynolds Number on a Plane Jet, Physics of Fluids 20 (2008).

[16] R.C. Deo, J. Mi, G.J. Nathan, The Influence of Nozzle Aspect Ratio on Plane Jets, Experimental Thermal and Fluid Science 31 (2007) 825-838.

[17] R.C. Deo, G.J. Nathan, J. Mi, Comparison of Turbulent Jets Issuing from Rectangular Nozzles with and without Sidewalls, Experimental Thermal and Fluid Science 32 (2007) 596-606.

[18] K.B.M.Q. Zaman, Axis Switching and Spreading of an Asymmetric Jet: the Role of Coherent Structure Dynamics, Journal of Fluid Mechanics 316 (1996) 1-27.

[19] Y. Tsuchiya, C. Horikoshi, T. Sato, On the Spread of Rectangular Jets, Experiments in Fluids 4 (1986) 197-204.

[20] A.P. Vouros, T. Panidis, A. Pollard, R.R. Schwab, Near Field Vorticity Distributions from a Sharp-Edged Rectangular Jet, International Journal of Heat and Fluid Flow 51 (2015) 383-394.

[21] J.M. Cabaleiro, J.-L. Aider, Axis-Switching of a Micro-Jet, Physics of Fluids 26 (2014).

[22] H. Sato, F. Sakao, An Experimental Investigation of the Instability of a Two-Dimensional Jet at Low Reynolds Numbers, Journal of Fluid Mechanics 20, part 2 (1964) 337-352.

[23] A. Bejan, Convection Heat Transfer. 2nd Ed., John Wiley & Sons, Inc., New York (1995).

[24] C. Gau, C.H. Shen, Z.B. Wang, Peculiar Phenomenon of Micro-Free-Jet Flow, Physics of Fluids 21 (2009) 1-13.

[25] A. Muramatsu, H. Tsuchiya, An Effect of Initial Disturbance on Spatial Development of a Two-Dimensional Jet at a Low Reynolds Number, Proceedings of the 5th International Conference on Jets, Wakes and Separated Flows (ICJWSF2015) (2015) 51-59.

[26] V.V. Lemanov, V.I. Terekhov, K.A. Sharov, Investigation of the Flow in Free and Impinging Air Micro- and Macrojets, Proceedings of the 5th International Conference on Jets, Wakes and Separated Flows (ICJWSF2015) (2015) 1-8.

[27] T.M. Dauphinee, Acoustic air pump, Review of Scientific Instruments 28 (6) (1957) 456.

[28] R.D. James, J.W. Jacobs, A. Glezer, A Round Turbulent Jet Produced by an Oscillating Diaphragm, Physics of Fluids 8 (1996) 2484–2495.

[29] B.L. Smith, A. Glezer, The Formation and Evolution of Synthetic Jets, Physics of Fluids 10 (1998) 2281–2297.

[30] J.E. Cater, J. Soria, The Evolution of Round Zero-Net-Mass-Flux Jets, Journal of Fluid Mechanics 472 (2002) 167–200.

[31] S.G. Mallinson, J.A. Reizes, G. Hong, An Experimental and Numerical Study of Synthetic Jet Flow, Aeronautical Journal 105 (1043) (2001) 41–49.

[32] A. Glezer, M. Amitay, Synthetic Jets, Annual Review of Fluid Mechanics 34 (2002) 503-529.

[33] R. Holman, Y. Utturkar, R. Mittal, B.L. Smith, L. Cattafesta, Formation Criterion for Synthetic Jets, AIAA Journal 43 (10) (2005) 2110–2116.

[34] J. Zhou, H. Tang, S. Zhong, Vortex Roll-Up Criterion for Synthetic Jets, AIAA Journal 47 (2009) 1252–1262.

[35] Q. Xia, S. Zhong, An Experimental Study on the Behaviours of Circular Synthetic Jets at Low Reynolds Numbers, Proceedings of the Institution of Mechanical Engineers, Part C: Journal of Mechanical Engineering Science 226 (2012) 2686–2700.

[36] Z. Trávníček, Z. Broučková, J. Kordík, Formation Criterion for Axisymmetric Synthetic Jets at High Stokes Numbers, AIAA Journal 50 (2012) 2012–2017.

[37] Z. Trávníček, Z. Broučková, J. Kordík, T. Vít, Visualization of Synthetic Jet Formation in Air, Journal of Visualization 18 (2015) 595-609.

[38] A. McGuinn, R. Farrelly, T. Persoons, D.B. Murray, Flow Regime Characterisation of an Impinging Axisymmetric Synthetic Jet, Experimental Thermal and Fluid Science 47 (2013) 241–251.

[39] L.G. Pack, A. Seifert, Periodic Excitation for Jet Vectoring and Enhanced Spreading, Journal of Aircraft 38 (2001) 486–495.

[40] B.L. Smith, A. Glezer, Jet Vectoring Using Synthetic Jets, Journal of Fluid Mechanics 458 (2002) 1–34.

[41] D.A. Tamburello, M. Amitay, Three-Dimensional Interactions of a Free Jet with a Perpendicular Synthetic Jet, Journal of Turbulence 8 (2007) 1–18.

[42] M. Ben Chiekh, M. Ferchichi, J.–C. Bera, Modified Flapping Jet for Increased Jet Spreading Using Synthetic Jets, International Journal of Heat and Fluid Flow 32 (2011) 865–875.

[43] G. Hong, Effectiveness of Micro Synthetic Jet Actuator Enhanced by Flow Instability on Controlling Laminar Separation Caused by Adverse Pressure Gradient, Sensors and Actuators A-Physical 132 (2006) 607–615.

[44] G.M.G. Watson, L.W. Sigurdson, The Controlled Relaminarization of Low Velocity Ratio Elevated Jets-In-Crossflow, Physics of Fluids 20 (2008) 094108.

[45] F.–J. Chen, G.B. Beeler, Virtual Shaping of a Two-Dimensional NACA 0015 Airfoil Using Synthetic Jet Actuator, AIAA Paper 2002–3273 (2002).

[46] R. Mittal, P. Rampunggoon, On the Virtual Aeroshaping Effect of Synthetic Jets. Physics of Fluids 14 (2002) 1533–1536.

[47] J. Tensi, I. Boué, F. Paillé, G. Dury, Modification of the Wake behind a Circular Cylinder by Using Synthetic Jets, Journal of Visualization 5 (2002) 37–44.

[48] M. Ben Chiekh, J.C. Bera, M. Sunyach, Synthetic Jet Control for Flows in a Diffuser: Vectoring, Spreading and Mixing Enhancement, Journal of Turbulence 4 (2003) 1-12.

[49] Y. Yassour, J. Stricker, M. Wolfshtein, Heat Transfer from a Small Pulsating Jet, in: Proceedings of the 8th International Heat Transfer Conference, Vol. 3, Hemisphere Publ., San Francisco, USA (1986) 1183–1186

[50] Z. Trávníček, V. Tesař, Annular Synthetic Jet Used for Impinging Flow Mass–Transfer, International Journal of Heat and Mass Transfer 46 (2003) 3291–3297.

[51] D.S. Kercher, J.-B. Lee, O. Brand, M.G. Allen, A. Glezer, Microjet Cooling Devices for Thermal Management of Electronics, IEEE Transactions on Components Packaging and Manufacturing Technology 26 (2) (2003) 359–366.

[52] R. Mahalingam, N. Rumigny, A. Glezer, Thermal Management Using Synthetic Jet Ejectors, IEEE Transactions on Components Packaging and Manufacturing Technology 27 (3) (2004) 439–444.

[53] M.B. Gillespie, W.Z. Black, C. Rinehart, A. Glezer, Local Convective Heat Transfer from a Constant Heat Flux Flat Plate Cooled by Synthetic Air Jets, Transactions ASME Journal of Heat Transfer 128 (2006) 990–1000.

[54] M. Arik, An Investigation into Feasibility of Impingement Heat Transfer and Acoustic Abatement of Meso Scale Synthetic Jets, Applied Thermal Engineering 27 (2007) 1483–1494.

[55] P. Valiorgue, T. Persoons, A. McGuinn, D.B. Murray, Heat Transfer Mechanisms in an Impinging Synthetic Jet for a Small Jet-To-Surface Spacing, Experimental Thermal and Fluid Science 33 (2009) 597–603.

[56] M. Chaudhari, B. Puranik, A. Agrawal, Heat Transfer Characteristics of Synthetic Jet Impingement Cooling, International Journal of Heat and Mass Transfer 53 (2010) 1057–1069.

[57] T. Persoons, A. McGuinn, D.B. Murray, A General Correlation for the Stagnation Point Nusselt Number of an Axisymmetric Impinging Synthetic Jet, International Journal of Heat and Mass Transfer 54 (2011) 3900–3908.

[58] Z. Trávníček, L. Němcová, J. Kordík, V. Tesař, V. Kopecký, Axisymmetric Impinging Jet Excited by a Synthetic Jet System, International Journal of Heat and Mass Transfer 55 (2012) 1279–1290.

[59] Z. Trávníček, V.Tesař, Z. Broučková, K. Peszyński, Annular Impinging Jet Controlled by Radial Synthetic Jets, Heat Transfer Engineering 35 (4) (2014) 1450–1461.

[60] A. Lee, V. Timchenko, G.H. Yeoh, J.A.Reizes, Three-Dimensional Modelling of Fluid Flow and Heat Transfer in Micro-Channels with Synthetic Jet, International Journal of Heat and Mass Transfer 55 (2012) 198–213; Erratum in International Journal of Heat and Mass Transfer 55 (2012) 2746.

[61] Z. Trávníček, P. Dančová, J. Kordík, T. Vít, M. Pavelka, Heat and Mass Transfer Caused by a Laminar Channel Flow Equipped with a Synthetic Jet Array, Transactions ASME Journal of Thermal Science and Engineering Applications 2 (2012) 041006-1–041006-8.

[62] M. Amitay, F. Cannelle, Evolution of Finite Span Synthetic Jets, Physics of Fluids 18 (2006) 054101.

[63] J.C. Béra, M. Michard, N. Grosjean, G. Comte-Bellot, Flow Analysis of Two-Dimensional Pulsed Jets by Particle Image Velocimetry, Experiments in Fluids 31 (2001) 519-532.

[64] C. Yao, F.J. Chen, D. Neuhart, Synthetic Jet Flow Field Database for Computational Fluid Dynamics Validation, AIAA Journal 44 (12) (2006) 3153-3157

[65] S. Abdou, S. Ziada, Spanwise characteristics of High-Aspect-Ratio Synthetic Jets, AIAA Journal 44 (7) (2006) 1516-1523.

[66] F.P. Incropera, D.P. DeWitt, Introduction to Heat Transfer. 3rd Ed., John Wiley & Sons, New York (1996)

[67] J. Šesták, F. Rieger, Přenos hybnosti, tepla a hmoty. ČVUT, Praha (1993).

[68] F. Dumouchel, J.C. Lecordier, P. Paranthoën, The Effective Reynolds Number of a Heated Cylinder. International Journal of Heat and Mass Transfer 41 (1998) 1787–1794.

[69] H.J. Seuntiëns, R.N. Kieft, C.C.M. Rindt, A.A. van Steenhoven, 2D Temperature Measurement in the Wake of a Heated Cylinder Using LIF, Experiments in Fluids 31 (2001) 588-595

[70] V.T. Morgan, The Overall Convective Heat Transfer from Smooth Circular Cylinders, Advances in Heat Transfer 11 (1975) 199–264.

[71] R.M. Fand, K.K. Keswani, A Continuous Correlation Equation for Heat Transfer from Cylinders to Air in Crossflow for Reynolds Numbers from 10^{-2} to 2×10^{5}. International Journal of Heat and Mass Transfer 15 (3) (1972) 559–562.

[72] J. Pátek, J. Hrubý, J. Klomfar, M. Součková, A.H. Harvey, Reference Correlations for Thermophysical Properties of Liquid Water at 0.1 MPa. Journal of Physical and Chemical Reference Data 38 (1) (2009) 21–29.

[73] J. Šimonek, J. Vampola, J. Mošnerová, J. Štursa, Konvektivní přenos tepla v jednofázovém prostředí, Přenos tepla a hmoty II., Technické příručky 3, SVÚSS Praha (1978).

[74] W.H. McAdams, Heat Transmission, McGraw-Hill, New York (1954) (cited according to [70]).

[75] M.M. Zdravkovich, Flow around Circular Cylinders, Oxford university Press, Oxford (1997).

[76] M.A. Atmane, V.S.S. Chan, D.B. Murray, Natural Convection around a Horizontal Cylinder: The Effects of Vertical Confinement, International Journal of Heat and Mass Transfer 46 (2003) 3661-3672.

[77] F. Karim, B. Farouk, I. Namer, Natural Convection Heat Transfer from a Horizontal Cylinder between Vertical Confining Adiabatic Walls, Transactions ASME Journal of Heat Transfer 108 (1986) 291-298.

[78] F. Penot, O. Skurtys, D. Saury, Preliminary Experiments on the Control of Natural Convection in Differentially-Heated Cavities, International Journal of Thermal Sciences 49 (10) (2010) 1911–1919.

[79] Z. Broučková, Z. Trávníček, PIV and LIF Study of Flow and Thermal Fields of Twine Plumes in Water, EPJ Web of Conferences 143 (2017) 02012.

[80] Z. Broučková, Z. Trávníček, Natural Convection from a Pairof Horizontal Cylinders at Controlled Heating, in: Proceedings of the 9th World Conference on Experimental Heat Transfer, Fluid Mechanics and Thermodynamics (ExHFT-9), Iguaçu Falls, Brazil (2017) 113.

[81] S.W. Churchill, H.H.S. Chu, Correlating Equations for Laminar and Turbulent Free Convection from a Horizontal Cylinder, International Journal of Heat and Mass Transfer 18 (1975) 1049-1053.

[82] W. Elenbas, The Dissipation of Heat by Free Convection, Philips Research Reports 3 (1948) 338-360 (cited according to [70]).

[83] M.A. Mikheyev, Fundametals of Heat Transfer, 2nd Ed. Peace Publ., Moscow (1968) (cited according to [70]).

[84] Engineering Sciences Data Unit, Convective Heat Transfer during forced Crossflow of Fluids over a Circular Cylinder, including Free Conduction Effects. Item No. 69004, London (May 1969) with Amendment A (March 1970) (cited according to [70]).

[85] A.H. Davis, Natural Convective Cooling in Fluids, Philosophical Magazine 44 (1922) 920-940 (cited according to [70]).

[86] R.C.L. Bosworth, A New Method for the Comparison of the Thermal Conductivities of Fluids, Part 1, Journal and Proceedings of the Royal Society of New South Wales 81 (1947) 156-166 (cited according to [70]).

[87] B.G. van der Hegge Zijnen, Modified Correlation Formulae for the Heat Transfer by Forced Convection from Horizontal Cylinders, Applied Scientific Research, Section A 6 (1956) 129-140 (cited according to [70]).

[88] H.H. Bruun, Hot-Wire Anemometry, Principles and Signal Analysis. Oxford University Press, Oxford (1995).

[89] S.W. Churchill, M. Bernstein, A Correlating Equation for Forced Convection from Gases and Liquids to a Circular Cylinder in Crossflow. Transactions ASME Journal of Heat Transfer 99 (2) (1977) 300–306.

[90] A. Zhukauskas, J. Ziugzda, Heat Transfer of a Cylinder in Crossflow, Hemisphere Publ. Washington DC (1985).

[91] C.F. Lange, F. Durst, M. Breuer, Momentum and Heat Transfer from Cylinders in Laminar Crossflow at $10^{-4} \leq Re \leq 200$. International Journal of Heat and Mass Transfer 41 (22) (1998), 3409–3430.

[92] H. Kramers, Heat Transfer from Spheres to Flowing Media, Physica 12 (2-3) (1946) 61-80.

[93] R. Hilpert, Wärmeabgabe von geheizten Drähten und Rohren im Luftstrom, Forschung auf dem Gebiete des Ingenieurwesens 4 (1933) 215–224.

[94] A.-B. Wang, Z. Trávníček, On the Linear Heat Transfer Correlation of a Heated Circular Cylinder in Laminar Cross Flow by Using a New Representative Temperature Concept, International Journal of Heat and Mass Transfer 44 (24), 4635–4647.

[95] D.C. Collis, M.J. Williams, Two–Dimensional Convection from Heated Wires at Low Reynolds Numbers. Journal of Fluid Mechanics 6 (1959) 357–384.

[96] A.P. Hatton, D.D. James, H.W. Swire, Combined Forced and Natural Convection with Low–Speed Air Flow over Horizontal Cylinders. Journal of Fluid Mechanics, Part 1, 42 (1970) 17–31.

[97] Z. Trávníček, K. Peszyński, J. Hošek, S. Wawrzyniak, Aerodynamic and Mass Transfer Characteristics of an Annular Bistable Impinging Jet with a Fluidic Flip-Flop Control, International Journal of Heat and Mass Transfer 46 (7) (2003) 1265–1278.

[98] H. Martin, Heat and Mass Transfer between Impinging Gas Jets and Solid Surfaces, Advances in Heat Transfer 13 (1977) 1–60.

[99] H. Schuh, B. Persson, Heat Transfer on Circular Cylinders Exposed to Free-Jet Flow. International Journal of Heat and Mass Transfer 7 (1964) 1257-1271.

[100] C.S. McDaniel, B.W. Webb, Slot Jet Impingement Heat Transfer from Circular Cylinder, International Journal of Heat and Mass Transfer 43 (2000) 1975–1985.

[101] F. Gori, L. Bossi, Optimal Slot Height in the Jet Cooling of a Circular Cylinder, Applied Thermal Engineering 23 (2003) 859-870.

[102] C. Bartoli, P. Di Marco, S. Faggiani, Impingement Heat Transfer at a Circular Cylinder Due to a Submerged Slot Jet of Water, Experimental Thermal and Fluid Science 7 (1993) 279-286.

[103] S.A. Nada, Slot/Slots Air Jet Impinging Cooling of a Cylinder for Different Jets-Cylinder Configuration, Heat and Mass Transfer 43 (2006) 135-148.

[104] E.M. Sparrow, A. Alhomoud, Impingement Heat Transfer at a Circular Cylinder due to an Offset or Non-Offset Slot Jet, International Journal of Heat and Mass Transfer 27 (12) (1984) 2297-2306.

[105] S. Amiri, K. Habibi, E. Faghani, M. Ashjaee, Mixed Convection Cooling of a Heated Circular Cylinder by Laminar Upward-Directed Slot Jet Impingement. Heat and Mass Transfer 46 (2009) 225–236.

[106] T.-M. Jeng, S.-C. Tzeng, R. Xu, Heat Transfer Characteristics of a Rotating Cylinder with a Lateral Air Impinging Jet, International Journal of Heat and Mass Transfer 70 (2014) 235–249.

[107] Z. Trávníček, Z. Broučková, Způsob a zařízení pro chlazení těles válcového tvaru proudem chladicí tekutiny, CZ patent č. 306506 (2017).

[108] Z. Trávníček, T. Vít, Impingement Heat/Mass Transfer to Hybrid Synthetic jets and Other Reversible Pulsating Jets, International Journal of Heat and Mass Transfer 85 (2015) 473-487.

[109] B. Kutinová et al., Technický naučný slovník, SNTL, Prague (1981-1986).

[110] Fluorescence and Fluorescence Applications, Integrated DNA Technologies, available online, cited July 10th 2017

http://www.idtdna.com/pages/docs/technical-reports/fluorescence-and-fluorescence-applications.pdf

[111] C.V. Bindhu, S.S. Harilal, G.K. Varier, R.C. Issac, V.P.N. Nampoori, C.P.G. Vallabhan, Measurement of the Absolute Fluorescence Quantum Yield of Rhodamine B Solution Using a Dual-Beam Thermal Lens Technique, Journal of Physics D: Applied Physics 29 (1996) 1074–1079.

[112] J.A. Sutton, B.T. Fisher, J.W. Fleming, A Laser-Induced Fluorescence Measurement for Aqueous Fluids Flows with Improved Temperature Sensitivity, Experiments in Fluids 45 (2008) 869-881.

[113] Dynamic Studio, User's Guide, Dantec Dynamics.

[114] M.C.J. Coolen, R.N. Kieft, C.C.M. Rindt, A.A. van Steenhoven, Application of 2-D LIF Temperature Measurements in Water Using a Nd:YAG Laser, Experiments in Fluids 27 (1999) 420-426.

[115] M. Raffel, C.E. Willert, S.T. Wereley, J. Kompenhans, Particle Image Velocimetry – A Practical Guide, Springer-Verlag, Berlin (2007).

[116] C.E. Willert, M. Gharib, Digital Particle Image Velocimetry, Experiments in Fluids 10 (1991) 181-193.

[117] V. Kopecký, Laserová anemometrie, Technická univerzita v Liberci, Liberec (2005).

[118] Z. Broučková, S.-S. Hsu, A.-B. Wang, Z. Trávníček, Water Synthetic Jet Driven by a Piezoelectric Actuator - LIF and PIV Experiments, Advanced Materials Research 1104 (2015) 45-50.

[119] Z. Broučková, S.-S. Hsu, A.-B. Wang, Z. Trávníček, PIV and LIF Study of Slot Continuous Jet at Low Reynolds Number, EPJ Web of Conferences 114 (2016) 02007.

[120] B.H. Timmins, B.W. Wilson, B.L. Smith, P.P. Vlachos, A Method for Automatic Estimation of Instantaneous Local Uncertainty in Particle Image Velocimetry, Experiments in Fluids 53 (2012) 1133-1147.

[121] M. Gordon, J.E. Cater, J. Soria, Investigation of the Mean Passive Scalar Field in Zero-Net-Mass-Flux Jets in Cross-Flow Using Planar-Laser-Induced Fluorescence, Physics of Fluids 16 (3) (2004) 794-808.

[122] Uncertainty Analysis Particel Image Velocimetry, ITTC - Recommended Procedures and Guidlines, International Towing Tank Conference, Fukuoka, Japan (2008).

[123] A. Sciacchitano, B. Wieneke, F. Scarano, PIV Uncertainty, Quantification by Image Matching, Measurement Science and Technology 24 (2013) 045302.

[124] J.J. Charonko,P.P. Vlachos, Estimation of Uncertainty Bounds for Individual Particle Image Velocimetry, Measurement Science and Technology 24 (2013) 065301.

[125] Ometron, Portable Vibrometer VH - 1000 - D, User Manual.

[126] S.J. Kline, F.A. McClintock, Describing Uncertainties in Single-Sample Experiments, Mechanical Engineering 75 (1953) 3–8.

[127] Z. Broučková, P. Šafařík, Z. Trávníček, A Parameter Map of Synthetic Jet Regimes Based on the Reynolds and Stokes Numbers: Commentary on the Article by Rimasauskiene et al., Mechanical Systems and Signal Processing 68-69 (2016) 620-623.

[128] B.L. Smith, G.W. Swift, Synthetic Jets at Large Reynolds Number and Comparison to Continuous Jets, AIAA Paper, AIAA 2001-3030 (2001).

[129] Z. Broučková, Z. Trávníček, Visualization study of hybrid synthetic jets, Journal of Visualization 18 (4) (2015) 581–593.

[130] Z. Trávníček, A.I. Fedorchenko, A.-B.Wang, Enhancement of Synthetic Jets by Means of an Integrated Valve-Less Pump, Part I. Design of the Actuator, Sensors and Actuator A-Physical 120 (2005) 232-240.

[131] R. Nový, Hluk a chvění, Česká technika- nakladatelství ČVUT (2009).

[132] Z. Broučková, T. Vít, Z. Trávníček, Laser Doppler Vibrometry Experiment on a Piezo-Driven Slot Synthetic Jet in Water, EPJ Web of Conferences 92 (2015) 02007.

[133] Z. Broučková, Z. Trávníček, Visualization and Heat Transfer Study of a Synthetic Jet Impinging on a Circular Cylinder, in: *Proceedings of 12th International Conference on Heat Transfer, Fluid Mechanics and Thermodynamics (HEFAT2016)*, Malaga, Spain (2016) 1791–1796.

[134] Z. Broučková, Z. Trávníček, Visualization and Heat Transfer Study of a Synthetic Jet Impinging on a Circular Cylinder, Heat Transfer Engineering 40 (13–14) (2019) (in press; on line version will be available in 2018).

[135] C.H.K. Williamson, Defining a Universal and Continuous Strouhal–Reynolds Number Relationship for the Laminar Vortex Shedding of a Circular Cylinder, Physics of Fluids 31 (10) (1988) 2742–2744.

Publications of author

The following list includes all the publications of the author. Some of the publications were cited in the Reference section, for the sake of clarity the numbers from the Reference section are indicated here as well.

Publications with the direct connection to the results of the thesis

Publications indexed in Web of Science and Scopus

Journal with impact factor

[ZB1] [134] Z. Broučková, Z. Trávníček, T. Vít, Synthetic and continuous jets impinging on a circular cylinder. *Heat Transfer Eng*. 40 (13–14) 2019 (in press; on line version will be available in 2018).

Journals without impact factor

[ZB2] [119] Z. Broučková, S.-S. Hsu, A.-B. Wang, Z. Trávníček, PIV and LIF study of slot continuous jet at low Reynolds number. EPJ Web of Conferences 114, 02007 (2016). (Experimental Fluid Mechanics 2015, Prague, Czech Republic).

[ZB3] [132] Z. Broučková, T. Vít, Z. Trávníček, Laser Doppler vibrometry experiment on a piezo-driven slot synthetic jet in water. EPJ Web of Conferences 92 02007 (2015). (Experimental Fluid Mechanics 2014, Český Krumlov, Czech Republic).

Publications not indexed in WoS and Scopus

Journal without impact factor

[ZB4] [118] Z. Broučková, S.-S. Hsu, A.-B. Wang, Z. Trávníček, Water synthetic jet driven by a piezoelectric actuator - LIF and PIV experiments. Advanced Materials Research 1104 (2015) 45-50. (Spring International Conference on Material Sciences and Technology 2015, Beijing, China).

Conference contribution

[ZB5] [133] Z. Broučková, Z. Trávníček, Visualization and heat transfer study of a synthetic jet impinging on a circular cylinder. In: Proceedings of 12th International Conference on Heat Transfer, Fluid Mechanics and Thermodynamics /HEFAT2016/, Costa del Sol, Spain, 11-13 July 2016, pp. 1791-1796.

Publications without the direct connection to the results of the thesis

Publications indexed in Web of Science and Scopus

Journal with impact factor

[ZB6] [127] Z. Broučková, P. Šafařík, Z. Trávníček, A parameter map of synthetic jet regimes based on the Reynolds and Stokes numbers: commentary on the article by Rimasauskiene et al. *Mech. Syst. Signal Proc.* 68-69 (2016) pp. 620-623

[ZB7] [37] Z. Trávníček, Z. Broučková, J. Kordík, T. Vít, Visualization of synthetic jet formation in air. *J. Vis.* 18 (2015) pp. 595-609

[ZB8] [129] Z. Broučková, Z. Trávníček, Visualization study of hybrid synthetic jets. *J. Vis.* 18 (2015) pp. 581-593

[ZB9] J. Kordík, Z. Broučková, Z. Trávníček, Impinging jet-based fluidic diodes for hybrid synthetic jet actuators. *J. Vis.* 18 (3) (2015) pp. 449-458

[ZB10] J. Kordík, Z. Broučková, T. Vít, M. Pavelka, Z. Trávníček, Novel methods for evaluation of the Reynolds number of synthetic jets. *Exp Fluids.* 55 (6) (2014) pp. 1757-1-1757-16.

[ZB11] [59] Z. Trávníček, V. Tesař, Z. Broučková, K. Peszyński, Annular impinging jet controlled by radial synthetic jets. *Heat Transfer Eng*. 35 (16-17) (2014), pp. 1450-1461.

[ZB12] [36] Z. Trávníček, Z. Broučková, J. Kordík, Formation criterion for synthetic jets at high Stokes numbers. *AIAA J*. 50 (9) (2012) pp. 2012-2017.

Journals without impact factor

[ZB13] [79] Z. Broučková, Z. Trávníček, PIV and LIF study of flow and thermal fields of twine plumes in water. EPJ Web of Conferences 143 02012 (2017). (Experimental Fluid Mechanics 2016, Mariánské Lázně, Czech Republic).

[ZB14] Z. Broučková, E. Flídr, P. Šafařík, Z. Trávníček, Active control of the wake behind the cylinder. EPJ Web of Conferences 143 02011 (2017). (Experimental Fluid Mechanics 2016, Mariánské Lázně, Czech Republic).

[ZB15] Z. Broučková, P. Pušková, Z. Trávníček, P. Šafařík, Jet flow issuing from an axisymmetric pipe-cavity-orifice nozzle. EPJ Web of Conferences 114, 02006 (2016). (Experimental Fluid Mechanics 2015, Prague, Czech Republic).

[ZB16] Z. Broučková, Z. Trávníček, P. Šafařík, Bubble dynamics in drinks. EPJ Web of Conferences 67 02011 (2014). (Experimental Fluid Mechanics 2013, Kutná Hora, Czech Republic).

[ZB17] Z. Broučková, Z. Trávníček, P. Šafařík, Active control of the jet in coaxial arrangement. EPJ Web of Conferences 45 01016 (2013). (Experimental Fluid Mechanics 2012, Hradec Králové, Czech Republic).

[ZB18] V. Tesař, Z. Broučková, J. Kordík, Z. Trávníček, K. Peszyński, Valves with flow control by synthetic jets. EPJ Web of Conferences 25 01092 (2012). (Experimental Fluid Mechanics 2011, Jičín, Czech Republic).

[ZB19] Z. Broučková, Z. Trávníček, P. Šafařík, Visualization of synthetic jets at higher Stokes numbers. EPJ Web of Conferences 25 01007 (2012). (Experimental Fluid Mechanics 2011, Jičín, Czech Republic).

Publications not indexed in WoS and Scopus

(some of them in Czech language)

Patents

[ZB20] [107] Z. Trávníček, Z. Broučková, Method and device for cooling of cylinder-shaped bodies by a cooling fluid jet). Patent No. 306506, Jan. 4, 2017 (in Czech).

[ZB21] Z. Trávníček, Z. Broučková, Method and device for generation of a synthetic jet or a hybrid synthetic jet. Patent Application PV 2017-420, June 20, 2017 (in Czech).

Conference contributions

[ZB22] [80] Z. Broučková, Z. Trávníček, Natural convection from a pair of horizontal cylinders at controlled heating. In: Proceedings of 9th World Conference on Experimental Heat Transfer, Fluid Mechanics and Thermodynamics /ExHFT-9/, Iguazu Falls, Brazil, 11-15 June 2017.

[ZB23] Z. Trávníček, F. Maršík, T. Vít, Z. Broučková, M. Pavelka, Lift forces on a circular cylinder in cross flow resulting from heat/mass transfer. In: Proceedings of 16th International Conference on Computational Methods and Experimental Measurements CMEM 2013, 2 - 4 July, 2013, Coruna, Spain, 149-159.

[ZB24] E. Flídr, P. Šafařík, Z. Trávníček, Z. Broučková, Aktivní řízení proudového pole syntetizovaným proudem v případě příčně obtékaného kruhového válce. Fluid mechanics and thermodynamics - Proceedings of Students' Work in the Year 2015/2016, Eds.: J. Ježek, J. Nožička, J. Adamec, P. Šafařík, ČVUT, Praha, 2016, 41-55.

[ZB25] P. Pušková, P. Šafařík, Z. Trávníček, Z. Broučková, Pasivní řízení symetrického proudu vzduchu. Fluid mechanics and thermodynamics - Proceedings of Students' Work in the Year 2014/2015, Eds.: J. Ježek, J. Nožička, J. Adamec, P. Šafařík, ČVUT, Praha, 2015, 67-79.

[ZB26] E. Flídr, P. Šafařík, Z. Trávníček, Z. Broučková, Malý aerodynamický tunel. Fluid mechanics and thermodynamics - Proceedings of Students' Work in the Year 2014/2015, Eds.: J. Ježek, J. Nožička, J. Adamec, P. Šafařík, ČVUT, Praha, 2015, 33-48.

[ZB27] E. Flídr, P. Šafařík, Z. Trávníček, Z. Broučková, Měření rychlosti a frekvence vzduchu v syntetizovaném proudu. Fluid mechanics and thermodynamics - Proceedings of Students' Work in the Year 2013/2014, Eds.: J. Ježek, J. Nožička, J. Adamec, P. Šafařík, ČVUT, Praha, 2014, 5-17.

[ZB28] I. Ng, V. Timchenko, J. Reizes, Z. Trávníček, J. Kordík, Z. Broučková, Synthetic jets at low Stokes number: numerical and experimental approach. In: 10th International Conference on Flow Dynamics, Sendai International Center, Miyagi, Japan, Nov. 25 -27, 2013, OS7-8, 472-473.

[ZB29] Z. Trávníček, Z. Broučková, J. Kordík, Visualization of synthetic jet formation in air. In: 12th International Symposium on Fluid Control, Measurement and Visualization (FLUCOME), Nara, Japan, Nov. 18-23, 2013, OS6-02-2.

[ZB30] Z. Broučková, Z. Trávníček, P. Šafařík, Spektrální analýza kontinuálního a syntetizovaného proudu. Fluid mechanics and thermodynamics - Proceedings of Students' Work in the Year 2012/2013, Eds.: J. Ježek, J. Nožička, J. Adamec, P. Šafařík, ČVUT, Praha, 2013, 19-32.

[ZB31] Z. Broučková, Z. Trávníček, P. Šafařík, Vizualizace obtékání rotujícího válce. Fluid mechanics and thermodynamics - Proceedings of Students' Work in the Year 2011/2012, Eds.: J. Ježek, J. Nožička, J. Adamec, P. Šafařík, ČVUT, Praha, 2012, 19-35.

[ZB32] Z. Trávníček, V. Tesař, Z. Broučková, K. Peszyński, Annular impinging jet controlled by radial synthetic jets. In: 9th International Conference on Heat Transfer, Fluid Mechanics and Thermodynamics, HEFAT 2012, Malta, July 16-18, 2012, 487–493.

[ZB33] Z. Broučková, Z. Trávníček, P. Šafařík, Visualization of the annular synthetic jet. In: Aktuální problémy mechaniky tekutin 2012, Ústav termomechaniky AV ČR, v. v. i.,15.2.–17.2. 2012, str. 13-16.

[ZB34] Z. Broučková, P. Šafařík, Z. Trávníček, Oblast parametrů syntetizovaných proudů. Fluid mechanics and thermodynamics - Proceedings of Student' Work in the Year 2010/2011, Eds.: J. Ježek, J. Nožička, J. Adamec, P. Šafařík, ČVUT, Praha, 2011, 23-38.

[ZB35] Z. Broučková, Z. Trávníček, P. Šafařík, The interaction of continual and synthetic jets. In: Aktuální problémy mechaniky tekutin 2011, Ústav termomechaniky AV ČR, v. v. i.,16.2.–17.2. 2011, str. 21-24.

[ZB36] Z. Broučková, P. Šafařík, Z. Trávníček. Aktivní řízení anulárního proudu radiálním syntetizovaným proudem. Fluid mechanics and thermodynamics - Proceedings of Students' Work in the Year 2009/2010, Eds.: J. Ježek, J. Nožička, J. Adamec, P. Šafařík, ČVUT, Praha, 2010, 5-14.

[ZB37] Z. Broučková, J. Kordík, Z. Trávníček, V. Tesař, P. Šafařík, K. Peszyński, Aktivní řízení anulárního proudu radiálním syntetizovaným proudem. In: Aktuální problémy mechaniky tekutin 2010, Ústav termomechaniky AV ČR, v. v. i.,10.2.–11.2. 2010, str. 23-26.

[ZB38] V. Tesař, Z. Trávníček, J. Kordík, Z. Broučková, Fluidic circuit theory applied to problem of resonant frequency in synthetic-jet actuators. In: 13th International Conference on Developments in Machinery Design and Control, Vol. 11 (2009) pp. 97–98.

Research reports

[ZB39] P. Bauer, Z. Broučková, J. Kordík, M. Sedlář, Návrh metodiky výpočtu ventilačních ztrát převodovky. Výzkumná zpráva Z-1525/15, Ústav termomechaniky AV ČR, 2015.

[ZB40] E. Flídr, Z. Broučková, M. Pavelka, Z. Trávníček, Malý aerodynamický tunel pro vizualizaci proudového pole. Výzkumná zpráva Z-1520/15, Ústav termomechaniky AV ČR, 2015.

[ZB41] Z. Broučková, J. Kordík, Z. Trávníček, Aktivní řízení anulárního proudu radiálním syntetizovaným proudem. Výzkumná zpráva Z 1438/09, Ústav termomechaniky AV ČR, 2009.

Appendix I *Velocity and vorticity maps of the CJ*

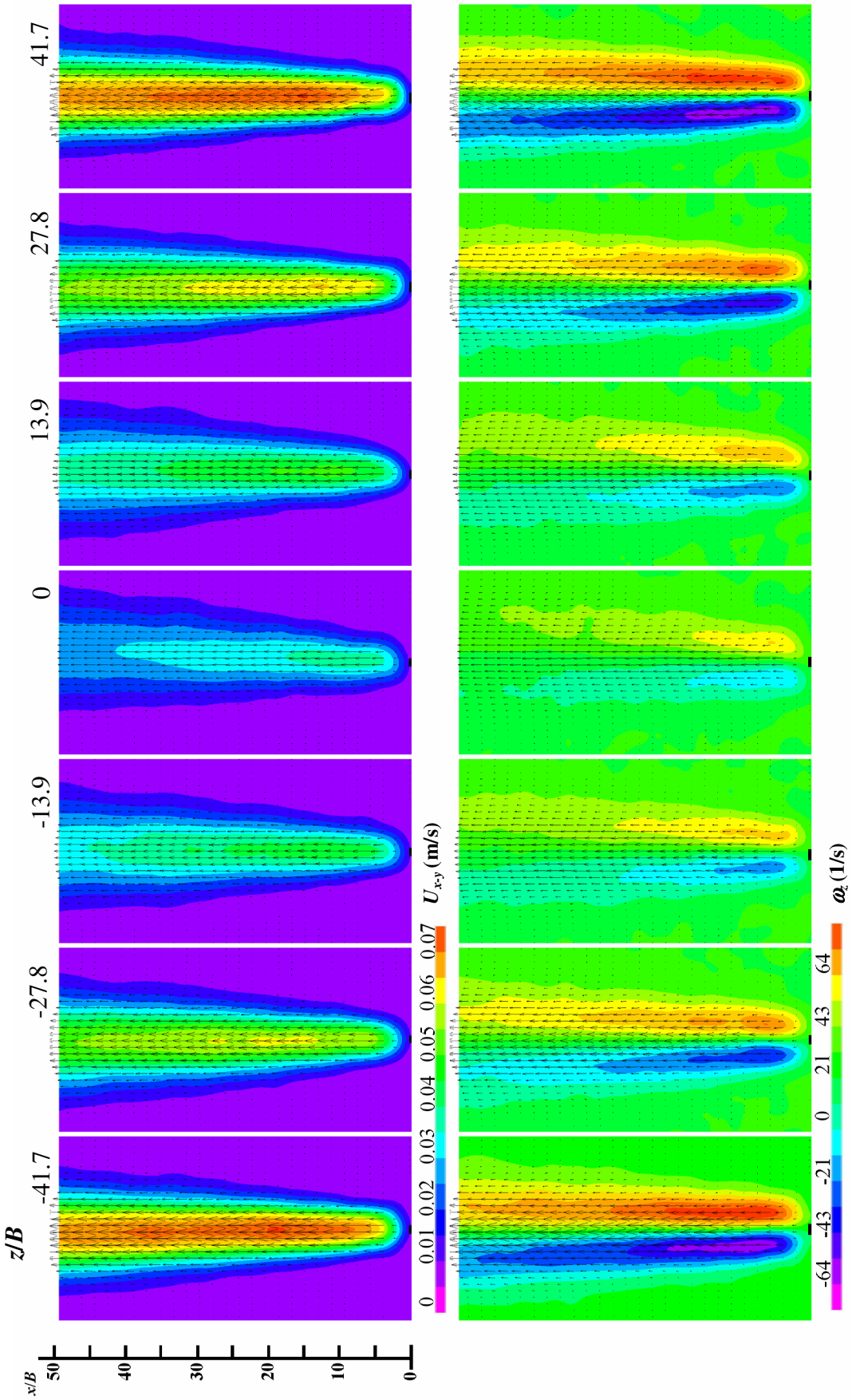

Appendix II *Velocity and vorticity maps of the SJ*

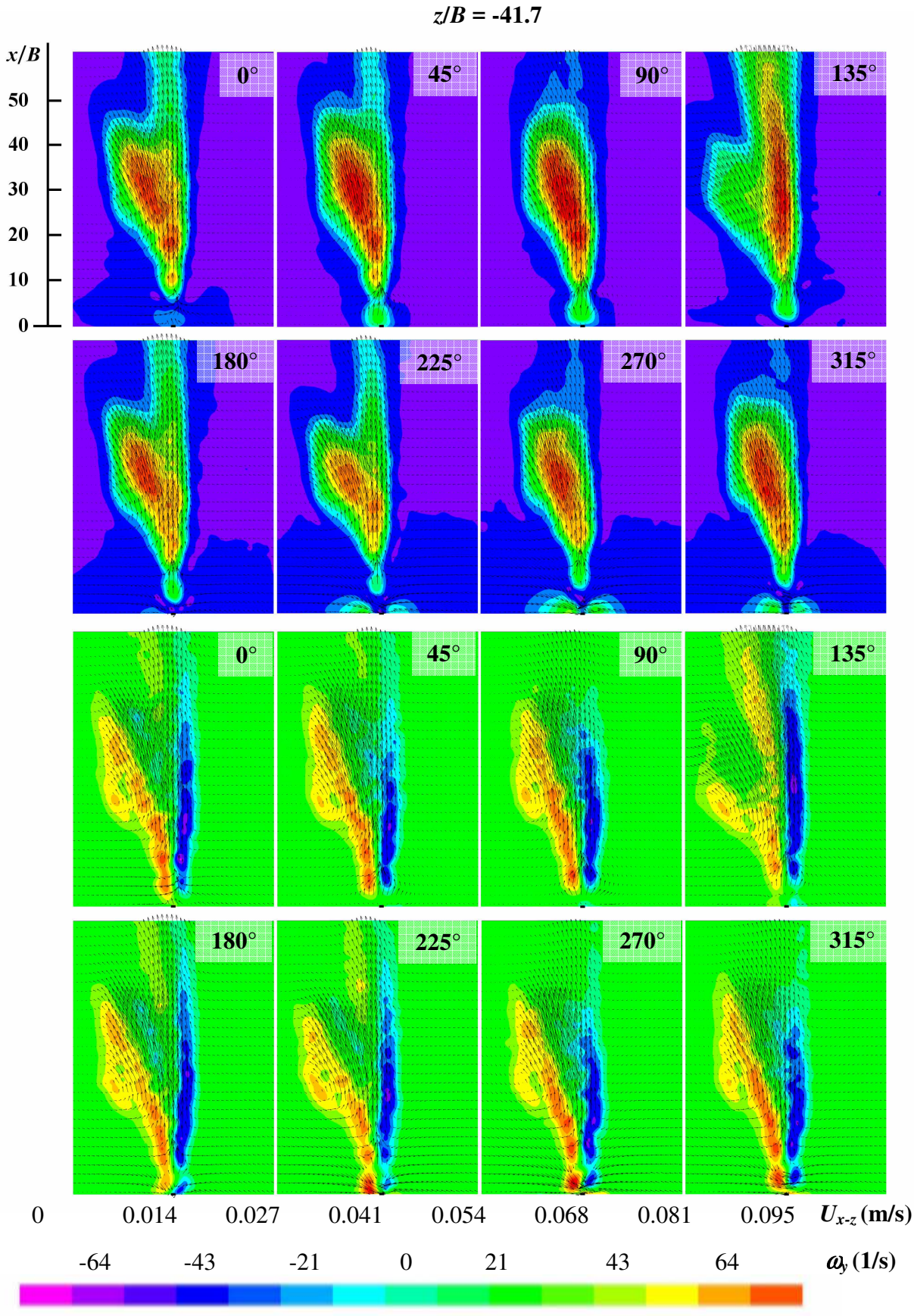

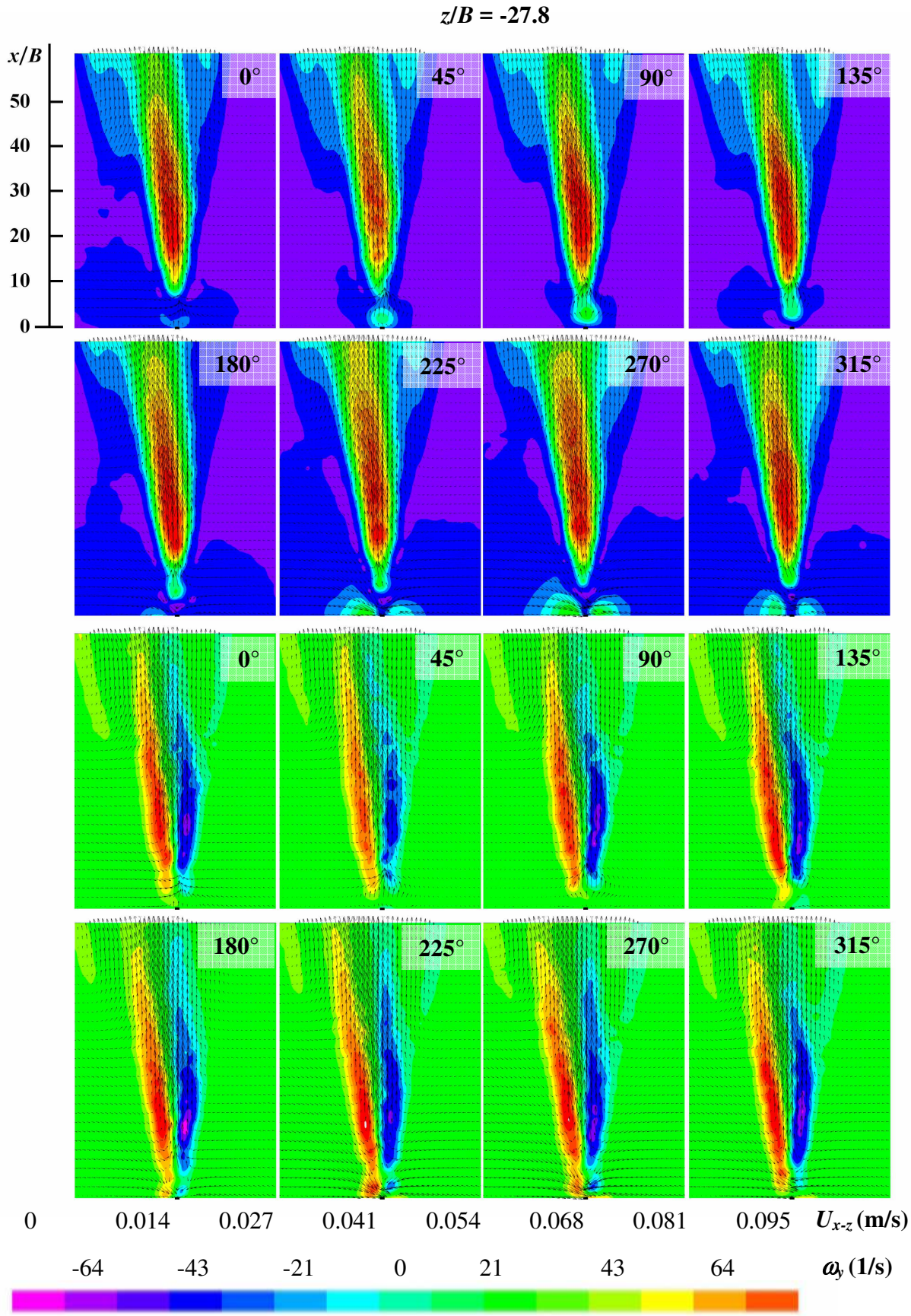
z/B = -27.8
x/B
50
40
30
20
10
0
0°
45°
90°
135°
180°
225°
270°
315°
0°
45°
90°
135°
180°
225°
270°
315°
0
0.014
0.027
0.041
0.054
0.068
0.081
0.095
U x-z (m/s)
-64
-43
-21
0
21
43
64
ω y (1/s)

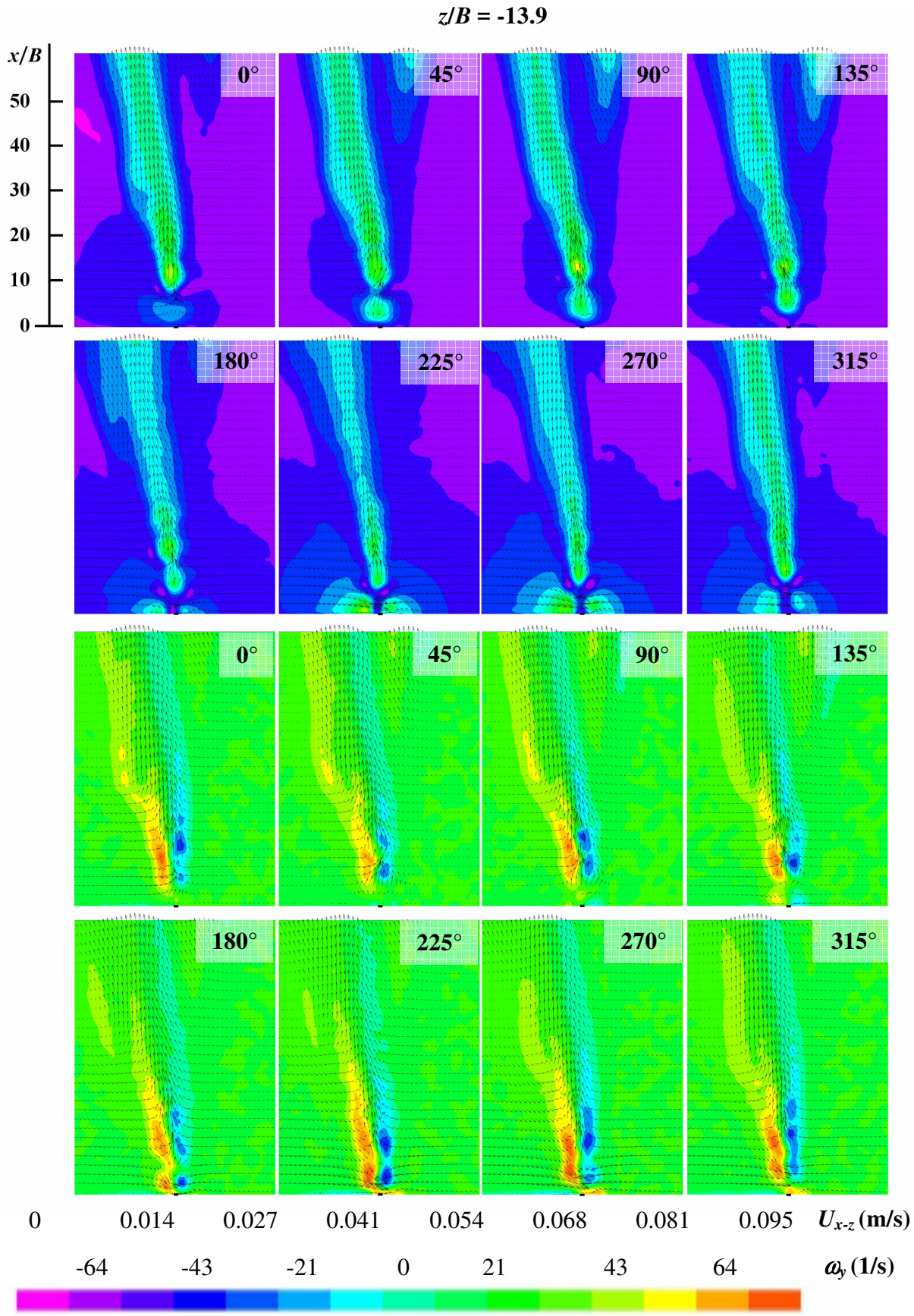
z/B = -13.9
x/B
50
40
30
20
10
0
0°
45°
90°
135°
180°
225°
270°
315°
0°
45°
90°
135°
180°
225°
270°
315°
0
0.014
0.027
0.041
0.054
0.068
0.081
0.095
U x-z (m/s)
-64
-43
-21
0
21
43
64
ω y (1/s)

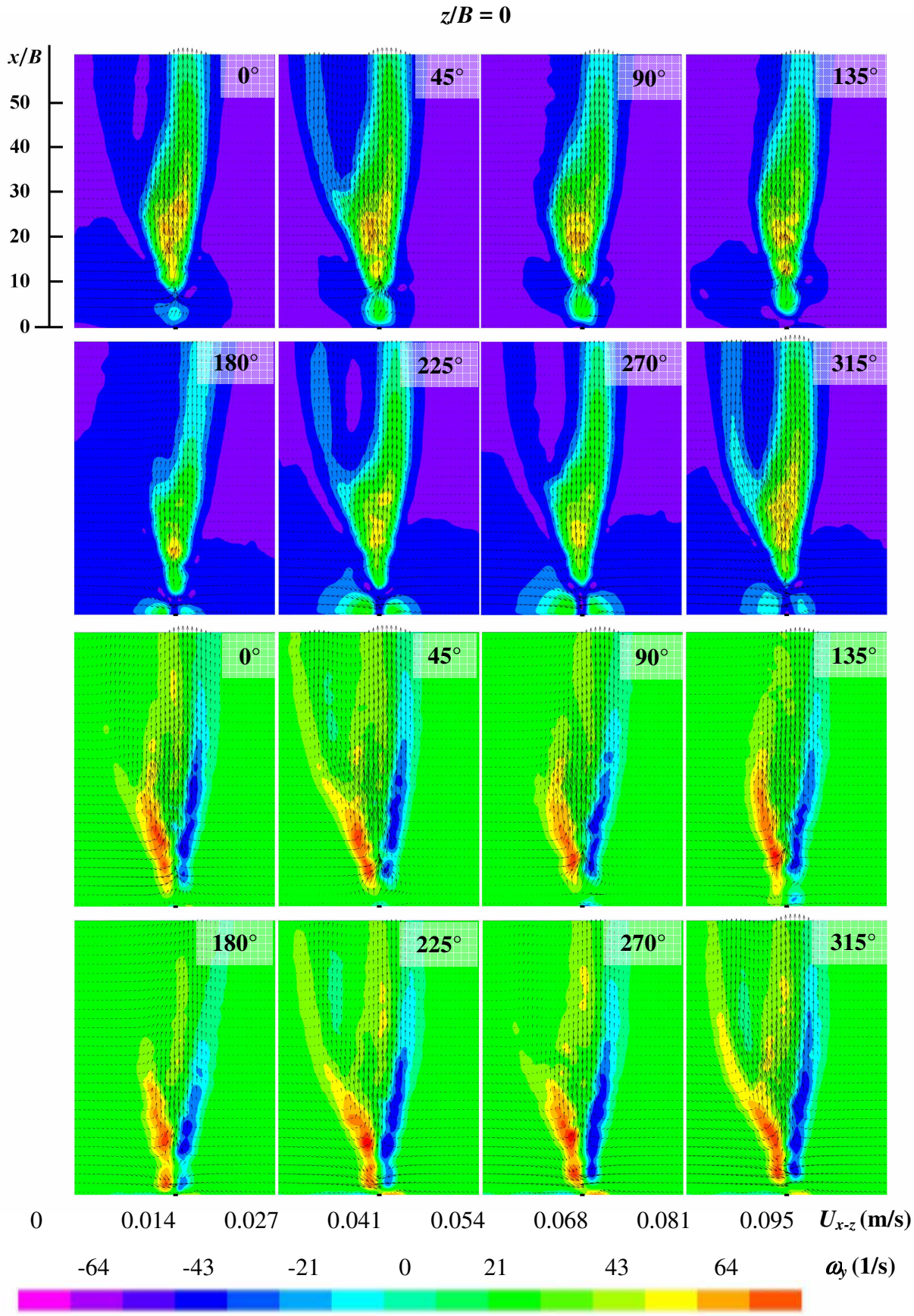
z/B = 0
x/B
50
40
30
20
10
0
0°
45°
90°
135°
180°
225°
270°
315°
0°
45°
90°
135°
180°
225°
270°
315°
0
0.014
0.027
0.041
0.054
0.068
0.081
0.095
U x-z (m/s)
-64
-43
-21
0
21
43
64
ω y (1/s)